Elevated Temperature Measurements during a Hypervelocity Impact Process

A Thesis Submitted for the Degree of Doctor of Philosophy

by

Konstantinos Tsembelis

June 1998

The Unit for Space Sciences and Astrophysics

School of Physical Sciences

University of Kent at Canterbury

Στήν οικογένειά μου,

Γεώργειο, Αγγελική-Ιωάννα και 'Ελενα Τσεμπελή.

Σας ευχαριστώ πολύ.

To my family,

Georgios, Aggeliki-Ioanna and Heleni Tsembelis.

Thank you very much.

We live on a small island of knowledge in a huge sea of ignorance. What we do in science is to reclaim some land for that island. But of course the new island is still surrounded by ignorance.

Sir Hermann Bondi

ABSTRACT

Experiments have been performed using the 2 MV Van de Graaff dust accelerator facility of the University of Kent at Canterbury. Iron dust particles were accelerated towards a glass target. Velocities in the range 5-20 km s^{-1} were attained for particles of mass 10^{-17} - 10^{-14} kg. Intensity of the resulting light flash was then measured for two different wavelengths and the temperature of the ejecta cloud was found assuming black body emission.

Experimental results were compared against one dimensional predictions based on equilibrium thermodynamics. A Mie-Gruneisen equation of state was assumed for the glass target. Shock state and subsequent release gave an estimation for the temperature.

Finally, a simple model was constructed to simulate glass hypervelocity impacts with the use of hydrocodes. Although numerical and computational deficiencies limited the use of hydrocodes to predict ejecta cloud temperatures, it was possible to use the model to estimate the dimensions of the impact craters on glass and compare them with published data.

Acknowledgements

A big 'thanks' to my family who supported me both financially and morally. I dedicate this thesis to them. I hope I made you proud.

I am deeply grateful to my supervisor Mark J Burchell. His patience and persistence made this research program to finish within three years. Although the disagreements we had, I would not have done it without him. Thank you Mark.

I am also grateful to my friend and colleague Nikolaos Margaritis for his valuable support and help he provided me in FORTRAN and general thermodynamics. Needless to mention the time we spent together talking about serious subjects such as philosophy of science or cosmology and silly ones such as basketball or the endless hours in front of the TV watching science fiction films and talking about their science. Beam me up Scottie!

I would also like to thank my colleague Emma A Taylor for asking me all these annoying questions about shock physics and made me to understand the subject better. Good luck with your new SPH. You are going to need it.

J A M McDonnell, the head of the group, provided me with valuable comments and financial support.

Paul R Ratcliff and David Gardner for teaching me how to use AUTODYN™ and giving me answer to questions about hydrocodes.

Century Dynamics Limited have been very helpful and always willing to spend time giving clues to set up AUTODYN in a more efficient way.

Mike Cole, as the experimental officer of our group, helped setting up my experiments in the Van de Graaff.

Cathy Cowdery and Major MacKenzie of DERA tested my Glass Analogue Model in its first stage.

Thanks also go to Hypervelocity Impact Society for providing funds to attend the HVIS '96 and thus meet Charles Anderson and Tim Holmquist who both helped my research with their valuable comments.

My new colleagues at the Cambridge Cavendish Lab., Neil Bourne, Jeremy Millett, Natalie Murray, Bill Proud and Lousy Forde provided me with last minutes corrections.

My roommates, Bryan Vaughan, David Catling and Tom Murphy were very patient with my, sometimes, irritating Greek character.

The owners of the Ben Johnson restaurant, Manolis and Amanda Theodorakis who hired me as an assistant manager in their kitchen and thus helped me financially.

I would like to thank my following friends for the moral support they provided during the seven years of my student life: N. Kalafatis, L. Economou, E. Louridas, P. Toumpaniaris, M. Stergiou, T. Amoratis, P. Georgopoulou, A. Georgantas, H. Kakoulidis, G. Fotiou, V. Gevros, N. Roukounakis, G. Mahas, and E. Georgiadou. If I have forgotten anybody, sorry about that!

List of Tables

List of Figures

CONTENTS

CHAPTER 1

Introduction

The near Earth space environment is a potentially dangerous place for spacecraft. The reason is that both man-made space debris and micrometeoroids orbit the Earth, such objects may impact on the velocity range of 5 to 30 km s^{-1}. Spacecraft surfaces may be penetrated and, in the limit, spacecraft can be destroyed. In recent years, extensive research has been being conducted to characterise the effects on spacecraft structural materials subjected to hypervelocity impacts. Whole conferences and symposia are now devoted in answering questions and giving new insights to material phenomena under hypervelocity impacts.

Hypervelocity impacts do not happen only on spacecraft. They are typical at solar system bodies such as planets and satellites. The surface of the Moon, for instance, is covered with large craters due to impacts of objects such as comets and asteroids. The extinction of the dinosaurs, here on Earth, was probably due to the impact of a large comet on the Yucatan peninsula. Although plate tectonic movements and subsequent resurfacing on Earth erodes most of the earlier craters, some are clearly visible such as the one at Arizona, known as the Barringer crater.

But what is a hypervelocity impact? For some people, all the impact speeds above 5 km s^{-1} are considered as hypervelocity, while for others this happens only when the impact speed exceeds the target's and projectile's stress wave speed (whether this speed should be the Hugoniot shock, the low-pressure bulk, the longitudinal, or the shear velocity is not clear). Another definition may be whenever gross plastic flow occurs in a rotational flow pattern and the

stress approximates the Bernoulli law for fluids. However, most people in the field would agree that an impact at 1 km s^{-1} is not hypervelocity but one at 15 km s^{-1} clearly is. The definition may well need to be chosen for the particular phenomenon in test.

One of the materials that is currently being used on spacecraft is glass. It is used in solar panel arrays, space shuttle windows, COLUMBUS viewports of the international space station and in optical sensors looking for missile launch etc. Although it is of increasing importance in space purposes, glass has been a material under study only for the case of ballistic impacts[1)] where the impact velocity rarely exceeds 1 km s^{-1}. Studies of glass under hypervelocity impact are limited. For instance, Alwes (1990)[2)] performed impacts and numerical simulations on glass for testing the glass panes of the COLUMBUS Space Station Viewports. The velocity covered a range of 0.8 to 9.2 km s^{-1}. A later, but questionable, study is performed by McSherry (1996)[3)] where she performed numerical simulations on glass for testing the behaviour of the Hubble Space Telescope (HST) solar arrays. The latest and most complete attempt to study both experimentally and computationally glass under hypervelocity impact comes from Taylor (1996)[4,5)]. She spanned a velocity range of 1.7 to 8.60 km s^{-1}, projectile density of 0.8 to 10 g cm^{-3} and size of 48 to 2500 μm. However, all the above studies were concentrated on the final dimensions of the glass crater.

Because of the high pressures involved during a hypervelocity impact, material from both target and projectile may be ejected, often referred to as the ejecta cloud. This cloud contains material at different states and velocities. The leading edge, which has been subjected to the highest pressures, is usually in a gaseous state followed by melted material and fine grains. Solid pieces of material may follow. In extremely high impact velocities, ion production is possible, if the energy transfer from the impact is high enough to 'strip' the electrons from their atoms. Hot ions and gases, glow and emit light as they cool down to ambient temperatures. There is, therefore, a light flash associated with a hypervelocity impact.

Light flash production - emission from hypervelocity processes can be seen during the night in clear atmospheric conditions. Who has not looked, late at night, at the stars at a clear summer night making a wish when a 'shooting star' appear? However, this 'shooting star' is nothing but a meteoroid entering the Earth's atmosphere. As it enters our planet at immense velocities both meteoroid and atmosphere gases are heated to extreme temperatures. This causes the ionisation of both materials and hence the beautiful phenomenon we have all observed. Large scale impacts on planetary surfaces or natural satellites, except from big craters, also produce large amounts of hot ejecta. Ejecta dust from the impact that exterminated the dinosaurs were

found all over the world. Indeed, Iridium findings at the Cratesious-Tertiary boundary confirmed the hypothesis of the dinosaur extinction by a large impact. Small gravitational differences in the Yucatan peninsula confirmed the exact location of the event. The latest recorded impact happened in Southern Greenland on December 9th 1997, 05.11am local time. The flashes observed in conjunction with the meteorite were so bright as to turn night into daylight at a distance of 100 kilometres and could be compared to the light of a nuclear explosion in the atmosphere[6]. An ever larger scale of impact on another planet (Jupiter) of our Solar System was observed when the comet Shoemaker-Levy 9, disintegrated in orbit by the Jupiter's strong gravitational field, impacted the planet. The fireball of the hot ejected material was seen even by the old space probe Voyager which was 70 A.U. away from the sun.

Light flash production in the laboratory has started with the work by Friichtenicht in 1965[7] and continued with Rollins (1968)[8]. The most detailed study comes from Eichhorn (1975-1978)[9-12]. He used the 2 MV Van de Graaff dust accelerator to accelerate different sub-micron metal projectiles to various metals. He found that the light energy from the flash was dependent on the material. For the same impact velocity and target material, the light energy could vary by a factor of 4 for different projectiles. Although Eichhorn conducted extensive light flash studies for different materials, he limited himself to metals. More recent attempts to study light flash production from materials other than metals come from Burchell et al. (1996)[13-14] where they impacted iron dust onto water ice and Medina et al. (1996)[15] where the target materials were specimen of sunshade and outer lens of sensors (also known as bahngmeters) used on satellites to monitor earth-based launch activity.

The ejecta cloud formation and motion itself has immediate applications to geology and Solar System sciences. It has been suggested in the past that the Moon may be an accumulation of impact ejecta from a primordial mantle of the Earth[16]. In addition, the origin of the majority of asteroids and asteroidal families may be closely related to the impact disruption of the parent bodies and to the ejection of the fragments away from the gravitational field of the planetesimal. The two Voyager missions have shown that water ice is abundant in the outer Solar System and in particular several satellites of the gaseous planets are covered with ice. Impact cratering on these icy satellites will produce ejecta, which if travelling fast enough can escape the parent body. This idea has been put forward as a contributor to the origin of rings of Saturn, Jupiter and Neptune. It thus, becomes apparent that studies of the ejecta cloud such as light flash, ejecta velocities and mass distribution are crucial in the understanding of our Solar System.

As mentioned earlier, if the impact velocity is high enough, materials will ionise and a mass spectrometry of the positive ions can allow the atomic species to be identified. Such a spectrometer is part of the Cosmic Dust Analyser (CDA)[17] which flies on the joint Cassini/Huygens mission to Jupiter. The mission will encounter particles in the interplanetary space and CDA will try to establish its composition. Part of CDA's calibration which took place in the University of Kent at Canterbury included the estimation of the velocity threshold for impact ion production for different projectile-target material combinations[17].

The main research area of this thesis is the study of light flash during a hypervelocity impact process, mainly the temperature of the ejected material, using three techniques; theoretical, experimental and computational. These techniques are divided into three main chapters. A brief description of each chapter is given.

Chapter 2 provides the theoretical background required for the understanding of an impact. The three different stages of a cratering event are summarised and discussed. Material behaviour under dynamical loading and basic shock wave physics are presented. Therefore equation of state theories, basic thermodynamics and constitutive response are discussed and their fundamental equations are described. Finally, a brief description of hydrocodes is also given. Hydrocodes are the available numerical techniques for simulating various impacts and, in general, highly dynamical events.

Chapter 3 uses some of the theoretical foundations established in Chapter 2 to derive the equations needed for calculating the ejecta cloud temperatures and velocities from first principles. For that reason a simple computer program has been written based on these principles. These equations, together with the code, are then used to estimate the ejecta cloud temperature when iron impacts soda-lime glass. In addition, the same program has also been used to estimate the velocity threshold for ion production needed for the calibration of the CDA, since the same physics applies. Finally, as part of the theoretical calculations, ejecta velocity for icy surfaces are made using the same principles.

Chapter 4 describes experiments performed using the 2 MV Van de Graaff dust accelerator facility of the University of Kent at Canterbury. Iron dust particles were accelerated towards a glass target. Velocities in the range 5-20 km s^{-1} were attained for particles of mass 10^{-17} - 10^{-14} kg. The intensity of the resulting light flash was then measured for two different wavelengths and the temperature of the ejecta cloud was found assuming black body radiation emission.

Chapter 5 describes the equations used by hydrocodes to calculate temperatures and compare them against the equations derived in chapters 2 and 3. As established from chapter 2, hydrocode simulations require parameters that are unique for each material. That is why a simple model for glass is presented. This model is then calibrated against experimental results performed by Taylor (1996)[4] and compared against hydrocode results[5] using the Johnson-Holmquist (J-H) brittle material model[5] already explained in chapter 2. Differences between results on experiments and simulations are presented and discussed. Suggestions for further development of the J-H model are also given.

Both ways of calculating temperatures (hydrocode and theory from chapters 2 and 3) seem to be equivalent and although the theory behind hydrocode temperature calculations are rigorous, there were several deficiencies that prevented accurate calculations of temperature. These deficiencies are presented and discussed.

Finally, chapter 6 provides the conclusions of this 3 year research program and gives future suggestions for continuing the project.

References

1. Bourne N K and Rosenberg Z. (1996), 'The Dynamic Response of Soda-Lime Glass', Proc. Conf. AIP on Shock Compression of Condensed Matter, Seatlle, Washington, 567-572.
2. Alwes D, (190), 'Columbus Viewport Glass Pane Hypervelocity Impact Testing and Analysis', *Int. J. Impact Engng*, **10**, 1-22.
3. McSherry F, (1995), 'Numerical Simulations of Hypervelocity Impacts on Solar Arrays', ESA Study Contract Report, No 11693/95/NL/JG.
4. Taylor E A, (1996), 'Experimental and Computational Study of Hypervelocity Impact on Brittle Materials and Composites', University of Kent at Canterbury, Ph.D. thesis.
5. Taylor E A, et al., (1997), 'Hydrocode Modelling of Space Debris Hypervelocity Impact on Soda-Lime Glass using the Johnson-Holmquist Brittle Material Model', Proc. 2nd Eur. Conf. Space Debris, Darmstadt, Germany, 449-453.
6. Neils Bohr Institute, Geophysical Dept., (1997), 'Greenland Meteorite Fall Update', Press Statement.
7. Friichtenicht H, (1965), NASA Report 4158-6015.

8. Rollins T L and Jean B, (1968), 'Impact Flash for Micrometeoroid Detection', Computing Devices Report 9899/FRI, NASA Contr. NAS9-6790.
9. Eichhorn G, (1975), 'Measurements of the Light Flash Produced by High Velocity Particle Impact', *Planet. Space Sci.*, **23,** 1519-1525.
10. Eichhorn G, (1976), 'Analysis of the Hypervelocity Impact Process from Impact Flash Measurements', *Planet. Space Sci,* **24,** 771-781.
11. Eichhorn G, (1978), 'Heating and Vaporisation during Hypervelocity Particle Impact', *Planet. Space Sci.*, **26,** 463-467.
12. Eichhorn G., (1978), 'Primary Velocity Dependence of Impact Ejecta Parameters', *Planet. Space Sci.*, **26,** 469-471.
13. Burchell M J, et al., (1996), 'Light Flash and Ionisation from Hypervelocity Impacts on Ice', *Icarus*, **122,** 359-365.
14. Burchell M J et al., (1996), 'Use of Combined Light Flash and Plasma Measurements to Study Hypervelocity Impact Processes', *Adv. Space Res.*, **12,** (12)141-(12)145.
15. Medina D F , et al., (1996), 'Reconstruction of a Hypervelocity Impact Event in Space', Proc. on the Characteristics and Consequences of Orbital Debris and Natural Space Impactors, Denver, Colorado, USA, 137.
16. Cameron A G W and Ward W R, (1976), 'The Origin of the Moon', *Lunar Science VII,* 120-122.
17. Ratcliff P R, et al., (1992), 'The Cosmic Dust Analyser', *J. British Interplanetary Soc.*, **45,** 355-358.
18. Ratcliff P R, et al., (1996), "Velocity Thresholds for Impact Plasma Production', *Adv. Space Res.*, **20,** 1471-1476.

CHAPTER 2

Hypervelocity Impact Dynamics

2.1 Introduction

The formation of a crater starts when the impactor first contacts the target and finishes with the final motions of the material inside the crater and the deposited debris around the rim. There are different physical processes that govern crater formation throughout its duration. For instance, during the first moments of the impact, the energy transfer can be so immense that both projectile and target may melt and/or vaporise. Therefore, a good description of their thermodynamic properties is required. However, different materials exhibit different strength under shock loading. Hence, material characterisation under dynamic loading is also important in the process of impact formation. In addition, in the case of planetary impacts, gravity of the target becomes important in the development of the final dimensions of the crater and the deposition of the debris around the crater rim and around the planetary body as well. Therefore, one can say that crater formation is a very complicated phenomenon. If the process could be split into different regimes where various types of physical behaviour dominate, then it should be easier to comprehend.

Although the duration of the process may vary according to the dimensions of the projectile and target, in general, is very short. For a planetary impact, it is of the order of a few

minutes, while for an impact in a laboratory, it may last only a few microseconds. In any case, it is impossible to study real cratering events in a precise detail. That is why, numerical modelling is very often used. Special computer packages have been developed, usually referred to as hydrocodes, which deal with non linear processes such as impacts.

The goal of this chapter is to review some of the principles that govern an impact process and its modelling. For that reason this chapter is divided into three main sections. The first gives an overview of the model, first proposed by Gault et al. (1968)[1)] and described in Melosh (1989)[2)] for the three stages of an impact (contact or compression, excavation and modification). The second section describes the behaviour of the materials during these stages. Finally, an overview is given concerning hydrocodes, i.e. what they are and how they can be used to give an insight about an impact process.

2.2 Stages of a Cratering Process

2.2.1 Contact and Compression Stage

This first stage of impact cratering begins when the projectile contacts the target surface. Shock waves propagate to both impactor and target originating at the point (or points for irregular impactors) where the projectile first touches the target's surface. Shock pressures developed during the early stages generally reach hundreds of GPa and thus far exceed the yield strength of both projectile and target. Therefore, both materials can be treated as fluids. The maximum pressure at the interface can be found using the Hugoniot relations, which relate the properties of the material behind and ahead of the shock. These are explained in section 2.3.2. The travelling shock front contributes to the deceleration of the projectile while the forward travelling shock will compress the target material. The shock wave traversing the projectile reaches its rear surface after time $t = L / u_{sp}$ where L is the diameter of the projectile and u_{sp} is the shock wave speed in the projectile material. When it reaches the rear surface, it is reflected back into the compressed projectile material as a rarefaction or release wave. Spallation, may eject a small fraction of the projectile's rear as lightly shocked debris, but most of the projectile unloads from high pressure and thus expands, usually, into the melt and/or vapour regime. This is discussed in more detail in section 2.3.3.7. The unloading phase ends when the rarefaction reaches the projectile-target interface. The rarefaction, travelling at speed c_R with respect to the projectile, must traverse its compressed thickness $(\rho_0/\rho)L$ and so the duration of the unloading phase is t_R

$=(\rho_0/\rho)L/c_R$, where ρ_0 and ρ are the densities of the unshoched and shocked projectile material, respectively. In addition, there are release waves from the lateral surfaces, as well. Thus, the projectile is essentially turned inside out and residues may be smeared out along the inside of the rapidly expanding crater cavity. In this stage, most of the projectile's initial kinetic energy is transferred to the target.

But release waves emanating from the target free surfaces are travelling inside it as well. Thus from the interface vaporised target material may eject. For extreme conditions, even plasma production is possible for both materials.

Contact and compression is the shortest of all the stages, lasting only as long as the shock wave and subsequent rarefaction take to transverse the projectile. Its duration depends upon the projectile's size, composition, and impact velocity. It may be as brief as a nanosecond, for an 1μm particle impacting at 2 km s^{-1}. Since the time scale of this stage is very short, the crater in the target has not evolved much. In fact only a small fraction of it is opened during this stage. Most of the crater formation takes place in the subsequent excavation stage.

2.2.2 Excavation Stage

The excavation stage comes immediately after the contact and compression stage ends. During this stage a more-or-less hemispherical wave propagates into the target. This shock and the following rarefaction set target material in motion, initiating a subsonic excavation flow that eventually opens the crater. The shock wave expands and weakens, decaying to an elastic wave as it engulfs more target material. The velocity acquired by the material is directed radially away from the impact site immediately behind the shock wave. However, rarefaction waves propagating downward from free surfaces create an upward directed pressure gradient behind the shock, which adds an upward component to the radial velocity, ultimately producing an upward and outward excavation flow. Near the impact site, where the pressure is high the target may vaporise or melt upon unloading. However, as we go further inside the target the shock wave is reduced to a stress one and material is simply ejected from the target because of the excavation flow.

The masses and temperatures of melted or vaporised material are determined almost exclusively by the dynamics of the expanding shock wave. However, by contrast, the shape and size of the final crater are almost exclusively determined by the details of the excavation flow,

and its interaction with the target's strength. Thus, for a full description of impact processes, strength models should be introduced (discussed in section 2.4).

2.2.3 Modification Stage

The modification stage begins after the crater has been fully excavated. Reactions in the target may happen, once stress waves have been attenuated to a level that no longer causes flow or gross plastic deformation. The more important of such target reactions are elastic/inelastic recovery of the crater; brittle spalling at the free surface of the crater and recrystallisation of the material in the area beneath the visible crater.

As the dimensional scales increases, one may go from strength dominated regimes to ones were gravity has a significant role to play[3)] . Hence, collapse due to gravity may happen: slump terraces form on the wall and central peaks rise in the interior. Great mountain rings may appear in and around still larger craters.

2.3 Material Characterisation under Shock Wave Loading

2.3.1 Introduction

In this section a way to calculate temperatures from first principles of the material under shock wave loading will be presented using Equation Of State (EOS) theories. However, before doing so, a description of shock waves and EOS theories are needed.

In 3-D (x,y,z) space the state of stress in a continuous medium is defined at a given point by six stress components: σ_{xx}, σ_{yy}, σ_{zz}, σ_{xy}, σ_{yz}, σ_{zx} . However, it is possible to choose a rotated set of co-ordinate axes so that $\sigma_{xy}=\sigma_{yz}=\sigma_{zx}$. Any three orthogonal axes that satisfy this condition are called principal axes for the given point. The stresses in the direction of the principal axes on surfaces normal to these axes are called principal stresses and are usually denoted by σ_1, σ_2, and σ_3 and the shear stresses $\sigma_{12}=\sigma_{23}=\sigma_{31}=0$. Each of the stresses is usually described in terms of an average stress, assumed to be the hydrostatic pressure, and a deviatoric (plasticity) term which is related to the shear stress in plane shock propagation. The stress components are given by

$$\sigma_i = -P + S_i \qquad \forall\, i = 1,2,3 \tag{2.3.1.1}$$

where P is the hydrostatic pressure (defined as the negative mean of the three principal stresses, i.e. $-P=(\sigma_1+\sigma_2+\sigma_3)/3$) determined by Equation of State Theories (EOS) and S_i are deviator stresses described by Strength Models. The negative sign for the hydrostatic pressure P follows

from the usual notation that stresses are positive in tension and negative in compression (the opposite to that for pressure).

As with the stresses, the strain components e_i are defined as the sum of a mean normal strain ε and deviatoric strain components θ_1, θ_2, and θ_3, that is

$$e_i=-\varepsilon+\theta_i\ ,\ \forall\ i=1,2,3 \qquad (2.3.1.2)$$

and $\varepsilon=-(e_1+e_2+e_3)/3$, with similar expressions for the strain rate components.

From the above equations we can derive:

$$s_1+s_2+s_3=\theta_1+\theta_2+\theta_3=0 \qquad (2.3.1.3)$$

The concept of elastic distortion is that if the material is loaded and subsequently unloaded, all the distortion energy is recovered and the material will come to its initial state. However, real materials are unable to support large shear stresses. If the distortion is too great, the material will reach its elastic limit and begin to distort non-elastically. If the material is subsequently unloaded only the elastic distortion energy will be recovered and the material will suffer permanent plastic strain. The transition to the plastic flow and the description of the elastic limit is given by the von Mises criterion[4]. It is a simple and convenient criterion to apply in that it defines a smooth and continuous yield surface and is a good approximation at high stress levels. The von Mises criterion states that, given the principal stresses σ_1,σ_2 and σ_3 the local yield condition is

$$(\sigma_1-\sigma_2)^2+(\sigma_2-\sigma_3)^2+(\sigma_3-\sigma_1)^2=2Y^2 \qquad (2.3.1.4)$$

where Y is the yield stress in a state of uniaxial stress. Using Equation. (2.3.1.1) the above relation can be written as

$$(s_1-s_2)^2+(s_2-s_3)^2+(s_3-s_1)^2=2Y^2 \qquad (2.3.1.5)$$

which with Equation. (2.3.1.3) may be reduced to

$$s_1^2+s_2^2+s_3^2=2Y^2/3 \qquad (2.3.1.6)$$

Thus the onset of yielding, i.e. of plastic flow, is purely a function of the deviatoric stresses (distortion) and does not depend upon the value of the local hydrostatic pressure unless the yield stress Y itself is a function of pressure, as is the case for some strength models discussed later.

Consider, now, the uniaxial strain state for an elastic-perfectly plastic material (no strain hardening). A body is in a state of uniaxial, or one-dimensional, strain when deformation is confined solely to one direction. For example, flyer plate impact experiments performed to characterise material properties, provide a uniaxial strain condition state because deformation cannot occur in directions normal to the direction of motion. Thus $e_2=e_3=0$ and $s_2=s_3=-s_1/2$. If, in

addition the maximum shear stress τ the material can withstand is $(\sigma_1-\sigma_2)/2$, then from Equations (2.3.1.1) through (2.3.1.6) we get that

$$\sigma_1=P+4\tau/3 \qquad (2.3.1.7)$$

Therefore the longitudinal stress is shared between the average hydrostatic pressure and the superimposed shear. However, for an elastic-perfectly plastic material the shear strength is constant. Hence, if σ_1 is much higher than the shear strength, Equation (2.3.1.7) gives the approximation that $\sigma_1 \approx P$. Thus the material has no significant strength and behaves almost like a fluid. This is the case for most planetary impacts where the impact velocity can reach 30 km s^{-1}.

Let us now give a definition of a shock wave. Consider first a typical stress vs. strain curve, illustrated in Figure 2.1. The slope at each point on the curve represents speed propagation of a wave. Thus all the waves up to the elastic limit will travel at the same velocity governed by the slope of OA, i.e. $C_e=[(K+4G/3)/\rho_0]^{1/2}$. However, if B represents the maximum stress in an impact, a dual wave structure will develop. A somewhat slower moving plastic wave travelling at a velocity governed by the slope AB, will follow the elastic precursor travelling at C_e. Because the stress-strain curve for most materials is concave up, as shown in Fig. 2.1, a stress level will be reached, point C, where the elastic and plastic waves have the same velocity. In this case, we have an elastic precursor and a plastic wave moving together at a velocity given by the slope OC which is identical to the slope OA. Finally, at even higher pressures, point D, only a single plastic wave exists which travels at a velocity, governed by the slope OD, which exceeds the elastic precursor velocity. In this case, we talk about a shock wave (pressure discontinuity) travelling inside the material.

Figure 2.1: Stress-Strain Relation showing Elastic-Plastic Material Response

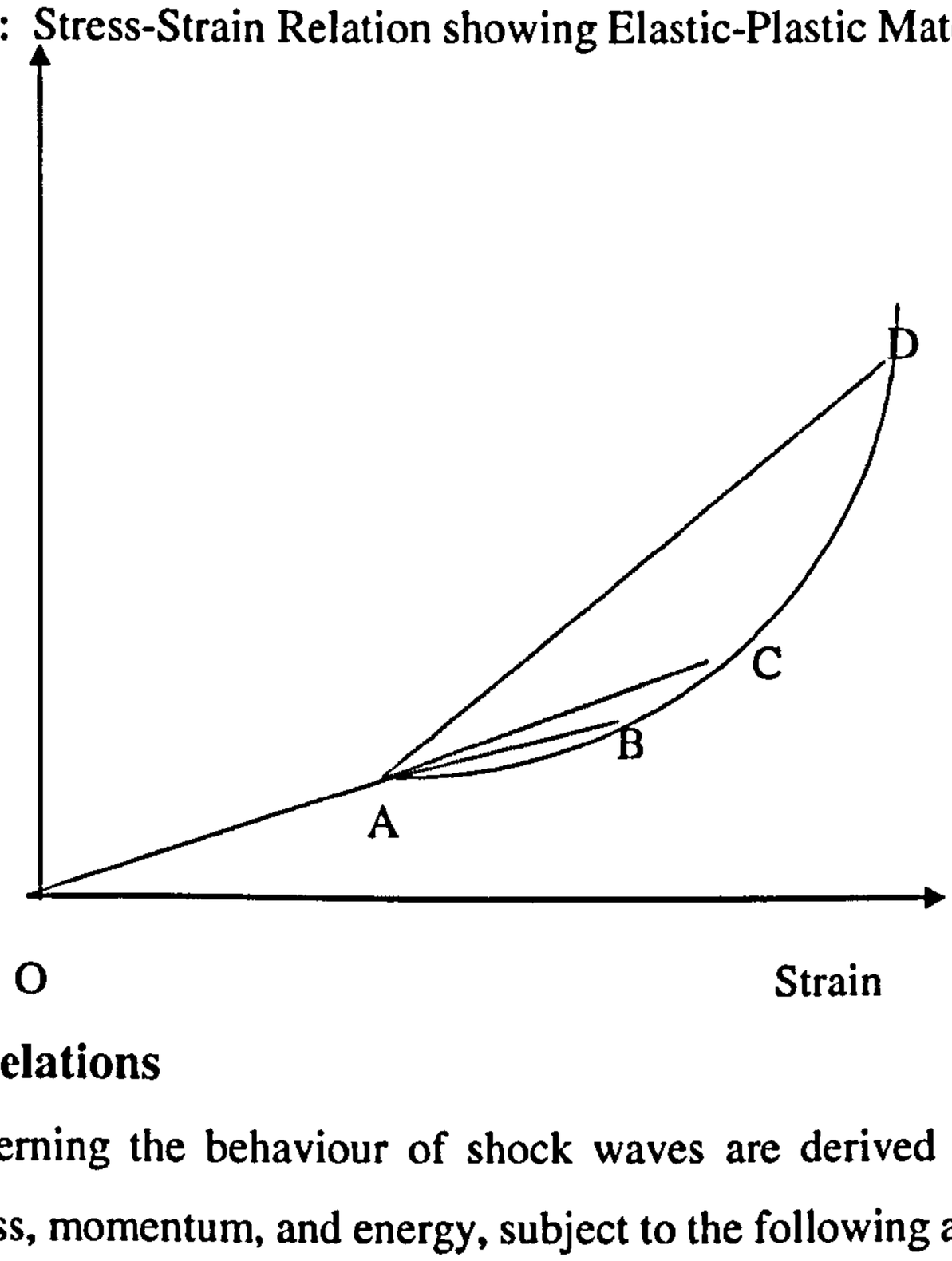

2.3.2 Hugoniot Relations

The equations governing the behaviour of shock waves are derived by applying the laws of conservation of mass, momentum, and energy, subject to the following assumptions:

a) The shock front is a discontinuity;

b) There is thermodynamic equilibrium immediately ahead and behind the shock front.

The derivation of the Hugoniot relations is given in the Appendix A. Here we present only their formulation.

- From mass conservation:

$$\rho_0 u_s = \rho (u_s - u_p) \qquad (2.3.2.1)$$

- From momentum conservation:

$$\sigma - \sigma_0 = \rho_0 u_s u_p \qquad (2.3.2.2)$$

- From energy conservation:

$$E - E_0 = \tfrac{1}{2} (\sigma + \sigma_0) (V_0 - V) = u_p^2/2 \qquad (2.3.2.3)$$

where σ_0, ρ_0, V_0, E_0, are the longitudinal stress, density, specific volume and specific internal energy before the shock respectively, σ, ρ, V, E are the values after the shock, u_s is the shock velocity, and u_p is the velocity that the material has acquired after the shock has passed. However, for large pressures, the above stress may be interchanged with the hydrostatic pressure P, and a third assumption is added, that is, the material has no strength. The above equations have five unknown variables, namely, u_s, ρ, u_p, σ and E. We add a fourth equation to the three

above, the Equation Of State (EOS) which relates P, V, and E. This will be discussed in the following section. Finally, a fifth equation comes from shock wave experiments which showed that a simple relation exists between the shock and particle relation, that is

$$u_s = c_0 + Su_p \,. \tag{2.3.2.4}$$

Where c_0 is the low pressure bulk sound speed for a material with no shear strength, i.e. $c_0 = (K/\rho)^{1/2}$, K is the bulk modulus and S is an experimentally determined material constant. This linear relation often provides a good description up to 10 km/s. At higher velocities, and thus higher pressures, U_s is more commonly written in the form

$$u_s = a + bu_p + cu_p^2 \,, \tag{2.3.2.5}$$

with a,b,c constants.

Departures from linearity of Equation (2.3.2.4), were usually traced to porosity, or phase transitions.

Using the Hugoniot relations, that is Equations (2.3.2.1) - (2.3.2.2), with Equations (2.3.2.4) or (2.3.2.5) is possible to obtain an expression for the shock pressure with respect to the volume.

$$P_H(V) = \frac{c_0^2(V_0 - V)}{\left[V_0 - S(V_0 - V)\right]^2} \tag{2.3.2.6}$$

$$P_H(V) = \frac{2a^2(V_0 - V)}{\left\{\left[V_0 - b(V_0 - V)\right]^2 - 2ac(V_0 - V)^2 + \left[V_0 - b(V_0 - V)\right]\sqrt{\left[V_0 - b(V_0 - V)\right]^2 - 4ac\left[V_0 - b(V_0 - V)\right]^2}\right\}} \tag{2.3.2.7}$$

The above expressions constitute the principal Hugoniot curves for a given material. However, although the Hugoniot curves are described by an equation of the form P = P(V), each point on that curve has a value of E associated with it. It is thus a locus of possible shock states and not the thermodynamic path that the material will follow in order to reach the final state. That is, it was assumed that the shock front is a discontinuity, hence the material 'jumps' from the original state to the final one given by the Hugoniot curve along a line connecting the two states known as the Rayleigh line.

Finally, it is possible to derive an expression between the impact velocity U_0 and the shock pressure P_H , using the Hugoniot relations. Immediately after first contact (in the beginning of the contact and compression stage), two shocks propagate away from the interface, one travelling into the projectile and the other travelling downward into the target. The shocks inside

the target and projectile are both raised to the same high pressure and must travel together with the same particle velocity, since neither interpenetration nor separation can occur. The unshocked projectile is moving at U_0 in the target's rest frame, so that if u^p_p is the particle velocity behind the shock in the projectile's rest frame, then the same material moves at speed $(U_0 - u^p_p)$ from the target's point of view. Similarly, if the shock wave in the projectile moves at speed u^p_s with respect to unshocked projectile material, then it moves at $(U_0 - u^p_s)$ with respect to the target. The equality of particle velocity in both projectile and target thus requires

$$u^t_p = U_0 - u^p_p \tag{2.3.2.8}$$

where u^t_p is the change in particle velocity across the shock in the target. Using the above equation, together with the first Hugoniot relations for both projectile and target we may deduce that

$$U_0 = \left[1 + \left(\frac{V^t_0 - V^t_H}{V^p_0 - V^P_H}\right)^{\frac{1}{2}}\right] * \sqrt{P\left(V^P_0 - V^P_H\right)} \tag{2.3.2.9}$$

Let as consider a specific example. Suppose that a stainless steel projectile of density 7.896 g/cm^3 impacts a 2024 aluminium target of density 2.785 g cm^{-3}. If the pressure is 100 GPa, then the impact velocity using Equation (2.3.2.9) is 5.32 km/s.

2.3.3 Equation Of State Theories

An EOS is a functional relationship of the thermodynamic variables hydrostatic pressure P, density ρ (or specific volume V=1/ρ), and specific internal energy E. It can be written as f(P,V,E) =0 and represents a surface in the PVE space, The PV isotherm (T=constant), isentrope (S=constant), and shock Hugoniot (the locus of all possible states that can be reached by using a single shock from a given initial state) are particular curves on this surface. The EOS is different for different materials.

In order to construct an EOS we can divide the problem into separate and tractable parts[5]. The simplest problem is one in which there are no phase transitions or chemical reactions. For a single phase and a single chemical component, it is common to assume that the thermodynamic functions can be written as the sum of several terms that are approximately independent of each other. The Helmholtz free energy is then given by

$$F(\rho, T) = E_c(\rho) + F_T(\rho, T) \tag{2.3.3.1}$$

The pressure P and internal energy E can be written in a similar form. Definitions of the terms in Equation (2.3.3.1) are most easily given for a solid. E_c is the internal energy of the zero-Kelvin isotherm, that is the energy of the system when all the electrons are in the ground state and the nuclei in a perfect lattice. This term accounts for both cohesive forces that give rise to condensed phases and the repulsive forces that determine most of the response to compression.

Atoms in a material are set into motion by heating. That is, a definite energy and pressure are connected with the thermal motion of the atoms. At temperatures of the order of thousands of degrees and above, the thermal excitation of the electrons plays an important role. The second term F_T of Equation (2.3.3.1) corresponds to thermal contributions. This term can be broken up into three parts. One part corresponds to vibrations of atoms (or rather their nuclei) about their equilibrium lattice positions. The second part is for molecular substances (the contribution from internal vibrational and rotational degrees of freedom should be taken into account). The last contribution is due to thermal excitation and ionisation and becomes important at high temperatures.

Even in the 'normal' region when the material is shock-compressed by a factor of 2 ($\rho / \rho_0 = 2$ and $P \approx 0.1 - 0.2$ TPa), the irreversible shock heating leads to a temperature rise of a few electron volts. These temperatures are much higher than the melting temperature at normal density. We can extrapolate the above theory to the liquid regime by neglecting the effects of liquid disorder, on the basis that at any given instant the local environment experienced by an atom in a liquid is about the same as in the corresponding solid. However, for satisfactory results, models based on the condensed matter theories cannot be extrapolated very far into the fluid range without some changes. Realistic theories of liquids and dense gases have become available only recently and still have limitations. For further information one can refer to SK Sikka et al. (1983)[6] or J Hama and K Suito (1996)[7]. For this reason, this work deals only with the relatively simple but heavily used EOSs such as the Mie-Gruneisen and Tillotson.

2.3.3.1 The Mie-Gruneisen EOS

Perhaps, the most heavily used EOS is the Mie-Gruneisen EOS[8]. If the pressure is low enough so that the thermal excitation and ionisation contribution to the specific internal energy is insignificant then it may be deduced from statistical mechanical considerations that the EOS has the following form:

$$P = -\frac{de_c}{dV} + \frac{\gamma(V)}{V} e_T(V,T) = P_c(V) + \frac{\gamma(V)}{V} e_T(V,T) \qquad (2.3.3.2)$$

$$\text{and} \qquad e = e_c(V) + e_T(V,T) \qquad (2.3.3.3)$$

where $e_c(V)$ is the cold curve (the contribution from the zero-Kelvin isotherm), $\gamma(V)$ is the Gruneisen coefficient, and $e_T(V,T)$ is the contribution to the energy due to kinetic and potential energy of the atoms whose mass resides almost entirely in their nuclei, that is the thermal energy. Combining the above equations we get the Mie-Gruneisen EOS:

$$P = P_c(V) + \frac{\gamma(V)}{V}\left(e - e_c(V)\right) \qquad (2.3.3.4)$$

If we assume the Debye model for a solid, where the vibrational energy levels of a system are assumed to be those of harmonic oscillators, then the internal energy and pressure can be written as[6,9]:

$$E = 3k_B De(\theta_D / T) \approx 3k_B T \ \text{ for } T \geq \theta_D \qquad (2.3.3.5)$$

$$\text{and} \qquad P_T = \frac{\gamma(V)}{V} E_T \qquad (2.3.3.6)$$

Here $De(\theta_D/T)$ is the Debye function and θ_D is the Debye temperature.

In this case γ is defined as:

$$\gamma = -\left\langle \frac{d \ln \nu_i(V)}{d \ln V} \right\rangle \qquad (2.3.3.7)$$

The ν_i's are the lattice frequencies and $\langle\rangle$ represents the average over the 3N normal modes of the solid. These frequencies and hence γ are assumed to be independent of the temperature and are functions of volume only.

The Gruneisen coefficient which is the ratio of thermal pressure to the thermal energy of the lattice, can be related to the other thermodynamic properties of the material. Differentiating (2.3.3.6) with respect to temperature at constant volume we get :

$$\gamma = \frac{V}{C_v}\left(\frac{\partial P}{\partial T}\right)_v = V\left(\frac{\partial P}{\partial E}\right)_v \qquad (2.3.3.8)$$

Using the thermodynamic identity:

$$\left(\frac{\partial P}{\partial T}\right)_V\left(\frac{\partial T}{\partial V}\right)_P\left(\frac{\partial V}{\partial P}\right)_T = -1 \qquad (2.3.3.9)$$

we have:

$$\gamma = -\left(\frac{V}{C_v}\right)\left(\frac{\partial P}{\partial V}\right)_T\left(\frac{\partial V}{\partial T}\right)_P \qquad (2.3.3.10)$$

However, $-(1/V_0)(\partial V/\partial P)_T=\kappa_0$ is the isothermal compressibility of the material at standard conditions, and $(1/V_0)(\partial V/\partial T)_P=\alpha$ is the coefficient of thermal expansion at constant pressure. Therefore the Gruneisen coefficient for a body at standard volume $\gamma_0\equiv\gamma(V_0)$ may be written as:

$$\gamma = \frac{V_0\alpha}{C_v\kappa_0} \equiv \frac{\alpha}{\rho_0 C_v\kappa_0} \equiv \frac{\alpha c_0^{\,2}}{C_v} \qquad (2.3.3.11)$$

(c_0 is the speed of sound determined from the isothermal compressibility).

Further, under various assumptions for the force field in solids, several authors have derived formulae for γ in a Debye solid in terms of the cold curve . They are the Slater model (or Slater-Landau model)[10], Dugdale-MacDonald model[11], and Vaschenko-Zubarev model[12]. Thus γ is given by:

$$\gamma = \frac{t-2}{3} - \frac{V}{2}\frac{\frac{d^2}{dV^2}\left(P_c V^{\frac{2}{3}t}\right)}{\frac{d}{dV}\left(P_c V^{\frac{2}{3}t}\right)} \qquad (2.3.3.12)$$

where t=0 →Slater

t=1 →Dugdale-MacDonald

t=2 →Vaschenko-Zubarev.

Thus, the volume variation of $\gamma(V)$ can be evaluated from the 0 K isotherm. More recently, Migault (1971 and 1972)[13,14] and Romain et al. (1979)[15] suggested that parameter t may be a material parameter having continuous values. However, a knowledge of the cold curve is required in order to find $\gamma(V)$. Formulae for that can be constructed by either semi-empirical calculations, or by quantum-mechanical theories[6].

It has been observed from these shock wave analyses that for small compression's, γ is nearly inversely proportional to the density, that is $\rho_0\gamma_0=\rho\gamma$. This is a very useful result and is used to find γ at any particular point on the Hugoniot curve without using Equation (2.3.3.12); ie. we simply use Equation (2.3.3.11) together with tables of measured Hugoniot data. Many authors

combined the above result with the fact that at large compressions the limiting value of γ for all materials is 2/3 (i.e. as for a free mono-atomic gas) to obtain formulae for $\gamma(V)$. Some of the resulting approximations for γ are

SESAME[16)]
$$\gamma = \gamma_0\rho_0/\rho + \frac{2}{3}\left(1-\rho_0/\rho\right) \qquad (2.3.3.13)$$

Thomson & Lauson[17)]
$$\gamma = \gamma_0\rho_0/\rho + \frac{2}{3}\left(1-\rho_0/\rho\right)^2 \qquad (2.3.3.14)$$

Royce[18)]
$$\gamma = \gamma_0 - a\left(1-\rho_0/\rho\right) \qquad (2.3.3.15)$$

where a is a material-dependent constant.

A rather interesting and useful approach of finding Gruneisen coefficients was derived by K. Nagayama and Y. Mori (1994)[19)] based on Equation (2.3.3.12). They introduced a new variable q_s which is given by

$$q_s = \left\{\frac{\partial\left[P\left(\rho/\rho_0\right)^{-\frac{2}{3}t}\right]}{\partial\rho}\right\}_s \qquad (2.3.3.16)$$

where t is the parameter of Equation (2.3.3.12) and is defined as the derivative with respect to density along an isentrope. Then they used the linear shock-particle velocity relation (that is $U_s=c_0 + su_p$, where U_s and u_p are the shock wave and material particle velocities respectively, c_0 is the low pressure bulk sound speed, and s is an experimentally determined material constant) to obtain:

$$q_s = \left(\frac{u_s-u_p}{u_s}\right)^{\frac{2}{3}t}\frac{\left(u_s-u_p\right)^2}{c_0}\left(u_s+Su_p-\frac{2}{3}t\frac{c_0u_p}{u_s-u_p}-\gamma\frac{Su_p^2}{u_s-u_p}\right) \qquad (2.3.3.17)$$

$$\gamma = \frac{t+1}{3}\frac{u_s\left(u_s-u_p\right)}{2c_0}\left(\frac{\partial\ln q_s}{\partial u_p}\right)_H \qquad (2.3.3.18)$$

(the H denotes differentiation along the Hugoniot).

They developed a computer code which solves the above equations and thus gives γ at any point on the Hugoniot. The code is given in the Appendix C and has been used in section 3.5 to estimate values of γ for glass at the initial density ρ_0.

Sometimes, the shock wave data to regions off the Hugoniot are required and the Gruneisen form of equation of state is a convenient way of accomplishing this. In general, the hydrostatic pressure is a function of specific volume and internal energy. That is P≡P(V,E). Thus:

$$dP = \left(\frac{\partial P}{\partial V}\right)_E dV + \left(\frac{\partial P}{\partial E}\right)_V dE \qquad (2.3.3.19)$$

Integrating at constant energy from V_r to V and then at constant volume from E_r to E gives:

$$P = P_0 + \int_{V_0,E_0}^{V,E_0}\left(\frac{\partial P}{\partial V}\right)_E dV + \int_{E_0,V}^{E,V}\left(\frac{\partial P}{\partial E}\right)_V dE \qquad (2.3.3.20)$$

From Equation (2.3.3.8) $\left(\frac{\partial P}{\partial E}\right)_V = \frac{\gamma(V)}{V}$.

If $P_0 + \int_{V_0,E_0}^{V,E_0}\left(\frac{\partial P}{\partial V}\right)_E dV = P_r(V)$ then Equation (3.3.20) becomes:

$$P = P_r(V) + \frac{\gamma(V)}{V}\left(E - E_r(V)\right) \qquad (2.3.3.21)$$

This equation has the form of Equation (2.3.3.4) and all the EOS of similar form are called Mie-Gruneisen EOS. The above equation gives the pressure of a material with respect to some reference curve $P_r(V)$. It is obvious that when the required pressure is the Hugoniot, then the $P_r(V)$ is the cold curve. However, sometimes, pressure is needed along other curves (e.g. the release adiabat). In this case, the reference curve is taken to be the Hugoniot curve, thus:

$$P = P_H(V) + \frac{\gamma(V)}{V}\left(E - E_H(V)\right) \qquad (2.3.3.22)$$

The Hugoniot and cold curves are related by:

$$P_H(V) = \frac{(\kappa - 1)P_c(V) - 2E_c(V)/V}{\kappa - V_0/V} \qquad (2.3.3.23)$$

where $\kappa = 2/\gamma + 1$.

The Mie-Gruneisen EOS is an accurate thermodynamic description of most metals in the solid regime, because it has its origin in the theory of condensed matter. Sometimes, it can be extended to liquid region because of the assumption that the local environment experienced by an atom in a liquid is about the same as in the corresponding solid. However, it gives poor results at high pressures when a material reaches the expanded liquid and the vapour regions. This is because, as the energy increases, the assumption that the Gruneisen coefficient is a function only of density is no longer valid; the dependence of γ on temperature becomes important when

electron excitation or chemical reactions occur. To avoid the above problems, Tillotson developed an analytic EOS (applicable to hypervelocity impacts) which will be discussed in section 2.3.3.4.

2.3.3.2 Perfect Gas EOS

Perfect gas is an idealised state of a material and its pressure is given by:

$$P=(\gamma-1)\rho E \qquad (2.3.3.24)$$

where γ is the ratio of the specific heat at constant pressure to that at constant volume, $\gamma=C_p/C_v$. The constant γ is determined by the number of internal degrees of freedom possessed by the gas molecules.

Compare Equation (2.3.3.24) with (2.3.3.4). We can see that the thermal part of the Mie-Gruneisen EOS is $P_T=\gamma(V)\rho E_T$, which is of the same form as (2.3.3.24), where $\gamma(V)=\gamma-1$. Thus, the thermal pressure in the Mie-Gruneisen EOS is similar to that of a perfect gas, while there is also pressure due to bulk compression.

2.3.3.3 Thomas-Fermi High Pressure Limit

As a solid is compressed, its nuclei are pushed closer together and thus electrons become more energetic. Eventually, a point will be reached where all the atoms are ionised and the solid is essentially an electron gas in which the nuclei serve mainly to ensure charge neutrality. Most of the pressure is due to the electrons. The pressure of a cold solid under these circumstances is given by:

$$P=\frac{h^2}{5m_e}\left(\frac{3}{8\pi}\right)^{\frac{2}{3}}\left(\frac{\rho Z N_0}{\mu}\right)^{\frac{5}{3}} \qquad (2.3.3.25)$$

where h is Planck's constant, m_e is the electron mass, Z is the mean atomic number of the solid, μ is the mean atomic weight, and N_0 is Avogadro's number.

The significance of both perfect gas EOS and Thomas-Fermi high-pressure will become apparent in the following section.

2.3.3.4 The Tillotson EOS

Tillotson[20] developed a formula that uses separate expressions in different regions of the EOS space. For the compression region and cold expanded states, where the energy density is less than the energy of incipient vaporisation ($E<E_{iv}$), he generalised the Mie-Gruneisen EOS by allowing γ to decrease with increasing E. This was to account for the effects of thermal electronic excitation; the expression and constants were chosen to fit the Thomas-Fermi results. Thus:

$$P_c = \left\{a + \frac{b}{E/\left(E_0\eta^2\right)+1}\right\}\rho E + A\mu + B\mu^2 \qquad (2.3.3.26)$$

where $\eta=\rho/\rho_0$, $\mu=\eta-1$. The constants a, b, and A being derived from shock experiments and E_0 and B are adjusted to give the best fit for the EOS surface. In spite of the notation, E_0 is *not* the initial energy density of the substance; it is merely a parameter that is often close to the vaporisation energy. The initial energy density E must, in fact, be zero to ensure that the pressure is zero in the initial state. When the pressure is zero, it can be shown that $(a+b)=\gamma_0$.

Also, the c_0 and S constants of the linear shock-particle velocity model are related with the above constants by $c_0=(A/\rho_0)^{1/2}$. A is thus equal to the low pressure bulk modulus sound speed and $S=\frac{1}{2}\left(1+\frac{B}{A}+\frac{a+b}{2}\right)$. Equation (2.3.3.26) represents the situation in which a substance is shocked to a sufficiently low pressure that it remains solid when it returns adiabatically to zero pressure.

In expansion, when the internal energy exceeds the energy of complete vaporisation ($E>E_{cv}$), the pressure is given by:

$$P_e = a\rho E + \left\{\frac{b\rho E}{E/\left(E_0\eta^2\right)+1} + A\mu e^{-\beta[\rho_0/(\rho-1)]}\right\}e^{-\alpha[\rho_0/(\rho-1)]^2} \quad . \qquad (2.3.3.27)$$

The constants α and γ control the rate of convergence to an ideal gas. The above equation approaches the ideal gas results at low densities. It is also constructed so that the pressure and its first derivative are continuous with Equation (2.3.3.26) when $\rho=\rho_0$.

However, some trouble may exist because of continuity reasons in the partial vaporisation regime (mixed phase region) when $E_{iv}<E<E_{cv}$, (the subscripts iv and cv stand for incipient and complete vaporisation, respectively). Thus, for the transition to be smooth and continuous a third expression was developed:

$$P = \frac{P_e(E - E_{iv}) + P_c(E_{cv} - E)}{E_{cv} - E_{iv}} . \qquad (2.3.3.28)$$

While the above EOS is easy to use and asymptotically correct (it goes to the Thomas-Fermi result for very high compression, and an ideal gas for large expansion) it does not accurately describe the gas-liquid and liquid-liquid phase transformation regions.

2.3.3.5 Semianalytical Equations Of State

The modern trend in EOS is toward the use of increasingly complex computer codes to generate an EOS that relies on different physical approximations in different domains of validity. One of the best such EOS is the ANEOS code (Thompson and Lauson, 1972). One major advantage possessed by this code over the Tillotson EOS is that in ANEOS the pressure, temperature, and density are derived from the Gibbs free energy, and thus are guaranteed to be thermodynamically consistent. On the other hand, pressures computed by the Tillotson EOS[2)] may not satisfy thermodynamic consistency, especially when phase changes occur. The Tillotson EOS also cannot correctly represent the pressure and density changes in a two-phase region, as when gas and liquid coexist. ANEOS, on the other hand, does a good job in such a region.

ANEOS does not have an analytic form as the previous EOS, but consists of about 3000 lines of FORTRAN. Access to it is limited as it is a copyright programme of the Sandia National Laboratory.

2.3.3.6 Theoretical Calculations of Shock Temperatures

From the third Hugoniot equation we obtain E_H-E_0=1/2 (P_H+P_0)(V_0-V_H). Differentiating this with respect to specific volume keeping the temperature constant we get:

$$\frac{dE_H}{dV} = \frac{1}{2}(V_0 - V_H)\frac{dP_H(V)}{dV} - \frac{1}{2}(P_H + P_0) \qquad (2.3.3.29)$$

Suppose, now, that the entropy S is a function of temperature T and specific volume V of the system. Hence:

$$dS = \left(\frac{\partial S}{\partial T}\right)_v dT + \left(\frac{\partial S}{\partial V}\right)_T dV \qquad (2.3.3.30)$$

The specific heat at constant volume C_v is defined as:

$$C_v = T\left(\frac{\partial S}{\partial T}\right)_v \qquad (2.3.3.31)$$

while from Maxwell equations:

$$\left(\frac{\partial S}{\partial V}\right)_T = \left(\frac{\partial P}{\partial T}\right)_v \qquad (2.3.3.32)$$

Combining Equation (2.3.3.8) with (2.3.3.30)-(2.3.3.32) we derive:

$$dS = \frac{C_v dT}{T} + \frac{\gamma(V) C_v dV}{V} \qquad (2.3.3.33a)$$

Considering the first law of thermodynamics, dE=TdS-PdV, Equation (2.3.3.33a) becomes:

$$dE = C_v dT + \frac{\gamma(V) T C_v dV}{V} - PdV \qquad (2.3.3.33b)$$

Finally, combining (2.3.3.29) with (2.3.3.33b) we finally get:

$$\frac{dT_H}{dV} = -\frac{T_H \gamma(V)}{V} + \frac{1}{2C_v}\left[(V_0 - V_H)\frac{dP_H(V)}{dV} + P_H - P_0\right] \qquad (2.3.3.34)$$

and

$$\frac{dS_H}{dV} = \frac{1}{2T_H}\left[(V_0 - V_H)\frac{dP_H(V)}{dV} + P_H - P_0\right] \qquad (2.3.3.35)$$

Thus, if γ and C_v are known at all states on the Hugoniot curve, the temperature and entropy can be calculated on the Hugoniot. $P_H(V)$ is usually taken from shock experiments with data being tabulated. The Gruneisen coefficient can be found either experimentally or using one of the methods described in section 2.3.3.1. Finally, for many solids, an adequate representation of the specific heat can be obtained from one of the simplest forms of the Debye theory. Therefore:

$$C_v = 3nk\left[4D_3(x) - 3x/\left(e^x - 1\right)\right] \qquad (2.3.3.36)$$

where
$$D_3(x) = \frac{3}{x^3}\int_0^x \frac{z^3 dz}{e^z - 1}, \quad x = \frac{\Theta_D}{T}. \qquad (2.3.3.37)$$

and

$$S = 3nk\left[\frac{4}{3}D_3(x) - \ln\left(1 - e^{-x}\right)\right] \qquad (2.3.3.38)$$

where Θ_D is the Debye characteristic temperature of the material.

A new method of calculating shock temperatures and entropy based on the Hugoniot data was recently proposed by K. Nagayama (1994)[21]. He developed a computer code for calculating temperature based on the following assumptions:

- The EOS is Mie-Gruneisen.
- The Gruneisen coefficient follows the relation $\rho\gamma=\rho_0\gamma_0$=constant.
- The heat capacity is given by the Debye model.

- The linear shock-particle velocity relationship holds.

Based on these assumptions, this approach of calculating shock temperature cannot be applied to the pressure regime where electronic contribution gives significant effects to the pressure. However, it provides an accurate estimation of the temperatures at moderate temperatures and the results completely reproduces the published resuslts[22].

This method has been implemented as a subroutine in the program used to calculate residual temperatures in chapter 3. The full code is given in appendix B and the method is fully described in appendix D.

2.3.3.7 Release from High Pressure

The passage of a shock front is an irreversible process resulting in an increase of the internal energy and entropy of the material. A typical diagram of P versus V for shock compression and release is shown in figure 2.2, together with the cold curve (zero-Kelvin isotherm).

The unshocked material is at state V_0, E_0 (we consider the initial pressure to be zero). For a given peak pressure P_H the volume will be V_H, which can be found if P_H (V) is known. The P_H (V) which is the Hugoniot curve can be found either by shock experiments or by combining the EOS and the third Hugoniot equation. However, the Hugoniot curve is *not* the loading path during the shock. It represents the locus of points at different peak pressures. The loading path starts at the initial state A and proceeds along the Rayleigh line R, which represents non-equilibrium states which are passed through very rapidly. Ultimately, point B, corresponding to the peak pressure in the shock wave, is reached. It is important to note that the energy along the loading path R is not constant. The final energy at B is related to the energy in the initial state through the third Hugoniot relation:

$$E_B-E_A=1/2\ P_H(V_0-V_H) \qquad (2.3.3.39)$$

The above equation means that the total energy acquired by a unit mass of the substance, as a result of shock compression, $P_H(V_0-V_H)$ is divided equally between the kinetic energy $u_p^2/2$ and the internal energy E_B-E_A (in a co-ordinate system in which the undisturbed medium is at rest). The change in the internal energy, in turn, is composed of the changes in the cold and thermal energies. This can be seen in Figure 2.2. The total internal energy is given by the area of the triangle V_0BV_H. The lightly shaded area under the 'cold curve' represents the contribution from the zero-Kelvin isotherm, while the more shaded area represents the thermal energy.

However, unloading from state B, by the propagation of rarefaction or release waves from the free surfaces, occurs without any heat conduction because of the short timescales involved and hence follows a path of constant entropy S. When the material is unloaded from the shock state towards the initial one, it is expanded with respect to the initial state at V_f. Since the release is isentropic, that means that the material has acquired an amount of energy which corresponds to the thermal one. Graphically, it is the difference of the two curvilinear triangles ABDA and $V_fAV_oV_f$.

From the second law of thermodynamics dE=TdS-PdV. When dS=0, we obtain:

$$E_f = E_H - \int_{V_H}^{V_f} (PdV)_S \qquad (2.3.3.40)$$

where the subscript H denotes point B along the Hugoniot and P is at constant entropy upon unloading. But E_H is given by the Equation (2.3.2.3). Thus:

$$E_f - E_0 = \frac{1}{2} P_H (V_0 - V_H) - \int_{V_H}^{V_f} (PdV)_S \ . \qquad (2.3.3.41)$$

This energy can then be compared to the energy required to melt or vaporise the material or even thermally excite its electrons.

As it has been mentioned in section 2.3.2, the shocked material has acquired velocity u_p given by the Hugoniot relations. However, an extra term has to be added[23] to this due to the tensile wave. This is:

$$u_R = \int_{V_H(P_H)}^{V(P=0)} \left[-\frac{\partial P}{\partial V} \right]_S^{1/2} dV \ . \qquad (2.3.3.42)$$

Thus, the particle velocity in decompressed material is the vector sum between these velocities, $u_T = u_p + u_R$. So, the velocity magnitude with which the material is actually moving is the difference between the two speeds. The ratio of u_R to u_p is approximately unity for low pressure shocks and it increases with increasing shock strength. Thus, material compressed and accelerated by a shock wave is not later decelerated to rest by the rarefaction; a residual velocity remains. This velocity plays a central role in impact crater excavation. However, the material speed at the free surface is the algebraic sum of these two speeds, $u_{fs} = u_p + u_R$. This sum, is supposed to be the velocity at which material is ejected during impact.

Figure 2.2: Typical P-V Diagram for Shock Compression and Release Adiabat

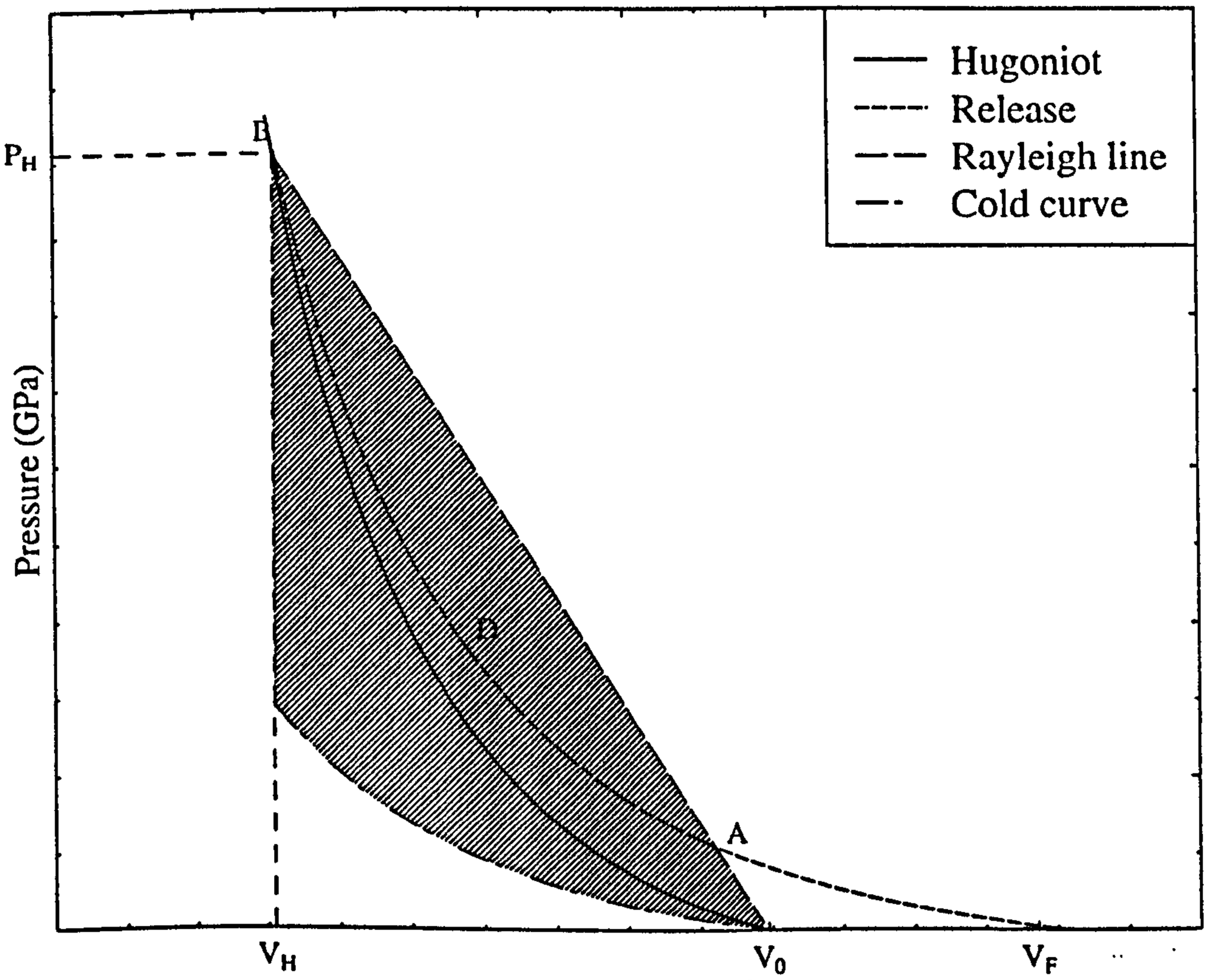

Figure 2.3: Iterative Method for Calculating Release Energies

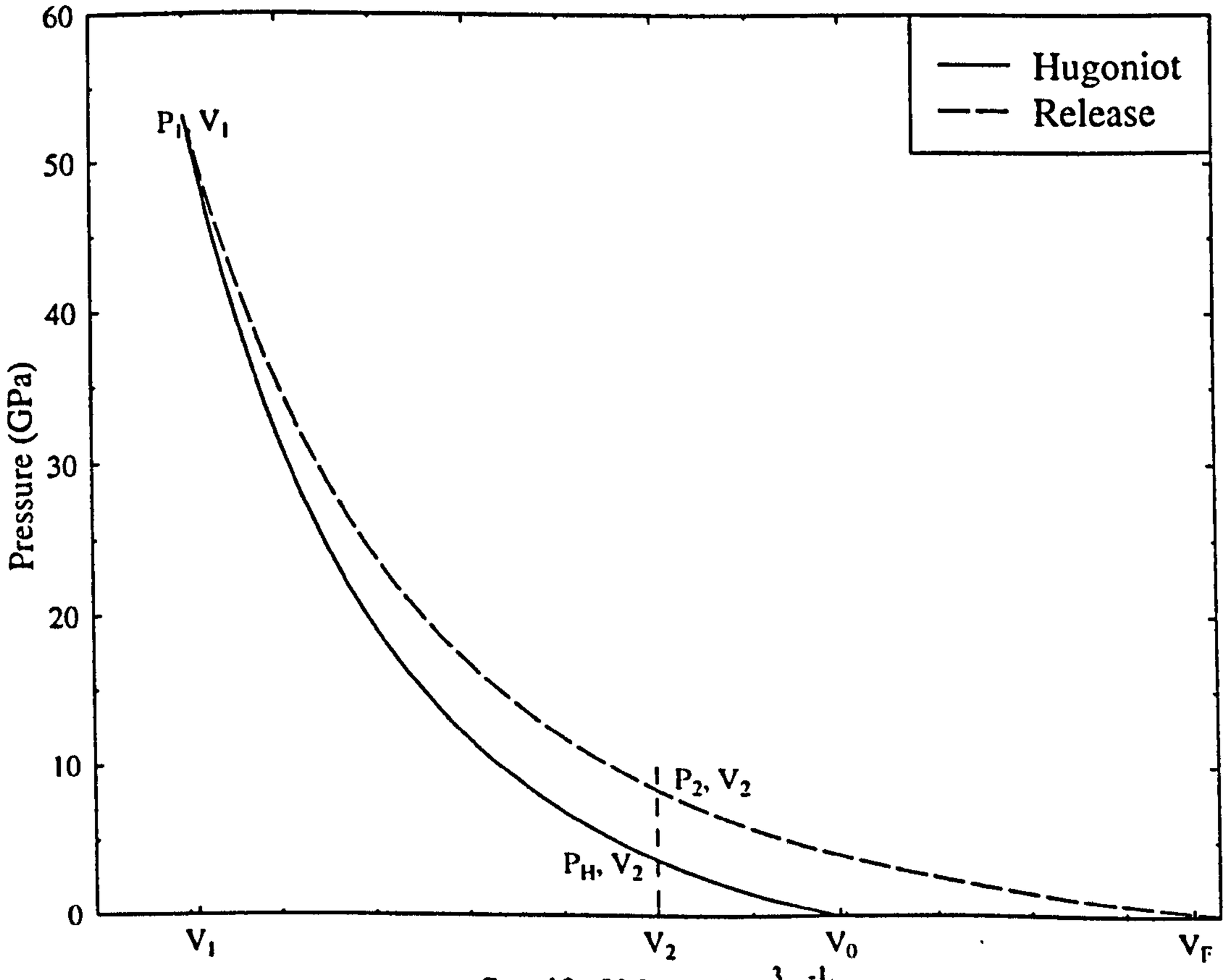

The cause of the difference between u_p and u_R is due to thermodynamics. The shock wave conserves mass, energy, and momentum as it compresses the substance. The rarefaction conserves all the above and entropy as well. Shock compression is thermodynamically irreversible, whereas rarefaction is reversible and adiabatic. Also, any process that contributes to the irreversibility of shock compression also enhances the difference between u_p and u_R . Yielding at the Hugoniot elastic limit, crushing of pore space, or unreversed phase transformations all act to increase the difference between these two speeds.

Finding the pressure variation with the specific volume upon release, would give information about the state of the material after returning to ambient pressures such as residual temperatures and final volume. For this, a knowledge of the EOS is required. Although any EOS can be used, for simplicity reasons, the Mie-Gruneisen EOS is used for this calculation.

Material is shocked from V_0 to P_1, V_1 , as illustrated in Fig. 2.3. Thus, from the third Hugoniot equation:

$$E_1 = \frac{1}{2} P_1 (V_0 - V_1) \qquad (2.3.3.43)$$

Then, it is released through the release adiabat S until P=0. But the pressure at any given point is given by the Mie-Gruneisen EOS. That is:

$$P_i = (P_H)_i + \left(\frac{\gamma(V)}{V}\right)_i \left[E_i - (E_H)_i\right] \qquad (2.3.3.44)$$

with:

$$(E_H)_i = \tfrac{1}{2} (P_H)_i (V_0 - V_i) \qquad (2.3.3.45)$$

From the 2nd law of thermodynamics we have:

$$dE = TdS - PdV \qquad (2.3.3.46a)$$

Using the isentropic constraint dS=0 (entropy conserved during release), Eq. (2.3.3.46a) becomes:

$$dE = - PdV \qquad (2.3.3.46b)$$

A finite difference scheme can be used to march down the release isentrope starting from the Hugoniot impact state (P_1, V_1). The change in volume ΔV is used as the marching step size taken as $(V_0 - V_1) / 10^3$:

$$dE \approx \Delta E = E_i - E_{i-1}$$
$$P \approx \tfrac{1}{2}\left(P_i + P_{i-1}\right) \qquad (2.3.3.47)$$
$$dV \approx \Delta V = V_i - V_{i-1}$$

Substituting Eqs. (2.3.3.47) into Eq. (2.3.3.46b):

$$E_i = E_{i-1} - \frac{\left(P_i + P_{i-1}\right)}{2}\Delta V \qquad (2.3.3.48)$$

Finally, substituting Eq. (2.3.3.48) into Eq. (2.3.3.44) and rearranging:

$$P_i = \frac{\left(P_H\right)_i + \left(\frac{\gamma(V)}{V}\right)_i \left[E_{i-1} - \frac{1}{2}P_{i-1}\Delta V - \left(E_H\right)_i\right]}{1 + \left(\frac{\gamma(V)}{V}\right)_i \frac{\Delta V}{2}} \qquad (2.3.3.49)$$

Successive application of Eqs. (2.3.3.48) and (2.3.3.49) gives the P, V, E loci of these isentropes. The energy under the isentrope is computed by summing the increments:

$\Delta E = \frac{P_i + P_{i-1}}{2}\Delta V$ along the entire path until P_i becomes zero[22,24].

Finally, it is possible to calculate the release temperature of the material, if its shocked temperature is known. If the entropy remains constant (dS=0), from Equation (2.3.3.33a) we derive:

$$\frac{dT}{T} = -\frac{\gamma(V)dV}{V} \qquad (2.3.3.50)$$

From that, it can be deduced that:

$$T_2 = T_1 \exp\left[-\int_{V_1}^{V_2} \frac{\gamma(V)}{V} dV\right] \qquad (2.3.3.51)$$

If V_2 is the release volume at zero pressure then T_2 corresponds to the temperature the material has after it has been released from high pressure and T_1 is the corresponding temperature at the shocked state. Most of the material ejected during a hypervelocity impact cratering process should correspond to this temperature. Equation (2.3.3.51) can be combined with the numerical method of calculating shock temperatures described in section 2.3.3.6 to estimate the residual temperature of a material after a given impact condition.

The iterative process described in this section together with the method to calculate residual temperatures have been implemented in a FORTRAN program as part of this work and is given in appendix B. In this way, starting from a given Hugoniot pressure in a material, which

corresponds to some given impact conditions, is possible to calculate residual temperatures and final volumes and ejecta velocities.

2.4 Constitutive Response

2.4.1 Introduction

In section 2.3.1 the response of an elastic - perfectly plastic material under impact has been reviewed, where the yield strength remained constant. However, this is a case for static loading. In the case of an impact the loading is dynamic and other effects play significant role to the material behaviour. For instance, the material becomes harder as strain and strain rate increases, but the opposite happens when its temperature increases. The first effect is known as work hardening, while the second is known as thermal softening. In the following sections some semi-empirical constitutive equations are presented which are useful for high strain, strain rate and temperature applications and have been used in the hydrocode program of this work and described in ref. 25.

2.4.2 Mohr-Coulomb Strength Model

The Mohr - Coulomb model[25] has been formulated for the behaviour of brittle materials, such as dry soils, rocks, concrete and ceramics. The cohesion and compaction behaviour of such materials result in an increasing resistance to shear up to a limiting value of yield strength as the loading increases. This can be modelled by a piecewise linear variation of yield stress with pressure (illustrated in Figure 2.4) up to a value of Y_{max}. In tension (negative values of pressure), such materials have little tensile strength and this is modelled by dropping the curve Y(p) rapidly to zero as the pressure goes to negative values to give a realistic value for the limiting tensile strength. Note that although the yield stress is pressure dependent the flow rule is volume independent, because of the Equation ($s_1 + s_2 + s_3 = 0$).

2.4.3 Johnson - Cook model

One of most heavily used strength models for metals subjected to large strains, high strain rates and high temperatures in the Johnson - Cook strength model[25,26]. Such behaviour might arise in problems of intense impulsive loading due to high velocity impact and explosive detonation. The model defines the yield stress Y as:

$$Y = [\, A + B\, \varepsilon_p{}^{n} \,]\, [\, 1 + C \log (\varepsilon_p{}^{*}) \,]\, [\, 1 - T_H{}^{m} \,] \qquad (2.4.3.1)$$

where ε_p = effective plastic strain

$\varepsilon_p{}^{*}$ = normalised effective plastic strain rate

T_H = homologous temperature = $(T - T_{room}) / (T_{melt} - T_{room})$

The five material constants are A, B, C, n and m which are found empirically by means of dynamic Hopkinson bar tensile tests over a range of temperatures and Taylor tests (impacting metal cylinders on rigid metal targets which provide strain rates in excess of 10^5 s^{-1}). The expression in the first bracket of Equation (2.4.3.1) gives the stress as a function of strain when $\varepsilon_p{}^{*} = 1.0\ s^{-1}$ and $T_H = 0$ (i.e. for laboratory experiments at room temperature). The constant A is the basic yield stress at low strains (the value Y for an elastic - perfectly plastic material), while B and n represent the effect of strain hardening. The expressions in the second and third sets of brackets represent the effects of strain rate and temperature respectively. In particular, the latter attends to model the thermal softening so that the yield stress drops to zero at the melting temperature T_{melt}.

Figure 2.4: The Yield Stress dependence on Hydrostatic Pressure for the Mohr-Coulomb Model

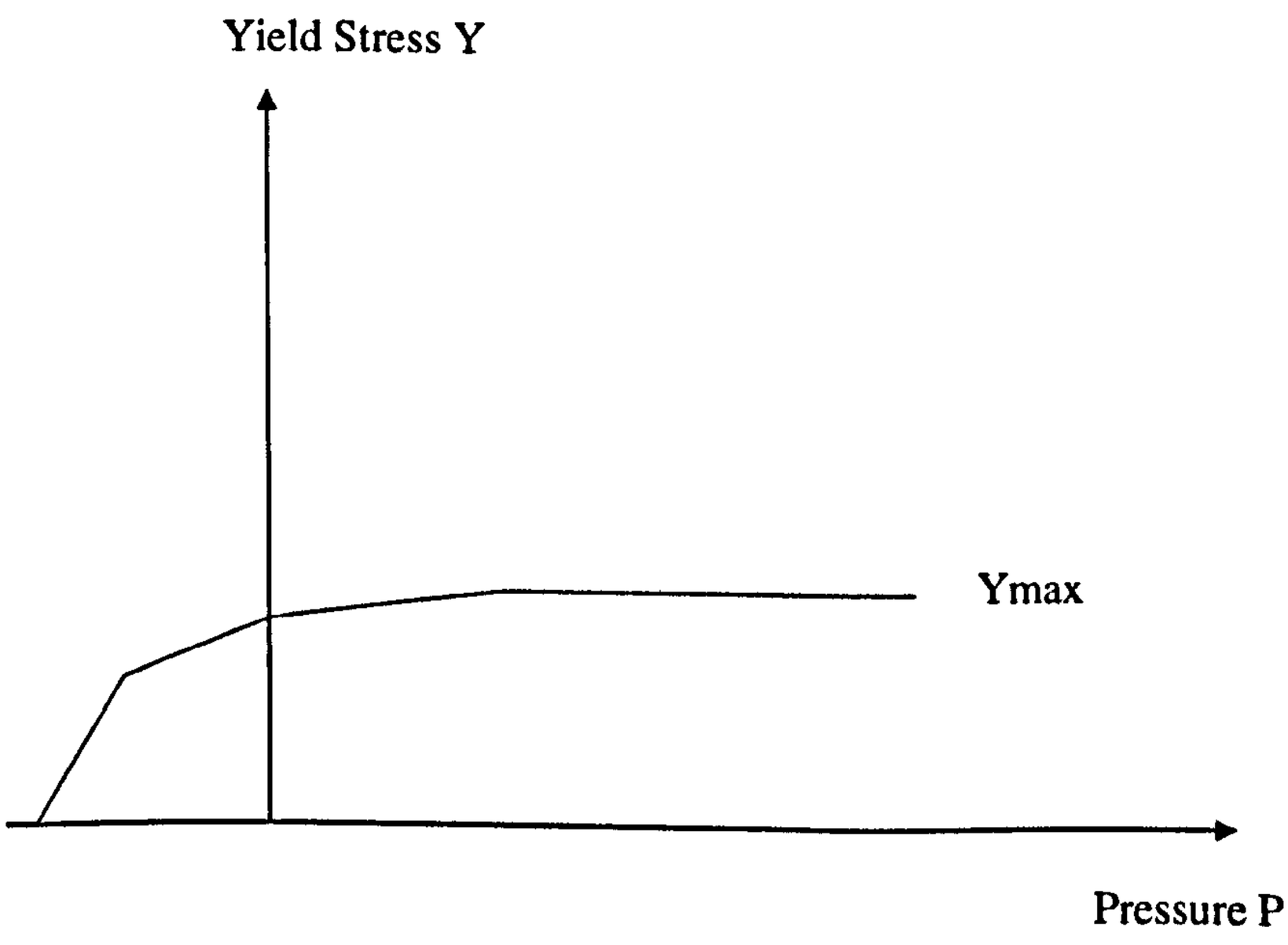

2.4.4 Zerilli - Armstrong model

Although the Johnson-Cook model predicted well the behaviour of many metals in the Taylor tests[25,27], it failed to give accurate predictions for the OFHC (Oxygen Free High Conductivity) copper. For that reason, Zerilli and Armsrong[25,27] suggested a better constitutive model based on dislocation mechanics. The effects of strain/strain rate hardening and thermal softening were included in the formulation. However, they also added the effects of the grain size. The most important point made by them was that each material structure type (fcc, bcc) should have a different constitutive relation, dependent on the dislocation characteristics of the given type. For example, a stronger dependence of the plastic yield stress on temperature and strain rate is known to result for bcc metals as compared with fcc metals. That is why, they coupled the strain hardening term with a temperature and strain rate dependence.

The equations for the yield stress are:

1) For bcc metals:

$$Y = Y_0 + C_1 \exp\left[-C_2 T + C_3 T \log \dot{\varepsilon}\right] + C_4 \varepsilon^n + k d^{-0.5} \qquad (2.4.3.2)$$

and

2) For fcc metals:

$$Y = Y_0 + C_5 \varepsilon \exp\left[-C_2 T + C_3 T \log \dot{\varepsilon}\right] + k d^{-0.5} \qquad (2.4.3.3)$$

where ε = effective plastic strain

$\dot{\varepsilon}$ = normalised effective plastic strain rate

T = temperature (degrees K)

d = grain size.

The material constants are Y_0, C_1, C_2, C_3, C_4, C_5, and n found empirically by Taylor tests.

2.4.5 Steinberg - Guinan model

Experimental data[25,28] on shock - induced free surface velocity versus time using VISAR indicate that at high strain rates (greater than 10^5 s^{-1}) strain rate effects become insignificant compared to other effects. The yield stress reaches a maximum value which is subsequently strain rate independent. The Steinberg - Guinan formulation[28] models this phenomena while allowing the yield stress initially to increase with strain rate. They also postulated that the shear modules increases with increasing pressure and decreases with increasing temperature. They have therefore produced expressions for the shear modulus and yield strength as functions of effective

plastic strain, pressure and internal energy (temperature). The constitutive relations for shear modulus G and yield stress Y for high strain rates are:

$$G = G_0\left\{1+\left(\frac{(\partial G/\partial P)_T}{G_0}\right)\frac{P}{\eta^{1/3}}+\left(\frac{(\partial G/\partial T)_P}{G_0}\right)(T-300)\right\} \qquad (2.4.3.4)$$

$$Y = Y_0\left\{1+\left(\frac{(\partial Y/\partial P)_T}{Y_0}\right)\frac{P}{\eta^{1/3}}+\left(\frac{(\partial G/\partial T)_P}{G_0}\right)(T-300)(1+\beta\varepsilon)^n\right\} \qquad (2.4.3.5)$$

$$\text{subject to } Y_{max} \geq Y_0[1+\beta\varepsilon]^n$$

where η is compression, defined as the initial specific volume V_0 divided by the specific volume V, β and n are the work hardening parameters ε is the effective plastic strain and temperature T is in Kelvin. The subscript 0 refers to the reference state (T=300 K, P=0, ε=0). The partial derivatives are the derivatives of that parameter at the reference state.

2.4.6 Johnson - Holmquist model

The yield stress of brittle materials strongly depends upon impact pressure[29]. This was attempted to be modelled by the Mohr - Coulomb model. However, its simplicity reduces the applicability of the model to a few cases. Lately, Johnson - Holmquist[30] introduced a model which attempts to model brittle effects such as pressure - dependent strength, damage and fracture, significant strength after fracture, bulking and strain rate effects. In this section we give an overall description of the model together with the related equations. Finally, since it is a model designed for hydrocodes and includes a failure model, is the best introduction for the next section and the section describing material modelling into hydrocodes.

The general features of the model are:

- The material begins to soften when damage begins to accumulate (D>0). This allows for gradual softening of the material under increasing plastic strain.
- The strength and pressure are normalised by the strength and pressure components of the Hugoniot Elastic Limit (HEL), which allows for many of the constants to be dimensionless. This can be very helpful when comparing different materials, and when estimating constants for materials which have an insufficient data base to determine constants.
- The strength and damage are analytic functions of the pressure and other variables. This allows for parametric variation of the constants in a more systematic way.
- The equation of state includes the bulking effect.

- The strength is, generally, a smoothly varying functions of the intact strength, fracture strength, strain rate, and damage.

The equations that govern the above material behaviour are

The normalised equivalent (yield) stress is

$$Y^* = Y_i^* - D\left(Y_i^* - Y_f^*\right) \tag{2.4.3.6}$$

were Y_i^* is the normalised intact yield stress, Y_f^* is the normalised fracture stress, and D is the damage $(0 \le D \le 1)$. In addition, the normalised yield stresses (Y^*, Y_i^*, Y_f^*) have the general form

$$Y^* = Y / Y_{HEL} \tag{2.4.3.7}$$

where Y is the actual yield stress and Y_{HEL} is the yield stress at the HEL.

The normalised intact strength is given by

$$Y_i^* = A\left(P^* + T^*\right)^N \left(1 + C \cdot \ln \dot{\varepsilon}^*\right) \tag{2.4.3.8}$$

and the normalised fracture strength is given by

$$Y_f^* = B\left(P^*\right)^M \left(1 + C \cdot \ln \dot{\varepsilon}^*\right) \tag{2.4.3.9}$$

Note that the normalised fracture strength can be limited by $Y_f^* \le$ SFMAX. This optional fracture strength parameter is included to provide more flexibility in defining the important fracture strength.

The material constants are A, B, C, M, N, and SFMAX. The normalised pressure is $P^*=P/P_{HEL}$, where P is the actual pressure and P_{HEL} is the pressure at the HEL. The normalised maximum tensile hydrostatic pressure is $T^*=T/P_{HEL}$, where T is the maximum tensile hydrostatic pressure the materials can withstand. The dimensionless strain rate is $\dot{\varepsilon}^* = \dot{\varepsilon} / \dot{\varepsilon}_0$, where $\dot{\varepsilon}$ is the actual strain rate and $\dot{\varepsilon}_0 = 1.0 \sec^{-1}$ is the reference strain rate. The damage for fracture is accumulated as following:

$$D = \left(\Delta\varepsilon^p / \varepsilon_f^p\right), \tag{2.4.3.10}$$

where $\Delta\varepsilon^p$ is the plastic strain during a cycle of integration and $\varepsilon_f^p = f(P)$ is the plastic strain to fracture under a constant pressure P. The specific expression is:

$$\varepsilon_f^p = D_1(P^*+T^*)^{D2} \tag{2.4.3.11}$$

where D_1 and D_2 are constants. Again the material cannot undergo any plastic strain at $P^* = -T^*$; but ε_f^p increases as P^* increases.

In addition, the hydrostatic pressure before fracture begins (i.e. when D=0) is simply:

$$P = K1 \cdot \mu + K2 \cdot \mu^2 + K3 \cdot \mu^3 \qquad (2.4.3.12)$$

where K1, K2, and K3 are constants (K1 is the bulk modulus); and $\mu=\rho/\rho_0 -1$ for current density ρ and initial density ρ_0. For negative pressure ($\mu<0$), Equation (2.4.3.12) is replaced by $P=K1 \cdot \mu$. Energy effects are assumed to be insignificant; that is, if we assume, a Mie-Gruneisen EOS then the Gruneisen coefficient is zero.

However, after damage begins to accumulate (D>0), bulking can occur. This is a well know effect on some brittle materials where pressure and/or volumetric strain increases as damage accumulates. Now, an additional incremental pressure ΔP is added to (2.4.3.12) such that:

$$P = K1 \cdot \mu + K2 \cdot \mu^2 + K3 \cdot \mu^3 + \Delta P. \qquad (2.4.3.13)$$

The pressure increment is determined from energy considerations; it varies from $\Delta P=0$ at D=0 to $\Delta P=\Delta P_{MAX}$ at D=1.0. The incremental internal elastic energy decrease (due to decreased shear and deviatoric stresses) in converted to potential energy by incrementally increasing ΔP. The decrease in the shear and deviatoric stresses occurs because the strength Y decreases as the damage D increases.

2.5 Computer Codes for Impact Simulations - Hydrocodes

An impact process is a very complicated phenomenon lasting a few microseconds. Controlled and potentially expensive experiments are often needed for understanding the processes involved in such impacts. In addition, experiments are limited by the impact velocity and size. Hence, events such as planetary impacts are impossible to study in a laboratory. That is why such events are simulated using numerical techniques with codes, often called hydrocodes (the first codes treated the material as a fluid, hydrodynamically, that is why the codes referred to as hydrocodes). Such codes make it relatively easy to calculate the behaviour of materials upon impact events such as impacts on planets or spacecraft structures for engineering purposes.

Although many such hydrocodes exist, the general features and problems are the same. The basic equations that are used in hydrocodes include:

1. Conservation equations (mass, momentum, energy)
2. Constitutive relations (volumetric and deviatoric response)
3. Failure criteria (instantaneous, micromechanical, time-dependent)

Excellent reviews exist about the subject such as McGlaun and Yarrington(1993)[23], Zukas(1990)[31], and Anderson(1987)[32]. In the following sections a brief description on hydrocodes is given the based on the treatment by Anderson[32].

2.5.1 Conservation Equations

From classical continuum mechanics a set of differential equations can be established through the application of the principles of conservation of mass, momentum and energy from a macroscopic point of view;

- Conservation of mass:

$$\dot{\rho} + \rho \dot{u}_{i,i} = 0 \tag{2.5.1}$$

- Conservation of linear momentum:

$$\rho \ddot{u}_i = \sigma_{ji,j} + \rho f_i \tag{2.5.2}$$

- Conservation of angular momentum:

a) Polar media: $$\rho \dot{L}_i = \rho Q_i + R_{ji,j} + \varepsilon_{jkl}\sigma_{jk} \tag{2.5.3a}$$

b) Nonpolar media: $$\sigma_{ij}=\sigma_{ji} \tag{2.5.3b}$$

- Conservation of energy:

$$\rho \dot{E} = \left(\sigma_{ji}\dot{u}_i\right)_{,j} - q_{i,i} + \rho S + \rho \dot{u}_i f_i \tag{2.5.4a}$$

$$E = I + \frac{1}{2}\dot{u}_j \dot{u}_j \tag{2.5.4b}$$

- Equation of state and flow rule.

However, there are two different ways to describe the above relations; Langrangian and Eulerian. The Eulerian description is a spatial description, while the Langrangian is a material one. The differences are discussed in more detail below. Solution of the above equations first requires that the differential equations be made discrete. A lattice of points, or grid, is generated to approximate the geometry of interest. If adjacent points are connected by lines, the area or volume enclosed by connecting adjacent point in the grid is referred to as cells.

To obtain an Eulerian or spatial description, one should compute, as time progresses, velocity, pressure, density, temperature, etc., at the fixed points on the grid. All grid points, and consequently cell boundaries, remain spatially fixed with time. Mass, momentum, and energy flow across cell boundaries. The quantities of flow into and out of a cell are used to compute the

new mass, pressure, velocity, energy, etc., of that cell. In this formulation, the cell volume is, obviously, invariant since points remain fixed in space.

In the Langrangian description, however, the grid points are attached to the material and move with the local material velocity. Velocity, pressure, density, temperature etc., are computed as time progresses for each cell. Adjacent points can be stretched or come closer together, as a spring, depending upon the forces applied. Mass, momentum, and energy are transported by material flow; the grid points move relative to a fixed spatial co-ordinate system. This means that the grid points follow particle paths of points in the material. In this approach, mass within the cell is invariant, but the volume of the cell may change with time because of expansion or compression of the material.

Let us, consider the example of density calculation. In calculating the density of a cell, $\rho=M/V$, where M is the mass within the cell of specific volume V, the Eulerian approach has a constant volume, V, and the mass changes as more or less mass accumulates in the cell due to mass flow across the boundaries of the cell. The density would decrease if more mass flowed out of a cell during a time step, Δt, than flowed into the cell. In the Langrangian description, however, the mass M is constant, and the volume of the cell changes due to the movement of the boundaries firmly attached to the moving material. The density would increase as the cell is compressed.

The biggest advantage of the Langrangian description is its ability to follow the history of a material particle across the impact duration. A material whose properties depend upon the previous history can be modelled. Thus, this approach allows an excellent treatment of material models (constitutive relations) and failure models, e.g. spallation and fragmentation.

However, Langrangian codes can have severe difficulties where large distortions occur, such as turbulent flow and high velocity impacts. In the Langrangian grid, the mesh points follow the motion of particles of mass. For instance, in an impact problem, the computational mesh becomes severely distorted near the projectile/target interface.

The problems which can be encountered in Langrangian calculations because of compression or severe distortion of the grid do not exist in the Eulerian approach because of its fixed grid system. In principle, all hydrodynamic problems could be solved numerically by using a multi-material Eulerian calculation which computes the mass, momentum, and energy flows across the fixed cell boundaries. Turbulent flow, rotational flow, high velocity impacts, highly compressed states, etc., can be computed using an Eulerian computer code.

However, because the Eulerian approach describes only what is crossing grid boundaries (thus, the instantaneous state of the material in the zone), the position of lines which approximate material interfaces and exterior boundaries is difficult to determine. Therefore, it cannot compute the time history of a particular material particle, which can be important in formulating realistic constitutive, fracture, and failure relations.

2.5.1.1 Space Discretisation and Criteria for Discretisation

Although Equations (2.5.1-2.5.4) describe the continuum, the computer is finite. Somehow the problem must be discretised in order to solve the differential equations. Two methods for solving continuum problems on the computer are used; finite difference and finite element.

In the finite difference representation, a lattice of points, or grid, is generated to approximate the geometry of interest. The spatial derivatives in the differential equations are replaced by difference equations, e.g., for some functional F, the partial derivative $\partial F/\partial x$ becomes $\Delta F/\Delta x$ where the differences are computed from values at grid points. The finite difference scheme is a pointwise approximation. The values computed at a point are then taken to represent the physical parameter over some finite region of space, e.g., a grid cell. The finite difference may be thought of as an approximate solution technique to an exact problem. This is because in the usual approach one manipulates the governing physical relationships into differential form. Then derivatives are systematically replaced with analogous difference operators. This is done for the governing equations, boundary and initial conditions. This procedure is then results in a set of algebraic equations which can then be solved numerically.

Whereas, the finite difference technique is a pointwise discretisation of the continuum, finite element techniques envision the solution region as being composed of many small interconnected sub-regions or elements. Thus, a piecewise approximation of the differential equations is made. Nodes are assigned to elements and then an interpolating function, typically a polynomial, is used to represent the variation of the variable over the element. In this technique, the discretisation is introduced at the outset. There is no playing with differential equations and replacement of derivatives. The continuum with its infinite degrees of freedom is replaced at the outset by a substitute finite degree of freedom system whose characteristics approximate those of theoretical modes. Once this approximation is made, the resulting equations are solved exactly.

However, for both schemes, there are four criteria which should be satisfied: consistency, accuracy, stability and efficiency.

2.5.1.2 Consistency

The first property to be demanded is that each scheme in some manner approximate the differential equations they are replacing. For instance, in the finite difference technique, it is required that the difference scheme reduce to the differential equation in the limit, that is

$$\lim_{\Delta x \to 0}\left(\frac{\Delta F}{\Delta x}\right) = \frac{\partial F}{\partial x} \tag{2.5.5}$$

This requirement is fundamental, otherwise the difference scheme does not simulate the differential equation.

However, the use of finite spatial and time steps produces errors and causes the solution to deviate from the solution to the differential equation.

2.5.1.3 Accuracy

Two types of errors may occur which impair the accuracy of a scheme; round-off errors and truncation errors. Round-off errors are associated with the precision of the computer, that is, the number of significant digits carried by the computer to represent a variable. Even with the large number of computer digits, occasions do arise where round-off errors create difficulties. Sometimes, special algorithms are necessary to handle certain types of such errors.

The second type of error is the result of the approximation scheme used, and is called truncation error. For example, in the finite difference scheme, the essence of this error arises from representing a continuous variable with a discrete number of points, and the magnitude of the errors depend on the mesh intervals in time and space.

2.5.1.4 Stability

Unfortunately, answering the question of accuracy is not efficient. If a scheme produces a solution which is not bounded, the scheme is said to be numerically unstable. A numerical method is stable if a small error at any stage produces a smaller cumulative error. If an error is amplified from time step to time step, the error will quickly swamp the solution and the result will be meaningless. For instance, assume that an error ε exists in a parameter Π at time step τ. The calculation of the Π at time step $(\tau+1)$ will have an error associated with it, and both $\Pi^{\tau+1}$ and $\varepsilon^{\tau+1}$ will be functions of Π and ε at the previous time steps:

$$\Pi_n^{\tau+1} + \varepsilon_n^{\tau+1} = f\left(\Pi_n^{\tau} + \varepsilon_n^{\tau}\right) \tag{2.5.6}$$

The amplification of the error at time step $(\tau+1)$ is given by:

$$\varepsilon^{\tau+1} = \gamma\,\varepsilon^{\tau} \tag{2.5.7}$$

where γ is the amplification factor. This amplification factor is related to truncation errors and the integration schemes used, but is not associated with round-off errors. For stability, the requirement is that the error at time $(\tau+1)$ be less than or equal to the error at time τ, otherwise the error will grow as time increases. This leads to the very important conclusion: the absolute magnitude of the amplification factor must be less or equal to one for a numerical scheme to be stable:

$$|\gamma| \leq 1 \tag{2.5.8}$$

The errors in Equation (2.5.6) also satisfy the general partial differential equations. Separation of variables is used to separate the time component of ε from the spatial component:

$$\varepsilon = \varepsilon^*(t)e^{ikx} \tag{2.5.9}$$

where $\varepsilon^*(t)$ gives the amplitude of the Fourier mode. As any waveform can be approximated by the superposition of the various wavelengths in a Fourier series, then the procedure is to demand stability for an arbitrary wavelength, represented by the wavenumber k It can be proved[32] that the stability criterion (2.5.8) leads to:

$$\Delta t \leq \frac{\Delta x}{c} \tag{2.5.10a}$$

for Langrangian co-ordinates. For Eulerian co-ordinates, the above equation takes the form:

$$\Delta t \leq \frac{\Delta x}{|v|+c} \tag{2.5.10b}$$

where c is the sound speed and v is the particle velocity.

Thus, the stability criterion is, essentially, a statement of causality, i.e., no signal (information) can be allowed to propagate across the shortest dimension of a zone in a time Δt.

2.5.1.5 Efficiency

The final requirement for a numerical technique is efficiency. A computer is finite; only a certain amount of memory is available and the calculation time required to get a numerical solution must be reasonable. Most of the times, the cost of running a given simulation is related to central processing time, memory requirements, and input/output operations. Efficiency decreases with greater complexity of the numerical technique (e.g. finer grid); however, the accuracy of the result is generally increased with increasing complexity. Thus, a compromise must be reached between efficiency and accuracy.

2.5.2 Material Modelling in Hydrocodes

Material modelling can be divided into three areas: volumetric response, or resistance to compressibility (Equation of State), the resistance to distortion (constitutive) and the reduction in ability to carry stress as damage accumulates (failure). However, in sections 2.3 and 2.4 an extensive review about material behaviour was given. Material modelling in hydrocodes follow the same analysis.

2.6 Conclusions

In this chapter, an overview of the basic principles and characteristics of material behaviour under impact and dynamic loading and hydrocode modelling was presented. Especially, the Mie-Gruneisen EOS was reviewed together with ways of calculating temperatures and ejecta velocities from first principles. For that reason, a simple computer program has been constructed (appendix B) which calculates temperatures and velocities upon release based on some basic principles such as the Debye theory of solids, thermodynamics and Hugoniot relations. This program is going to be used in both chapters 3 and 4.

Different constitutive models were also presented which will be used in chapter 5 for modelling of different materials in hydrocode simulations of metals impacting soda-lime glass.

References

1. Gault DE et al., (1968), 'Impact Cratering Mechanics and Structures' in French BM and Short NM (Eds.), *Shock Metamorphism of Natural Materials,* Mono Book Co., Baltimore, Md.
2. Melosh HJ, (1989), *'Impact Cratering: A Geologic Process'*, Oxford University Press, N.Y.
3. Nolan MC et al., (1996), *Icarus,* **124**, pp 359.
4. Von Mises R, (1928), Angew R, *Math. U. Mech.*, **8**, [English Translation: UCRL Trans. 872].
5. Asay JR and Kerley GI, (1987), *Int. J. Impact Engng*, **5**, pp 69.
6. Sikka BK et al., (1983), *Physics Reports*, **102(3)**, pp 121.
7. Hama J and Suito K, (1996), *J. Phys.: Condens. Matter*, **8**, pp 67.
8. Gruneisen E, (1926), in Greiger H and Scheel K. (Eds.), *Handbook der Physic*, **10**, Springer, Berlin (in German).
9. Zel'dovish YB and Raiser YP, (1967), *'Physics of Shock Waves and High Temperature Phenomena'*, **2**, Academic Press, N.Y.
10. Slater JC, (1939), *'Introduction to Chemical Physics'*, McGraw-Hill.
11. Dugdale JS and MacDonald DKC, (1953), *Physics Reports*, **89**, pp 832.

12.Vaschenko VY and Zubarev VN, (1963), *Sov. Phys. Solid State*, **3**, pp 653.

13.Migaut A, (1971), *J. Phys.*, **32**, pp 437.

14.Migaut A, (1972), *J. Phys.*, **33**, pp 701.

15.Romain J et al., (1979), in Timmerhaus KB and Barber MS (Eds.), '*High Pressure Science and Technology*, **1**, Plenum, N.Y.

16.Bennett BI et al., (1978), Los Alamos Scientific Laboratory Report, LA-7130.

17.Ross M, (1989), *J. Chem. Phys*, **73**, pp 4445.

18.Royce E., (1971), Lawrence Livermore Laboratory Report, UCRL 51121.

19.Nagayama K and Mori Y, (1994), *J. Phys. Soc. Japan*, **63(11)**, pp 4070.

20.Tillotson JH, (1962), Gen. Atomic. Rep., AG 3612.

21.Nagayama K (1994), *J. Phys. Soc. Japan*, **63**, pp 3737.

22.McQueen RG et al., (1970), in Kinslow R (Ed.), '*High Velocity Impact Phenomena*', Academic Press, N.Y.

23.Asay JR and Shahinpoor M (Eds.), (1993), '*High Pressure Shock Compression of Solids*', Springer-Verlag, N.Y.

24.Anderson CE Jr, et al., (1990), *Int. J. Impact Engng*, **9**, pp 89.

25.AUTODYN™ Theory Manual (Century Dynamics Inc., Oakland, CA, 1995)

26.Johnson GR and Cook WH, (1983), *Proc. 7th Int. Symp. On Ballistics*, Hague, Netherlands.

27.Zerilli FJ and Armstrong RW, (1987), *J. Appl. Phys.*, **61(5)**, pp 1816.

28.Steiberg DJ et al., (1979), *J. Appl. Phys.*, **51(3)**, pp 1498.

29.Rosenberg Z, (1985), *J. Appl. Phys*, **58**, pp 5087.

30.Holmquist TJ, et al., (1995), *Proc. 15th Int. Symp. On Ballistics*, Jerusalem, Israel.

31.Zukas JA (Eds.), (1990), *'High Velocity Impact Dynamics'*, John Willey, N.Y.

32. Anderson CE Jr, (1987), *Int. J. Impact Engng*, **5**, pp 33.

CHAPTER 3

Theoretical Calculation of Ejecta Temperatures and Velocities

3.1 Introduction

The main area of this thesis is to calculate the temperature of the ejecta resulted from a Hypervelocity Impact. As it has been mentioned in the introduction, the approach is 3-fold, constituted of theoretical, experimental and simulation techniques. In this chapter, we shall explain how to find temperatures, theoretically, using the laws of thermodynamics and the Hugoniot relations. The approach is similar to the one followed by Anderson et al. (1990)[1] to calculate the residual temperatures of the debris cloud produced by hypervelocity impacts of Aluminium on Aluminium, Cadmium on Cadmium, Molybdenum on Molybdenum and Lead on Lead.

We reproduce his results and then calculate residual temperatures for Iron impacting Gold and Copper in order to compare them with existing experimental data. However, since glass is our main target material of study, we then present calculations of glass ejecta temperatures when impacted by Iron. We have chosen to perform the calculations with Iron because experiments were performed in the Van de Graaff accelerator facility using Iron (see chapter 4).

Furthermore, velocity thresholds for impact plasma production have also been calculated and presented in this chapter for calibration purposes of the Cosmic Dust Analyser (CDA) which will fly on the Cassini/Huygens mission [2] (which will encounter particles in interplanetary space and co-orbiting in the Saturnian system).

In addition, we shall show how the above approach of calculating residual temperatures may be used to find the ejecta velocities of the target under Hypervelocity Impact. This has immediate applications to geology and solar system sciences. It has been suggested in the past that the terrestrial planets accumulated from previously condensed solid objects (O' Keefe and Ahrens (1977)[3] , Rinwood (1975)[4]) and that the moon itself may be an accumulation of impact ejecta from a primordial mantle of the earth (Cameron and Ward (1976)[5]). The origin of asteroids and asteroidal families could be closely related to the impact disruption of the parent bodies and to the ejection of the fragments away from the gravitational field of the planet.

Finally, the two Voyager missions have shown that water ice is abundant in the outer solar system and in particular several of the satellites of the gaseous planets are covered with ice. Impact cratering on these icy surfaces will produce ejecta, which if travelling fast enough can escape the parent body. This idea has been put forward as a contributor to the origin of the rings of Saturn, Jupiter and Neptune.

Thus, it becomes apparent that calculating ejecta velocities is crucial in the understanding of our solar system. At the end of this chapter we also present simple theoretical calculations of ejecta velocities of water ice (where no strength was considered) and compare them against published data.

3.2 Theoretical calculation of ejecta temperatures and velocities

From the 1st law of thermodynamics, the change in internal energy of a system is given by:

$$dE = TdS - PdV \tag{3.1.1}$$

where T is the temperature, S is the entropy, P is the hydrostatic pressure and V is the specific volume. If the entropy S is a function of temperature and pressure, i.e. S = S(T, P) then the change in entropy is given by:

$$TdS = T\left(\frac{\partial S}{\partial T}\right)_P dT + T\left(\frac{\partial S}{\partial P}\right)_T dP \tag{3.1.2}$$

However, the specific heat at constant pressure C_P is given by:

$$C_P = T\left(\frac{\partial S}{\partial T}\right)_P \tag{3.1.3}$$

In addition, from the 1st Maxwell equation of thermodynamics [6] we have that:

$$\left(\frac{\partial S}{\partial P}\right)_T = -\left(\frac{\partial V}{\partial T}\right)_P \tag{3.1.4}$$

The coefficient of volumetric expansion β is defined as:

$$\beta = \frac{1}{V}\left(\frac{\partial V}{\partial T}\right)_P \tag{3.1.5}$$

Therefore, using Equations (3.1.2) - (3.1.5), Equation (3.1.1) takes the following form:

$$dE = C_p dT - \frac{T\beta}{\rho} dP - PdV \tag{3.1.6a}$$

or approximating

$$\Delta E = C_p \Delta T - \frac{T\beta}{\rho} \Delta P - P\Delta V + n \tag{3.1.6b}$$

where n is the specific energy required for a phase transformation. We will compute the temperature when the material has returned to the ambient pressure. As the final state is at the same pressure as the initial state, the second term on the right-hand side of Equation (3.1.6b) is zero. In addition, if we suppose that the ambient pressure is zero (not an illogical assumption since hypervelocity impact experiments are performed in vacuum), then the third term vanishes as well. If we, further, assume that the specific heat remains constant, then Equation (3.1.6b) may reduce to:

$$\Delta E = C_p (T - T_0) + n \tag{3.1.7}$$

where T_0 is the initial temperature (usually about 300 K). Rearranging the above equation we find that:

$$T = \frac{\Delta E - n}{C_p} + T_0 \tag{3.1.8a}$$

if phase transitions exist. Otherwise Equation (3.1.7) reduces to:

$$T = \frac{\Delta E}{C_p} + T_0 \tag{3.1.8b}$$

However, what is ΔE? It is, simply, the change in internal energy of the initial state (before the impact) and the final state (after the material has been released):

$$\Delta E = E_f - E_0 = \frac{1}{2} P_H (V_0 - V_H) - \int_{V_H}^{V_f} (PdV)_S \tag{3.1.9}$$

As it has been already explained in section 2.3.3.6, it is possible to calculate E_f-E_0 using an iterative process and thus implement it in a computer code. Therefore, starting from a given Hugoniot state of a material, it is possible to calculate the residual temperature.

But, we are interested in what is the residual temperature of the material with respect to the impact velocity, since we are able to measure it directly from the experiments. Hence, it is essential to calculate the Hugoniot pressure for each impact. The way to do it is by the impedance match method [7,8] , understanding that this is only an approximation to the problem. The projectile is supposed to be an infinite sheet with thickness equal to the actual projectile diameter. The target is approximated by a half space. The sheet, which extends laterally to infinity, slaps vertically to the target at the impact velocity U_0. Thus, the impact problem, which, in general, is 3-dimensional, is reduced to an 1-dimensional approximation. This approximation, however, neglects the release waves inward from the sides of the actual projectile and so tends to overestimate the actual mean pressure. Release waves become significant when the shock wave in the target has travelled about one projectile diameter.

Immediately after the first contact, two shocks propagate away from the impact interface, one inside the projectile and the other into the target. Between the shocks, the target and projectile are both raised to the same pressure and the material particle velocity must be the same, since neither interpenetration nor separation can occur. However, other properties, such as the compressed densities of the projectile and target, their internal specific energies, and the velocities of the shock waves may vary for the two materials.

The conditions between the shocks are determined by the Hugoniot equations (Equations 2.3.2.1-2.3.2.3) to each shock separately, using the appropriate Equation of State for each material and imposing the equality of pressure and particle velocity at the interface. Care must be taken to apply the Hugoniot equations to the projectile in a co-ordinate frame in which it is at rest, since the Hugoniot equations have been derived under the assumption that the unshocked material is at rest. The unshocked projectile material is moving at U_0 in the target rest frame, so that if u_p is the particle velocity behind the shock in the projectile frame of reference, then the same material moves at speed (U_0 - u_p) from the target point of view. The equality of particle velocity in both projectile and target, thus, requires

$$u_t = U_0 - u_p \tag{3.1.10}$$

where u_t is the target particle velocity.

From the second Hugoniot equation, Equation (2.3.2.2) we have an expression between the Hugoniot pressure, shock velocity and particle velocity behind the shock

$$P_H=\rho_0 u_s u_p \tag{3.1.11}$$

In addition, we have, already, established the fact that there is an empirical relation between shock velocity and particle velocity (Equations 2.3.2.4 and 2.3.2.5). Bearing in mind that the pressure in the interface of the target and projectile must be the same, it is possible to derive the following equations

$$u_t^2\left(\rho_{0_p} s_p - \rho_{0_t} s_t\right) - u_t\left(\rho_{0_p} c_{0_p} + 2\rho_{0_p} s_p U_0 + \rho_{0_t} c_{0_t}\right) + \rho_{0_p} U_0\left(c_{0_p} + s_p U_0\right) = 0 \tag{3.1.12a}$$

and

$$-\rho_{0_p} b_p u_t^3 + \left(\rho_{0_p} s_p + 3\rho_{0_p} b_p U_0 - \rho_{0_t} s_t\right)u_t^2 - \left(\rho_{0_p} c_{0_p} + 2\rho_{0_p} s_p U_0 + 3\rho_{0_p} b_p U_0^2 + \rho_{0_t} c_{0_t}\right)u_t +$$

$$\rho_{0_p} U_0\left(c_{0_p} + s_p U_0 + b_p U_0^2\right) = 0 \tag{3.1.12b}$$

Equation (3.1.12a) holds when in both target and projectile a linear relation exists between shock velocity and particle velocity, that is

$$U_{s_t} = c_{0_t} + s_t u_t \text{ and } U_{s_p} = c_{0_p} + s_p u_p,$$

while Equation (3.1.12b) holds when a linear relation in the target exists between shock velocity and particle velocity, but a relation of the form

$$U_{s_p} = c_{0_p} + s_p u_p + b_p u_p^2$$

exists in the projectile. This is used for the iron projectiles in sections 3.4 and 3.5.

Therefore, by solving the appropriate equation, it is possible, firstly to find the particle velocity inside the target and then the common shock pressure. After that, the computer program may be used to find the corresponding ΔE. However, although, until now, it is possible to calculate ΔE, we must decide which of the Equation (3.1.8) to use in order to find the residual temperature. As it has been already mentioned, n is the latent heat for a phase transformation. Thus, Equation (3.1.8b) will hold up to incipient melting, whereas Equation (3.1.8a) will hold after that point and in particular from complete melt up to incipient vaporisation n correspond to the specific heat of fusion, since only melting takes place up to incipient vaporisation. Therefore, we are able to find the changes in internal energy for incipient/complete melting/vaporisation if the temperatures of melting/vaporisation and the heats of fusion and vaporisation are known. That means that the values of ΔE are known, and hence we can find the shock pressure by using the same computer program; and since the pressure has been calculated, it is possible to use Equation (2.3.2.9) to find the impact velocity which will produce the required phase change. Hence we know the regions where Equations (3.1.8) hold.

Let us now summarise the steps required to find the residual temperatures

1. Calculate the change in energy for a phase change in the target
   - Incipient melt: $\Delta E_{im}=C_p(T_m-T_0)$
   - Complete melt: $\Delta E_{cm}=C_p(T_m-T_0)+ n_f$
   - Incipient vaporisation: $\Delta E_{iv}=C_p(T_v-T_0) + n_f$
   - Complete vaporisation $\Delta E_{cv}= C_p(T_v-T_0) + n_f + n_v$

   where n_f and n_v are the enthalpies of fusion and vaporisation respectively.
2. Find the Hugoniot volume and pressure to produce the above ΔE for the target using the program.
3. Find the specific volumes of the projectile that correspond to the shock pressure found above.
4. Use Equation (2.3.2.9), that is, $U_0 = \left[1+\left(\frac{V_0^t - V_H^t}{V_0^p - V_H^p}\right)^{1/2}\right] * \sqrt{P\left(V_0^p - V_H^p\right)}$ to find the impact velocity required for a phase change.
5. Find the target particle velocity and thus the shock pressure for some impact velocities, solving either Equation (3.1.12a) or Equation (3.1.12b).
6. Using the computer program calculate the change in internal energy produced by the given shock pressure.
7. Finally, using the calculated ΔEs, we find the residual temperatures using Equations (3.1.8).
8. From steps 1-4, the way to calculate velocity thresholds for impact plasma production becomes apparent. We are interested in the minimum impact velocity required which is sufficient to vaporise the target material (where we assume that ionisation naturally occurs through collisions within the vapour[9] .Thus, the change in energy is given by $\Delta E_{iv}=C_p(T_v-T_0)+n_f$ and hence the shock pressure and impact velocity can be found.

Finally, in section (2.3.3.6) when we discussed release from high pressure, we mentioned that after release, the materials acquires an extra term to its velocity, given by Equation (2.3.3.42)

$$U_R = \int_{V_H}^{V} \left(-\frac{\partial P}{\partial V}\right)_S^{1/2} dV. \qquad (3.1.13)$$

We can use the same difference approach as in section (2.3.3.6) to deduce an approximate relation for U_R. Thus Equation (3.1.7) becomes

$$U_R = \sum_{V_H}^{V_f} -(\Delta P \cdot \Delta V)^{1/2} \qquad (3.1.14)$$

Thus, by summing the increments $(\Delta P \cdot \Delta V)^{1/2}$ (in the same computer program mentioned earlier) along the release isentrope, is possible to calculate the extra term added to U_p. Therefore, the sum of U_p+U_R gives the ejection velocity of the target material.

However, this is only an approximation based on the following assumptions:

- The release path is considered to be an isentrope.
- This is a 1-D calculation, where we have considered that all the ejected material has the same velocity. That is, it has been subjected to the same shock pressure. However, this is not a case in a 3-D impact. Ejected material has been shocked to different pressures. However, what it is calculated is an estimation of the maximum ejecta velocity. If the values of the different pressures that the target has been subjected to we known, then the different ejecta speeds could be calculated.
- Stress pulses are viewed as sharp-fronted waves with negligible rise time. However, if this is the case, then at the free surface (where, by definition, the pressure vanishes at all times) the pressure jumps discontinuously from zero at the free surface to its maximum value just beneath. This sharp-fronted wave, however, is merely a convenient approximation to a wave with a small, but finite rise time. For further information about stress wave interference in the near-surface zone, one can refer to Reference (9).
- Finally, although, the above treatment can be used with any Equation of State, for simplicity reasons, the Mie-Gruneisen EOS has been used. Thus, we limit ourselves to the incipient vaporisation point, since as mentioned is section 2.3.3.1 this EOS gives poor results in the vapour region.
- Release wave interactions leading to spallation we re not considered.

3.3 Impacts of Al-Al, Cd-Cd, Mo-Mo and Pb-Pb

In this section results published in Reference (1) are reproduced in order to show they are consistent with the treatment explained in the previous section. However, the Mie-Gruneisen EOS has been used instead of the Tillotson EOS which has been used in Reference (1). The material constants used in this treatment are shown in table 3.1. The Hugoniot parameters and

Gruneisen coefficients come from Reference (8), while thermodynamic properties are from Reference (33).

Using the table 3.1, it is possible to calculate the specific energy required for incipient / complete melting and incipient vaporisation of the materials. Knowing the energy, the required Hugoniot pressure and shock particle velocity can be estimated, and thus, compared directly with results by Anderson et al[1)] . Table 3.2 summarises the results where projectile and target are constituted of the same material.

Differences in the data exist and are typically about 4% for the velocity and 3% for the pressure. The differences in the data exist for three reasons:

- Firstly, we assumed that the ambient pressure was zero, while in Anderson's et al. treatment the pressure was one atmosphere.
- Secondly, the value of the specific heat used by Anderson et al. was averaged over a wide temperature region. Although, the same approach has been used in treatment, it is quite possible that the final value will be different.
- Thirdly, the Mie-Gruneisen EoS used instead of Tillotson.

Thus, we have shown, that although, two different EOS were used the results are consistent and agree with published data.

3.4 Impacts of Fe on Au & W

In this section we present results for residual temperatures of Gold and Tungsten (when impacted by Iron particles), against projectile velocity as calculated using the approach discussed in section 3.2. In addition, results using the Nagayama approach, discussed in section 2.3.3.6, are also presented for comparison.

In the 70s Eichhorn [10-13)] performed experiments using the 2MV Van de Graaff dust accelerator facility of Max-Planck-Institut to estimate ejecta temperatures during a hypervelocity impact. To obtain the temperature of the luminous ejected material, the light flash energy was measured in different wavelength intervals. The measured spectra were compared against calculated model spectra to obtain the spectral temperature. The model spectra were calculated with the assumption that the light is mainly due to black body radiation. He used several projectile-target combinations. Two of them are Fe onto Au and Fe onto W.

Figures 3.1 and 3.2 illustrate the ejecta residual temperatures from the Eichhorn experiments and the theoretical values calculated with the approaches by Anderson and Nagayama.

Table 3.1: Material parameters used in this chapter [8,33)]

	ρ_0 (g/cm^3)	C_0 (km/s)	s	γ_0	C_v 10^{-3} MJ/kgK	T_m ^{0}K	T_v ^{0}K
Al	2.712	5.38	1.22	1.52	1.0000	933	2753
Cd	8.639	2.48	1.64	2.20	0.2445	594	1038
Rh	12.45	4.807	1.38	1.88	0.3000	2233	3960
Ag	10.5	3.27	1.55	2.38	0.2700	1234	2468
Cu	8.933	3.94	1.49	1.99	0.4430	1356	2811
Ni	8.9	4.59	1.44	1.93	0.5660	1726	3065
Co	8.862	4.77	1.28	1.99	0.6260	1765	3229
W	19.224	4.029	1.24	1.54	0.1810	3653	6000
Au	19.3	3.07	1.54	2.97	0.1440	1336	3240
Mo	10.208	5.14	1.22	1.52	0.2400	2883	5833
B_4C	2.4	7.898	1.14	1.27	-	-	-
Pb	11.346	2.03	1.47	2.77	0.1423	600	2013

Table 3.2: Impact conditions for phase changes.

Target	Incipient Melting				Complete Melting				Incipient Vaporisation			
	Ref. 1		this work		Ref. 1		this work		Ref. 1		this work	
	U_p km/s	P_H GPa	U_p km/s	P_H GPa	U_p km/s	P_H GPa	U_p km/s	P_H GPa	U_p km/s	P_H GPa	U_p km/s	P_H GPa
Al	2.77	68.2	2.85	71	3.45	94	3.45	94	5.46	188	5.20	174
Cd	0.93	32	0.90	31	1.17	44.5	1.15	43	1.51	64.7	1.50	64
Mo	2.58	218	2.75	238	3.04	274	3.15	289	3.93	399	4.00	409
Pb	0.79	28.6	0.80	29	0.95	37	0.95	37	2.00	113	1.85	100

One can, clearly, distinguish three different regions. A low impact velocity region ($U_0 <$ 5 km s^{-1}), an intermediate region (5 km $s^{-1} < U_0 <$ 8 km s^{-1}) and a high one ($U_0 >$ 8 km s^{-1}). In the low velocity region, for both target materials, theoretical predictions underestimate the experimental values. This may be attributed to collisions in the ejecta which result in an increase of the ejecta temperature.

However, quite recently, Sysoev et al. (1997)[14] argued that for velocities of the order of 3 km/s, ion generation and temperature increase happens because of the electric field produced by the charged projectiles before impacting the target. Due to the surface electric charge of the projectile, an electric field is formed between the projectile and target. The electrons stimulate the desorption of atoms and ions from the particle surface accompanied by the heating and ionisation of the near-surface layer of the particle. The temperature can reach 25000 K for the case of a large microparticle charge when the projctile is 0.8-0.4 μm from the target. This process is also known as autoemission. Since, Eichhorn has used a Van de Graaff dust accelerator for his experiments, it is quite possible that such an effect is dominant at low velocities.

In the intermediate region, results agree, relatively well, with experimental data, while in the high region no theoretical predictions exist because, as explained in earlier section, the Mie-Gruneisen EOS has been used which cannot apply for the vapour region.

3.5 Impacts of Fe on Soda - Lime Glass

In this section, theoretical calculations of residual temperature of glass are presented for the first time which will then be compared against experiments performed by the author using the Van de Graaff accelerator facility of UKC.

As explained is section 3.1, in order to find residual temperatures, the two constants of the shock - particle velocity should be known, the Gruneisen coefficient, melting / vaporisation temperatures, latent heat of melting and specific heat at constant pressure. Unfortunately, such parameters are not yet available for soda - lime glass. Therefore, an approximation was made for them. In Reference (15) Johnson and Holmquist describe a model for glass behaviour under shock wave loading. Further information about the model will be given in chapter 5. They have used a polynomial relation for shock pressure and density,

$$P = K_1\mu + K_2\mu^2 + K_3\mu^3 \qquad (3.5.1)$$

Figure 3.1: Gold residual temperatures when impacted by Iron

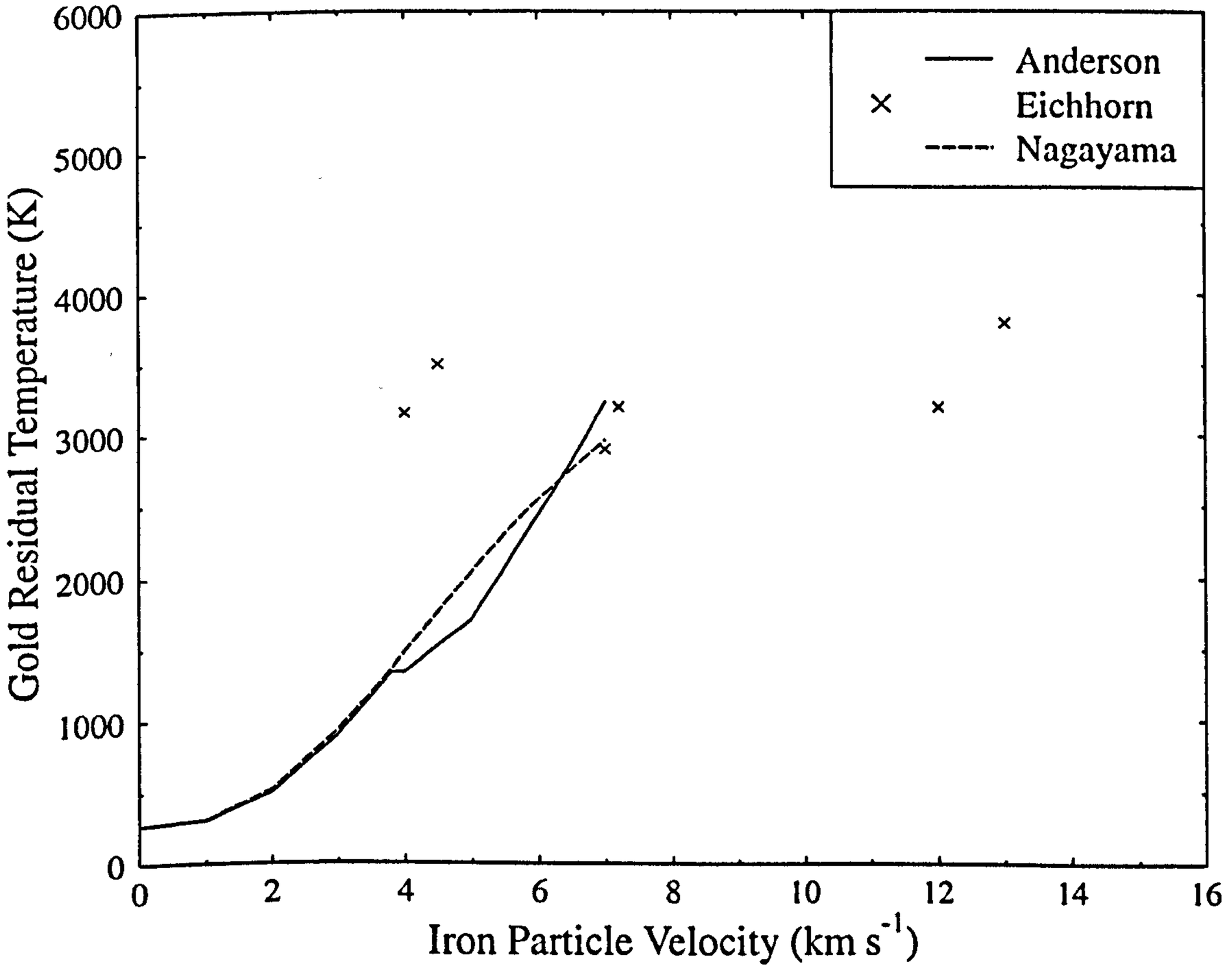

Figure 3.2: Tungsten residual temperature when impacted by Iron

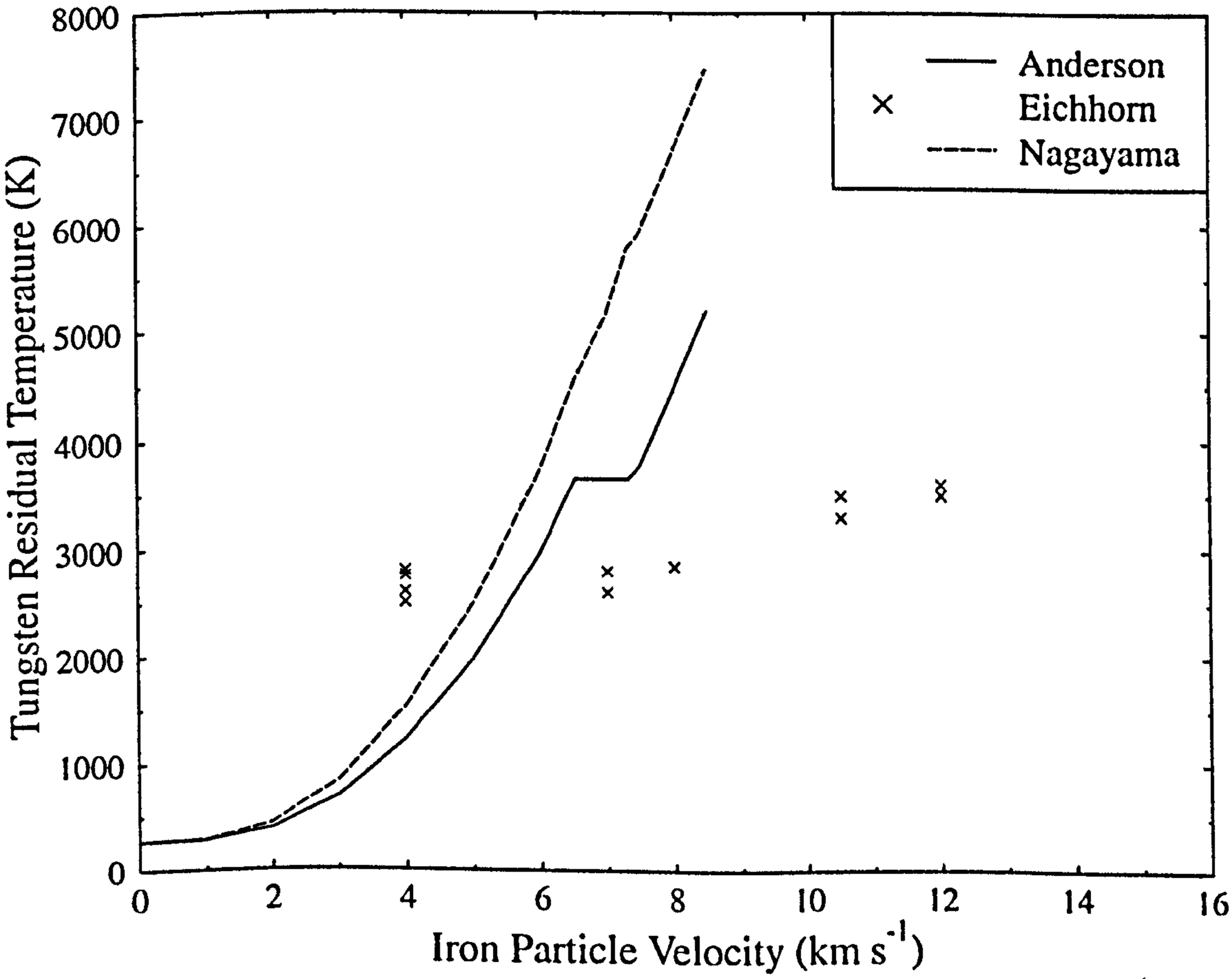

where K_1, K_2 K_3 are constants and $\mu = \rho/\rho_0 - 1$. The values of the constants are 45.4 GPa, -138 GPa and 290.0 GPa respectively. If we fit this Hugoniot curve to a shock - particle velocity we get values for c_0 and s which are 3.3 km/s and 1.5 respectively. Both curves are illustrated in Fig. 3.3.

However for the Gruneisen coefficient we chose five different values and all of them were used to find the residual temperatures. The first value is the coefficient for Quartz [8] . The second value comes from Alwes (1990)[16] , and the last three have been calculated using the program developed by Nagayama and Mori (1994)[17] and described in section 2.3.3.1. Table 3.3 summarise the values for this coefficient.

In addition, from Alwes paper we get an estimation for the melting temperature of glass ($T_m = 1400$ K). However, since there are no data for vaporisation temperature and latent heat of fusion and vaporisation, we had to make the assumption that (since soda - lime glass is mainly constituted of silicon dioxide) that glass is very similar to SiO_2; hence it was possible to acquire the remaining values from Reference (18). Table 3.4 summarises the values taken from that Reference. From table 3.4, the latent heat of fusion n_f can be found.

$$n_f = T_m (\Delta S_{cm} - \Delta S_{im}) \qquad (3.5.2)$$

In the case of the melting temperature, we take the mean value between the value by Alwes and the one for SiO_2. Hence $T_m = 1697$ K and the value for the latent heat of fusion is 0.117 MJ / kg.

Figures 3.4 and 3.5 show the common pressure and glass residual temperatures when iron impacting glass for different glass Gruneisen coefficients. As the Gruneisen coefficient increases the residual energy remained into the system decreases (since the amount of energy used for release increases) for the same impact velocity, therefore from Equations (3.1.8) it can be seen that as the Gruneisen coefficient is inversely proportional to the residual temperature for the same impact conditions. That is why, the curves in Figure 3.5 are shifted to the right as the Gruneisen coefficient increases. When γ_0 has a value of 0.9, the point of glass incipient vaporisation is at about 6 km s^{-1} iron impact velocity. In contrast, for the other values of γ_0 the temperature never reaches the value of vaporisation temperature. This, however, is not physical but represents the limitations of the Mie-Gruneisen EOS for high velocities.

Table 3.3: Different values used for the glass Gruneisen coefficient

Gruneisen Coefficient	Reference
0.90	Quartz [13]
1.32	Alwes [20] and MgO [13]
1.67	Nagayama and Mori t=2 [15]
2.0	Nagayama and Mori t=1 [15]
2.33	Nagayama and Mori t=0 [15]

Table 3.4: Thermodynamic properties of SiO_2 from ref. [3]

Entropy change for incipient melting ΔS_{im}	13.4 cal mol^{-1} K^{-1}
Entropy change for total melting ΔS_{cm}	13.73 cal mol^{-1} K^{-1}
Melting temperature T_m	1996 K
Vaporisation temperature T_v	3175K
Mean atomic weight	20.03 g mol^{-1}

3.6 Velocity threshold for impact plasma production

In October 1997 the Cassini/Huygens mission flew to the Saturnian system in order to study the planet and its satellites. One of the experimental systems on the Cassini mission is the Cosmic Dust Analyser (CDA) The CDA instrument is designed to determine particle flux rates and to measure, simultaneously, the charge, mass, velocity, trajectory and composition of individual dust particles. The system uses time-of-flight spectrometry of the positive ions in the plasma produced by the high velocity impacts of dust particles which allows their atomic species to be identified. Thus, the need to identify the threshold velocities required to produce ions of different species becomes apparent.

For that reason, experiments have been performed on the dust accelerator facilities at the University of Kent at Canterbury (UK) and the Max-Planck-Institut für Kernphysik (Germany) in which the production of plasma from impacts of micron and sub-micron particles from 1 to 90 km/s has been measured. Various projectile and target materials have been investigated.

The aim of the author is to calculate the velocity threshold from first principles for different projectile - target combinations. The approach used for such calculations is summarised in section 3.2 and results are presented in table 3.5. It has to be mentioned that the incipient vaporisation and not the complete vaporisation/onset of ionisation is calculated. It is assumed that collisions between gas molecules will produce some ions[9] . However, for comparative reasons the experimental data are also presented here together with results from molecular dynamics (MD) and computer simulation predictions.

Figure 3.3: Glass Hugoniot Curve

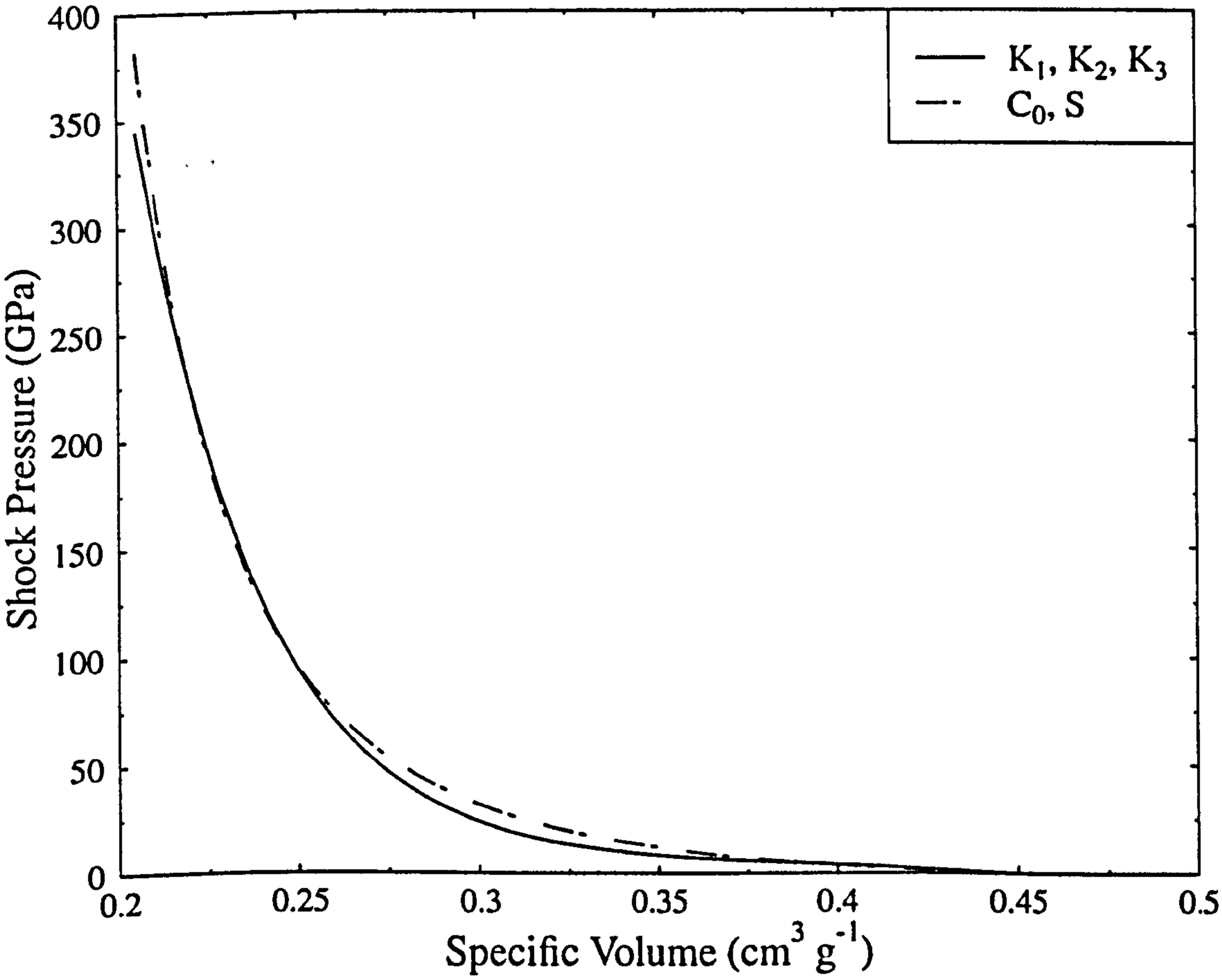

Figure 3.4: Common Shock Pressure at Interface when Iron impacts Glass

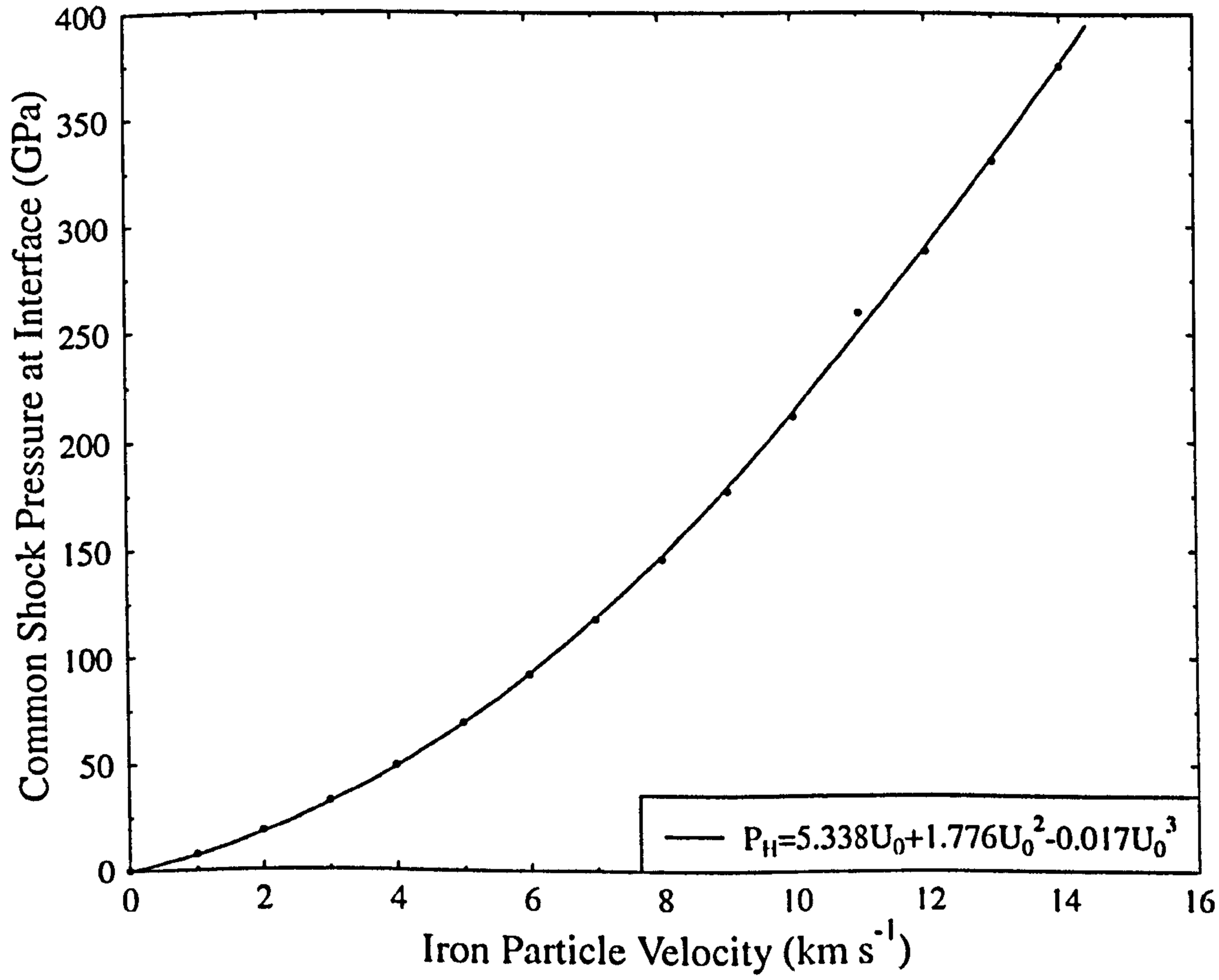

The experimental, MD and simulation work has been performed by PR Ratcliff and has been presented in COSPAR '96 [9].

The computer simulation predictions come from the use of the AUTODYN™ hydrocode[19] using the Tillotson Equation of State[20], which, as described in section 2.3.3.4, accounts for vaporisation of material.

However, an alternative approach to calculating threshold impact velocities for vaporisation is to use the principles of molecular dynamics. Instead of considering the material as a continuum described by bulk properties, material is considered on an atomic scale. At the impact velocities we are considering, atomic interactions can be considered to be elastic collisions (at higher velocities, corresponding to kinetic energies of many keV per atomic mass unit (amu) the interaction is with the 'electron plasma' of the solid through inelastic energy loss). The requirement to vaporise the material in either the projectile or the target is for the transfer of energy from the bulk kinetic energy of atoms in the projectile to thermal energy of atoms in the projectile and/or target to exceed the latent heat of fusion and the latent heat of vaporisation. The results are shown in Table 3.5. For the case of boron carbide as a target, no B or C species results exist because the impedance match method cannot apply for the individual constituents of a material.

From table 3.5, one can see that the results using the approach described in section 3.2 lie between the hydrocode predictions and the experimental data. In addition, the results are closer to the experimental values than any other approach used.

The approach used by the author is more advantageous than the molecular dynamics and the hydrocodes, when compared against the experimental data. Firstly, one must realise that hydrocode runs are expensive and time consuming. A few days, at least, are required for a given projectile-target combination in order to determine the velocity threshold. In addition, not all the combinations were possible to perform, due to lack of material parameters. On the other hand, the approach used by the author and the molecular dynamics require only a few hours for all the data to be calculated. However, the molecular dynamics results, when compared to the experimental data, agree to a lesser extent, than the author's results. One can calculate the percentage difference between the experimental value and the corresponding value from a given approach, that is, (experimental value - value from a given approach)/(experimental value)*100%. For a given projectile-target combination, the closer this number is to zero, the closer the value of a given approach is to the experimental value. Therefore, if the cumulative number of values happening in a given range for both approaches is plotted, then it is possible to

Figure 3.5: Glass Residual Temperature

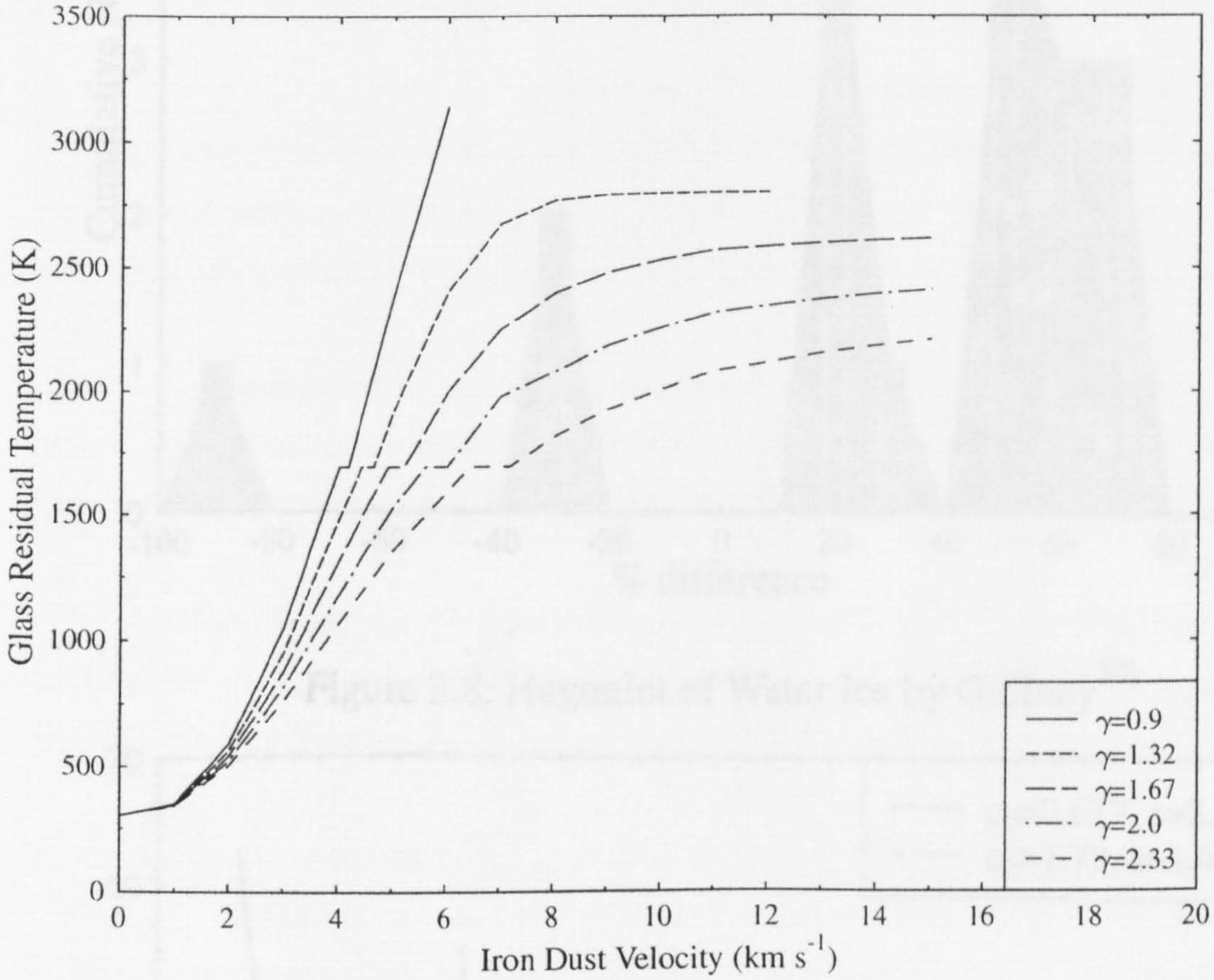

Figure 3.6: Cumulative number of results for theoretical approach

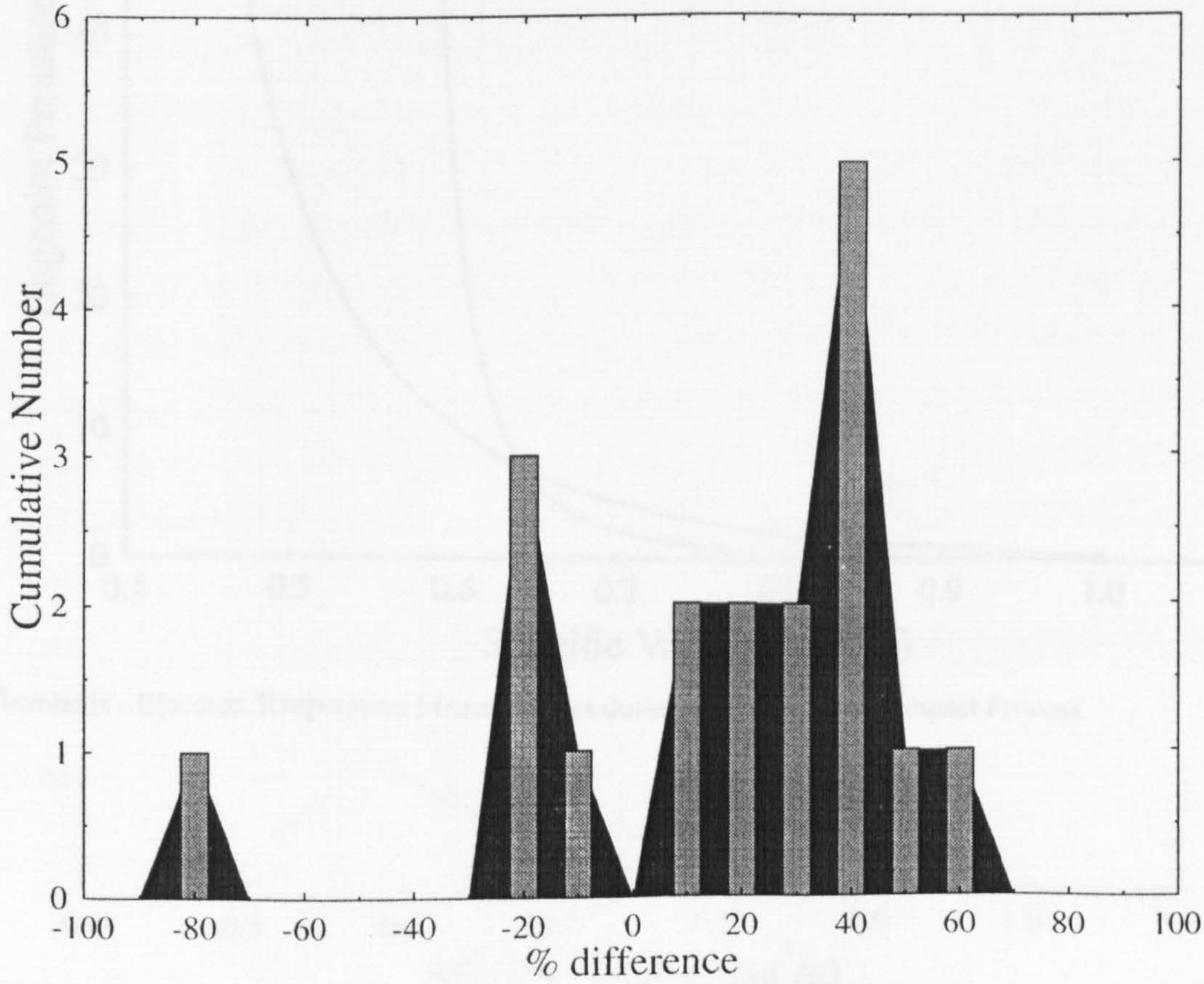

Figure 3.7: Cumulative number of results for Molecular Dynamics

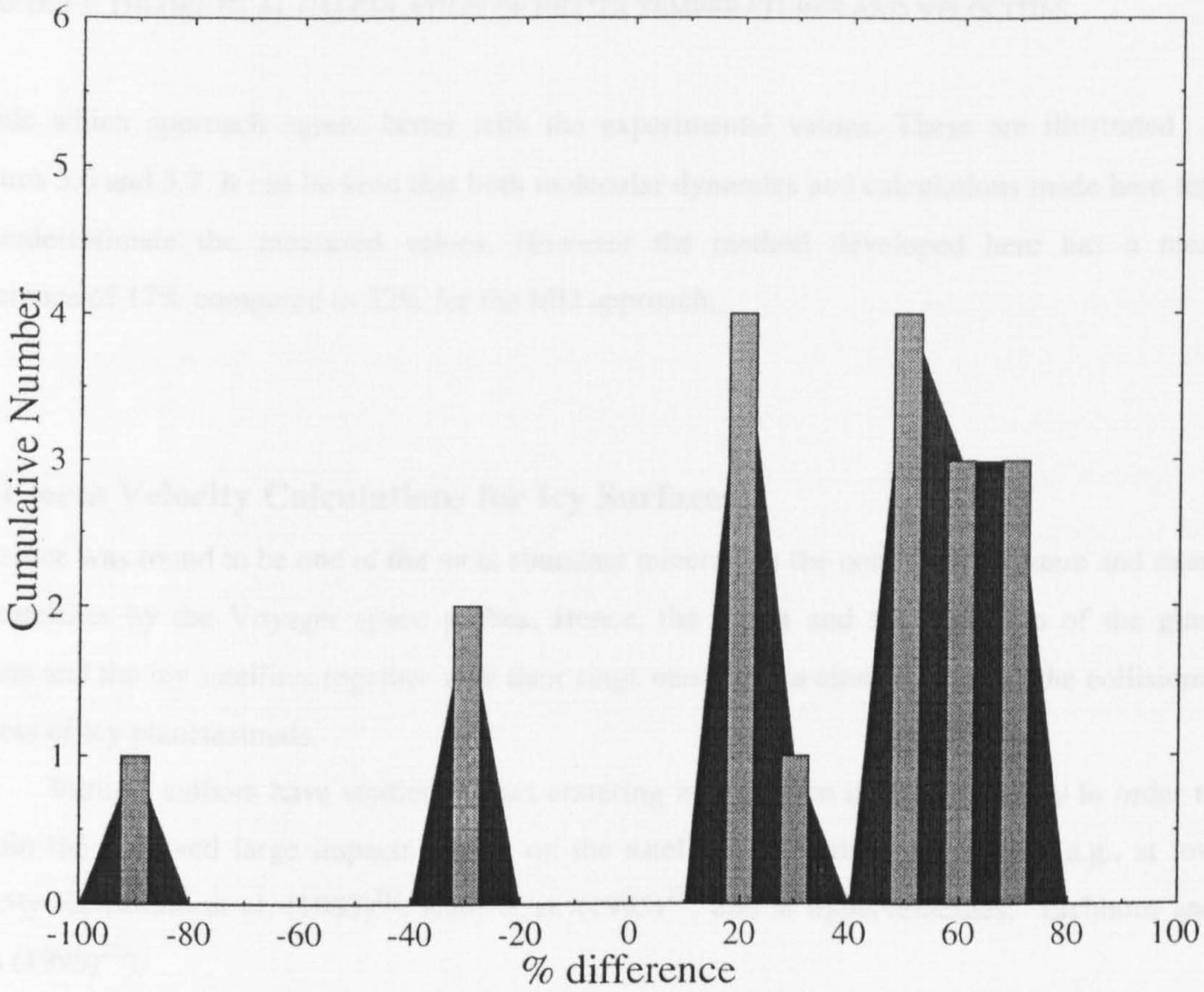

Figure 3.8: Hugoniot of Water Ice by Gaffney[30)]

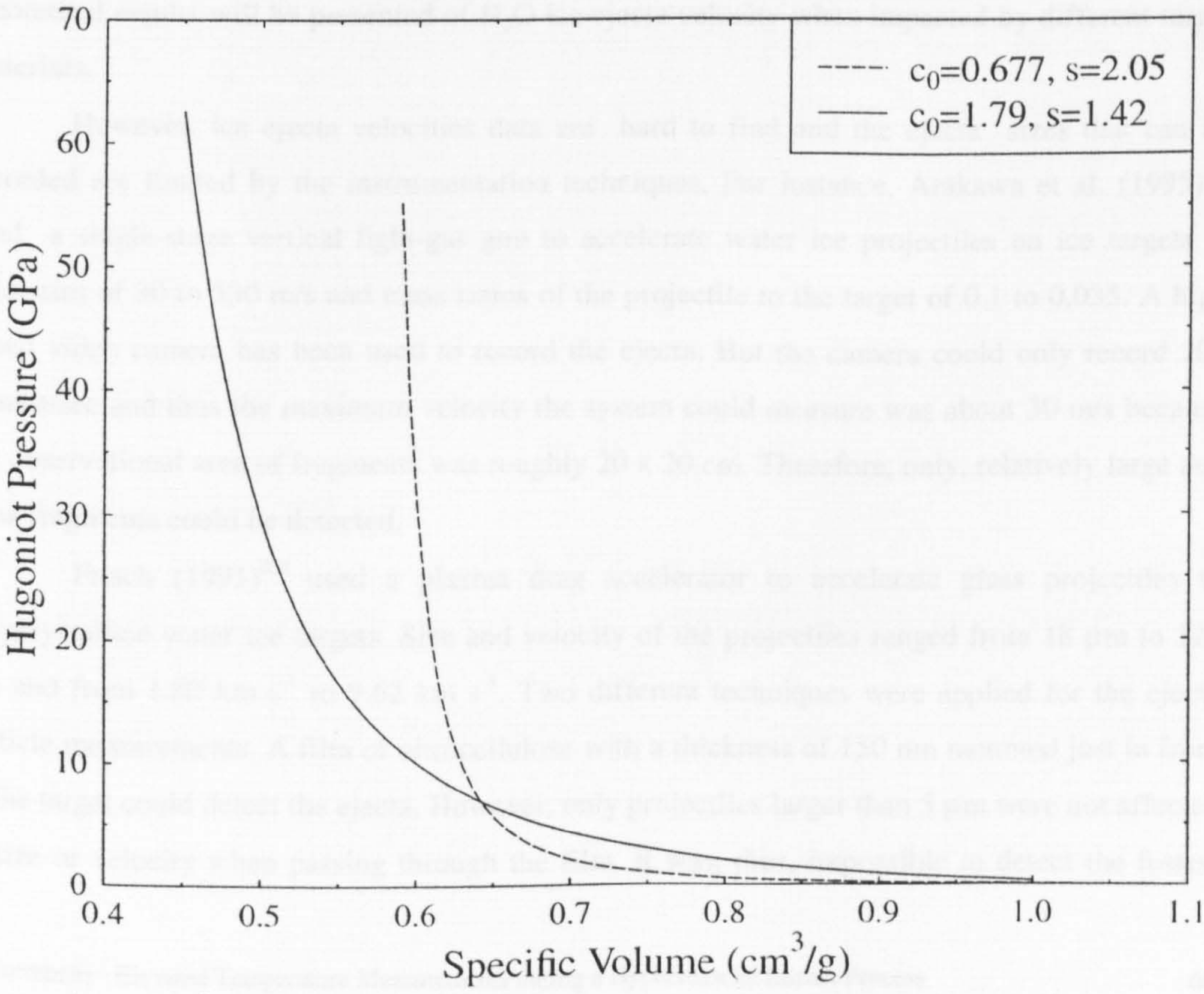

decide which approach agrees better with the experimental values. These are illustrated in Figures 3.6 and 3.7. It can be seen that both molecular dynamics and calculations made here tend to underestimate the measured values. However the method developed here has a mean difference of 17% compared to 32% for the MD approach.

3.7 Ejecta Velocity Calculations for Icy Surfaces

Water ice was found to be one of the most abundant minerals in the outer Solar System and many icy satellites by the Voyager space probes. Hence, the origin and the evolution of the giant planets and the icy satellites together with their rings must have a close relation to the collisional process of icy planetesimals.

Various authors have studied impact cratering in water ice in the laboratory in order to explain the observed large impacts craters on the satellites of Jupiter and Saturn (e.g., at low velocity Kawasami et al. (1983)[21], Kato et al. (1995)[22], and at hypervelocities, Eichhorn and Grün (1993)[23]).

The velocity of the ejecta after an impact on ice is, thus, very important in understanding many processes taken place during the early stages of the Solar System. In this section, theoretical results will be presented of H_2O ice ejecta velocity when impacted by different target materials.

However, ice ejecta velocities data are hard to find and the ejecta sizes that can be recorded are limited by the instrumentation techniques. For instance, Arakawa et al. (1995)[24] used a single-stage vertical light-gas gun to accelerate water ice projectiles on ice targets at velocities of 30 to 530 m/s and mass ratios of the projectile to the target of 0.1 to 0.035. A high speed video camera has been used to record the ejecta. But the camera could only record 200 frames/sec and thus the maximum velocity the system could measure was about 30 m/s because the observational area of fragments was roughly 20 x 20 cm. Therefore, only, relatively large and slow fragments could be detected.

Frisch (1991)[25] used a plasma drag accelerator to accelerate glass projectiles to polycrystalline water ice targets. Size and velocity of the projectiles ranged from 18 μm to 124 μm and from 1.80 km s^{-1} to 9.62 km s^{-1}. Two different techniques were applied for the ejecta particle measurements. A film of nitrocellulose with a thickness of 150 nm mounted just in front of the target could detect the ejecta. However, only projectiles larger than 5 μm were not affected in size or velocity when passing through the film. It was, thus, impossible to detect the fastest

and smallest ejecta which could, even, be in the vapour state. Piezoelectric sensors were also used as a second detection technique. The detectors were built of piezoelectric plates with a sensitive area of 250 mm^2. Similar problems exist in this approach.

Finally, Burchell et al. (1996)[26] used a Van de Graaff dust accelerator in order to accelerate micron- and submicron- iron particles at velocities of 2 km s^{-1} to 65 km s^{-1}. In this case, the signal from the secondary ionisation observed by a photomultiplier tube was interpreted as the observation of ionisation caused by impacts of high-speed ejecta. Assuming an angle of ejection of 60^0 to the target surface, ejection velocities could be measured. A correlation was established between ejecta velocity and projectile impact velocity

$$U_{ej} = 0.093\ U_0^{1.13} \tag{3.7.1}$$

However, only the relatively large ejecta had enough kinetic energy to produce a secondary ionisation.

For the rest of this section, we present one dimensional ice ejecta velocity calculations when impacted by glass, water ice and iron projectiles and we argue for the need of better detection techniques.

In order to calculate the ejecta velocity, the Hugoniot and the Gruneisen coefficient must be known. However, water ice is a complicated material with many phases[27]. Hugoniot data have been presented by Anderson (1968)[28], Larson (1984)[29] and Gaffney (1985)[30]. Gaffney has distinguished two different curves in the P-V plane. The first curve lies in the low pressure region where the pressure is between 600 MPa, (above the Hugoniot Elastic Limit) and 2.2 GPa and a high pressure region where the pressure exceeds 8 GPa. In the intermediate region there is a wide discrepancy in the results. Anderson attributes this to poor data in one of his experiments, while Larson reports a state between Anderson's points.

Thus the two regions are:

1. When Pressure $P \in [0.6, 2.2]$ GPa

$$U_S = 0.677\ (km/s) + 2.05\ u_p \tag{3.7.2}$$

2. When Pressure P exceeds 8 GPa

$$U_S = 1.79\ (km/s) + 1.42\ u_p \tag{3.7.3}$$

Both curves appear in Figure 3.8. A value for the Gruneisen coefficient was found in Reference (31) to be 0.35. Using these values we can predict the ice ejecta velocity against impact velocity for different projectiles. Figure 3.9 illustrates such results for three different projectile materials: iron,

Figure 3.9: Ice Ejecta Velocity for different Projectiles

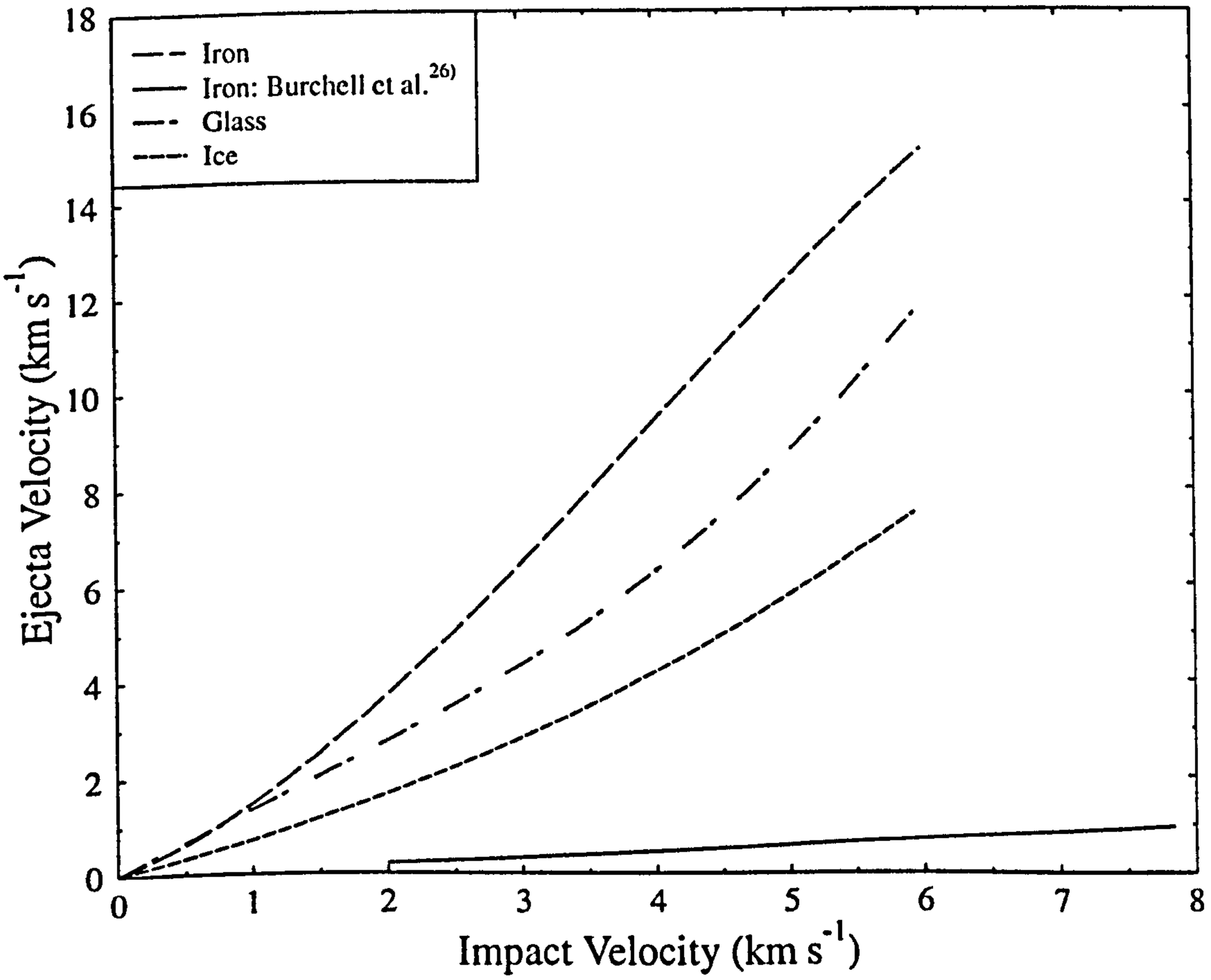

Figure 3.10: Cloud Ejecta Velocity when Nylon impacted Copper

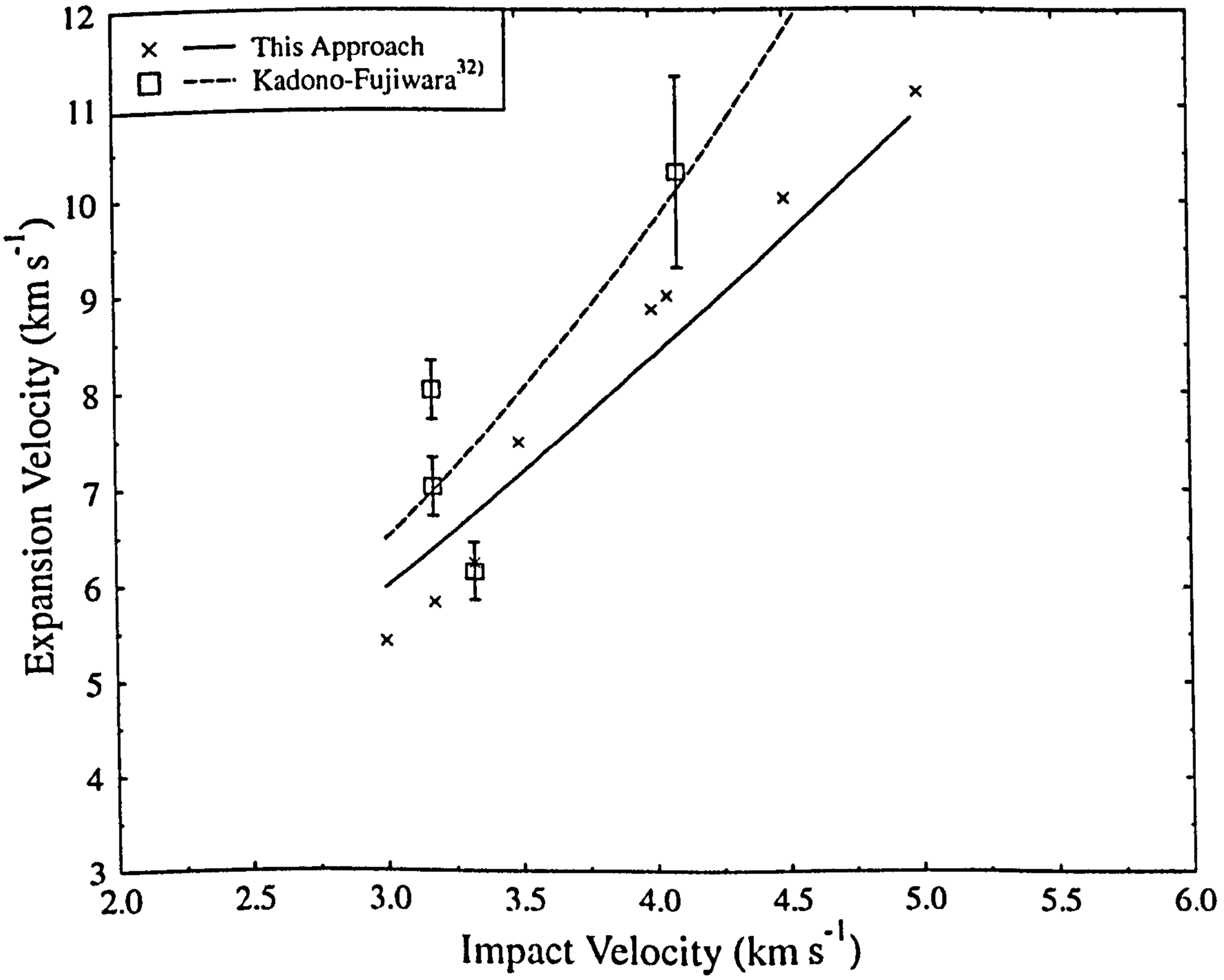

Table 3.5: Summary of results for vaporisation threshold velocities (km/s)

Projectile and target	Species	Experiments	This approach	Molecular Dynamics	Hydrocode Sphere-Plate
Fe on Rh	Fe	16 (15)[1]	8.16	6.4	6
	Rh	16 (15)	8.44	7.0	-
Fe on Al	Al	8 ± 3[2]	9.02	6.1	20
	Fe	8 ± 3	13.69	9.8	8
Fe on Mo	Fe	23 (22)	8.73	5.1	8
	Mo	19 (18)	9.88	7.1	26
Fe on Au	Fe	15 ± 2	7.55	4.1	5
	Au	?	6.97	7.9	-
Fe on Ag	Fe	10 ± 5	8.79	4.9	8
	Ag	10 ± 5	6.02	6.2	-
Fe on Ni	Fe	?	9.01	6.4	8
	Ni	8 ± 1	9.09	6.4	22
Fe on Cu	Fe	8.4 (7.7)	8.93	6.0	7
	Cu	8.7 (8.4)	7.58	6.2	16
B_4C on Ag	B	11.6 (11.4)	-	-	-
	C	6.3 (4.7)	-	-	-
	Ag	11.6 (11.4)	9.12	21	-
Al on Co	Al	21 ± 5	8.81	6.1	8
	Co	21 ± 5	14.78	9.8	-
Al on C	C	20 ± 5	-	-	-
	Al	19 ± 2	-	13.3	-
Al on Fe	Al	18 ± 5	9.02	6.1	8
	Fe	22 ± 5	13.69	9.8	17
C on Fe	C	16 ± 2	-	-	-
	Fe	15 ± 4	17.46	18	-

[1] If the measured threshold velocity is followed by a number in brackets, the stated velocity is the lowest at which the given line was observed and the number in brackets is the next highest velocity in the data set at which the line was not observed (i.e. the minimum possible value of threshold).

[2] ± indicates the error on the threshold velocity derived by extrapolating the fit to the data to zero yield.

glass and ice. For comparison purposes, results by Burchell et al.[26] (Equation (3.7.1)) is also illustrated.

It can be seen that there is a great discrepancy between theoretical predictions and experimental data, as expected. Theoretical approach can evaluate the maximum possible speed of the ejecta of a given impact. However, only the smallest fragments will have this velocity, which, as discussed above, are difficult to detect. Fortunately, new cameras, such as image converter cameras, make such detection possible. Kadono and Fujiwara (1996)[32] have used an IMACON 790 to observe the expanding vapor cloud generated by a hypervelocity impact.

Pictures of the impact were taken with a framing speed of 1 million frames per second! It was, thus, possible to detect the vapor cloud moving at velocities of 10 km/s. Nylon projectiles 7 mm in diameter were accelerated onto Nylon and Copper targets at velocities of 3 km/s to 6 km/s using a two stage light gas gun. Figure 3.10 illustrates the experimental results together with the theoretical predictions. It is apparent that the theoretical results are consistent with the experiments. Therefore, the need for such cameras becomes apparent.

3.8 Conclusion

In this chapter, a method to calculate residual temperatures and ejecta velocities of a hypervelocity impact was developed and described. This method was tested against known temperature data [1,12] used to evaluate glass residual temperatures when impacted Iron. These results will be compared against experiments at chapter 4.

In addition, this method was used to predict velocity threshold for impact plasma production. Such calculations are important for the calibration of the Cassini Cosmic Dust Analyser (CDA). Results using this method agree with experimental data to a bigger extent than other methods used such as molecular dynamics and are faster than hydrocode runs.

Finally, previous work on ice ejecta velocities has been summarised and theoretical predictions of ice ejecta speeds have been presented when water ice is impacted by glass, ice and iron. Also, the need for new detection techniques, such as IMACON image converter camera, has been argued and discussed.

References

1. Anderson, C E et al., (1990), "Debris Cloud Dynamics", *Int. J. Impact Engng*, **9**, 89-113.
2. Ratcliff P R, et al., (1992), "The Cosmic Dust Analyser", *J. British Interplanetary Soc.*, **45**, 355-358.
3. O' Keefe J D and Ahrens T J, (1977), "Impact-induced energy partitioning, melting, and vaporisation on terrestrial planets", *Proc. Lunar Sci. Conf. 8th*, 3357-3374.
4. Rinwood A E, (1975), "Composition and Petrology of the Earth's Mantle", McGraw-Hill, NY.

5. Cameron A G W, and Ward W R, (1976), "The origin of the Moon", *Lunar Science VII*, 120-122.
6. Adkins C J, (1983), "Equilibrium Thermodynamics", 3rd ed., Cambridge University Press.
7. Melosh H J, (1989), "Impact Cratering: A Geologic Process", Oxford University Press, NY.
8. Asay J R and Shahinpoor M (eds), (1993), "High-Pressure Shock Compression of Solids", Springer-Verlag, NY.
9. Ratcliff P R, et al. (1997), "Velocity Thresholds for Impact Plasma Production", *Adv. Space Res.*, **20**, 1471-1476.
10. Eichhorn G, (1975), "Measurements of the Light Flash produced by High Velocity Particle Impact", *Planet. Space Sci.*, **23**, 1519-1525.
11. Eichhorn G, (1976), "Analysis of the Hypervelocity Impact Process from Impact Flash Measurements", *Planet. Space Sci.*, **24**, 771-781.
12. Eichhorn G, (1977), "Heating and Vaporisation during Hypervelocity Particle Impact", *Planet. Space Sci.*, **26**, 463-467.
13. Eichhorn G., (1977), "Primary Velocity Dependence of Impact Ejecta Parameters", *Planet. Space Sci.*, **26**, 469-471.
14. Sysoev A A , et al., (1997), "Mass Spectra formation from charged microparticles", *Nucl. Instr. And Meth. In Phys. Res. B*, **122**, 79-83.
15. Holmquist T J, et al., (1995), "High Strain Rate Properties and Constitutive Modeling of Glass", 15th Int. Symp. On Ballistics.
16. Alwes D, (1990), "Columbus-Viewport Glass Pane Hypervelocity Impact Testing and Analysis", *Int. J. Impact Engng*, **10**, 1-22.
17. Nagayama K and Mori Y, (1994), "Simple Method of Calculating Grüneisen Parameter Based on the Shock Hugoniot Data for Solids", *J. Phys. Soc. Jap.*, **63**, 4070-4077.
18. Ahrens T J and O' Keefe J D, (1971), "Shock Melting and Vaporisation of Lunar Rocks and Minerals", Conf. Lun. Geophys.
19. Birbaum N K , et al., (1987), "AUTODYN- an Interactive Non-Linear Dynamics Analysis Program for Microcomputers to Supercomputers", 9th Int. Conf. On Struct. Mech. In Reactor Tech.
20. Tillotson J H , (1962), "Metallic Equations of State for Hypervelocity Impact", Gen. Atomic Rep. AG-3612.
21. Kawasami S, et al., (1983),"Impact Experiments on Ice", *J. Geophys. Res.*, **B88**, 5806-5814.
22. Kato M, et al., (1995), "Ice-on-Ice experiments", *Icarus*, **113**, 423-441.

23. Arakawa M, et al., (1995), "Ejection Velocity of Ice Impact Fragments", *Icarus,* **118**, 341-354.

24. Eichhorn G and Grün E, (1993), "High Velocity Impacts of Dust Particles in Low-Temperature Water Ice", *Planet. Space Sci.*, **24**, 771-781.

25. Frisch W, (1991), "Hypervelocity Impact Experiments with Water Ice Targets", in *Hypervelocity Impacts in Space*, (McDonnell J A M, Ed.), 7-14.

26. Burchell M J, et al., (1996), "Light Flash and Ionisation from Hypervelocity Impacts on Ice", *Icarus*, **122**, 359-365.

27. Kamb B, (1965), "Structure of Ice VI", *Science*, **150**, 205-209.

28. Anderson G D , (1968), "The Equation of Sate of Ice and Composite Frozen Material", *US Army Cold Reg. Res. & Eng. Lab. Res,.* **Rept. RR-257.**

29. Larson D B , (1984), "Shock Wave Studies of Ice under Uniaxial Strain Conditions", *J. Glacial.*, **30**, 235-240.

30. Gaffney E S , (1985), "Hugoniot of Water Ice", *In Ices in the Solar System* (Klinger J, Benest D, Dolfus A, and Smoluchowski R, Ed.),ASI, 119-148.

31. Tanner W G, (1995), "Meteoroids and Space Debris Hypervelocity Impact Penetrations: The Role of Hydrocodes", thesis.

32. Kadono T and Fujiwara A, (1996), "Observation of Expanding Vapor Cloud Generated by Hypervelocity Impact", *J. Geophys. Res.*, **101**, 26097-26109.

33. Y. S. Touloukian (Ed.), (1970), 'Thermophysical Properties of Matter', Plenum, N.Y.

CHAPTER 4

Elevated Temperatures at impact using the 2MV Van de Graaff

4.1 Introduction

A very well known phenomenon of hypervelocity impact is the melting, vaporisation and ionisation of both target and projectile. Therefore, upon such impacts large amounts of hot and radiative material are ejected. Such ejecta material is, quite often, referred to as plasma, because it may contain large amounts of ionised material. The light emanating from this kind of material is called light flash.

Because of the high velocities involved, light flash production under hypervelocity impact happens frequently in the space environment. An example of such impacts are the meteor phenomena or shooting stars in every day language. When a piece of extraterrestrial material enters the Earth's atmosphere at high velocities, air and meteor material are ionised, which then radiate light, and hence are visible with the naked eye; they can also be detected by their radar signatures. In this example, the target is a gas (the atmosphere) and the light is emitted from the gas heated by the passage of the meteor as well as from its heated surface.

CHAPTER 4: ELEVATED TEMPERATURES AT IMPACT USING THE 2MV VAN DE GRAAFF

Large scale impacts on planetary surfaces or natural satellites can produce light flashes. Such large impacts on solid surfaces are infrequent and few reliable observations exist. A recent well observed impact did not involve a solid surface but a dense gaseous atmosphere i.e. comet Shoemaker-Levy 9 impacting on Jupiter. The fire ball of the hot ejected material was seen even by the old probe Voyager which was 70 A.U. away from our sun.

The Giotto probe which flew to Halley's comet during its most recent passage through the inner Solar System, had an instrument used for ion spectroscopy to try and look at elemental composition of particles emitted by the comet. The basic principle was that a small dust particle would impact a target generating an impact plasma. An applied electric field was then used to accelerate the ions and their arrival time at a detector depends upon the mass of the individual ion species involved. To operate properly such a system needed a start time for the impact at beginning of the drift process. That start time was provided by the light flash of the signal impact.

Light flash investigation is also important for some monitoring satellites. Space borne optical sensors (known as bahngmeters) can be mounted on satellites to monitor Earth-based missile launch activity[1]. However, cosmic dust and space debris may impact on the sensors, thus giving a false signal. It is thus important to study the nature of such signals in order to determine the difference between a flash from an impact on the sensor and signal from a distant missile launch. It is therefore no surprise that the US Air Force maintain an interest in studies of impact light flash.

Glass is an increasingly important material as it is increasingly present on spacecrafts in the form of ever larger solar arrays and windows on vehicles such as the space shuttle ant the new international space station. In this chapter we present results of impact of iron particles onto soda-lime glass using the Van de Graaff dust accelerator facility of the University of Kent at Canterbury. Intensity of the light flash was measured for two different wavelengths at a velocity range of 5 - 20 km s^{-1} and the temperature of the ejecta cloud was found assuming black body radiation emission. The temperature was found to be almost independent of impact velocity. The results are then discussed in the context of previous attempts to measure the ejecta cloud temperature both experimentally and computationally.

4.2 Experimental Arrangement

4.2.1 Experimental set up

We begin by presenting a general overview of the experimental set up which is illustrated in Figure 4.1. Iron dust particles were accelerated towards a glass target by means of the 2MV Van de Graaff dust accelerator facility of the UKC. Velocities in the range 5 - 20 km s^{-1} were attained for particles of mass 10^{-14} - 10^{-17} kg. A detailed description of this dust source is given by Green at al. (1988)[2]. In section 4.2.2 a brief summary of the dust accelerator will be given.

The dust was accelerated into a chamber evacuated to 1 to $2x10^{-6}$ mbar. The glass target was a normal microscope slide with dimensions of 7x3x0.5 mm. The glass was attached to an aluminium holder placed at the centre of the chamber and perpendicularly to the beam line. The set up was such that the dust beam could impact the centre of the glass. In addition, the holder was painted black and the whole chamber was covered with black plastic to reduce light reflections. Ten viewports, placed at 36^0 apart to each other, existed around the chamber. Two photomultiplier tubes types EMI 9789Q and EMI 6097 were placed, symmetrically and at 36^0 to the beam direction, in two of these viewports by means of glass windows. Thus, no ultra violet light could be transmitted. Both tubes were operated in integration mode. Hence, the total magnitude of the signal was proportional to the total energy of an event. Since the tube signals were integrated, τ=247 ms, the rising time of the signal represented the duration of the event. The EMI 6097 was operated at 1.4 kV by a Harwell power supply, while the EMI 9789Q was operated at 1.3 kV by an EMI 3000R supply. Both tubes were connected to a LeCroy 9304 oscilloscope (100MS s^{-1}).

Filters at specific wavelengths were placed in front of the tubes. In this way, assuming black body radiation for the light flash, it was possible to estimate the ejecta temperature. However, in order to convert the tubes' signals to energy, the photomultiplier tubes had first to be calibrated against a source of known emission. The actual calibration is given in section 4.2.3.

The filter placed in front of the EMI 9789Q was a bandpass one with peak wavelength of 400 nm, 65.7 nm half bandwidth and 51% transmission. The filter placed in front of the EMI 6097, was a combination of a short and long pass filter. The end filter was equivalent to one having 550 nm peak wavelength, 50nm half bandwidth, and 66.4% transmission. After correcting for filter bandwidth and transmission and the solid angle subtended at the target by the PM tubes, it is possible to estimate the energy of the flash at 400 nm and 550 nm, since both tubes had already been calibrated against a known source.

4.2.2 The Van de Graaff Dust Particle Accelerator

Since a Van de Graaff (VdG) is an electrostatic accelerator the dust particles used must be charged before they can be accelerated. A small reservoir of dust was placed at the top terminal end of the VdG. The dust used here was iron dust. The dust is spherical to a high degree with a size range of 0.01 to 3 microns diameter. Before being placed in the VdG the dust was dried in a small vacuum oven. This prevented any clumping of the fine powder.

The dust reservoir had front and rear surface plates across which a dc pulsed voltage is applied. The rear plate has a needle attached horizontally, pointing at a hole in the front plate. This is above the level of the dust and is aligned with the main axis of the VdG. The pulsed voltage stimulates the dust which start to travel between the two plates. Any dust particle reaching the needle tip receives the maximum charge and on its passage towards the front plate passes through the hole, out of the reservoir and into the main flight tube.

The flight tube has 52 ring electrodes which have a voltage difference V_A between the electrodes and ground of about 2 million Volts. Therefore the charged particles can accelerate, as their electrostatic energy qV_A is converted to kinetic energy. Thus one may write

$$\tfrac{1}{2} mv^2 = q(V_A + V_C) \qquad (4.2.2.1)$$

where m is the particle mass, v its final velocity, q its charge, V_A the accelerating voltage and V_c the needle charging potential. Note that, although the potential is about 2MV, due to the mass of the particles the acceleration is totally non-relativistic. From Eq. (4.2.2.1), it can be seen that the velocity v is a function of the ration q/m. For fully efficient charging, the charge is a surface effect, and thus q/m is fixed at a given mass for a given dust material type (assuming perfectly spherical projectiles). Therefore, with a relatively, small spread, there is only one velocity for a given mass particle, and the highest velocities are associated with the smallest masses. This is shown in Figure 4.3, where the data for the iron particles accelerated to the glass target is presented.

Therefore, in order to estimate the mass of a particle, the other three parameters must be known. When a particle is inside the main flight tube, it passes through a detector, called the Compact Time Of Flight (CTOF). The detector consists of two copper rings at known distance apart. When a particle passes through the detector it induces a charge on each ring. The rings are connected to an oscilloscope via an amplifier, hence two signals appear on the oscilloscope screen. The time difference between them gives the velocity, since the distance between the rings is known. The particle velocity was, on average, accurate to ±1% at low velocities, rising to 5% at 20 km s^{-1}. The height of the signal, which is in mV, corresponds to the charge. The detector

and pre amps used have been calibrated by inssertion of known charge signals placed onto the detectors. The result is that 1 Coulomb of charge corresponds to 10.86 x 10^{12} Volt. The accelerating voltage is measured directly on the machine instrumentation.

For the data presented here, the VdG was run with voltages of 1.3 to 1.7 MV. This increases the lifetime of the machine by reducing the risk of sparking which is present at the high voltage. The mass range found here 10^{-17} to 10^{-15} kg corresponds to iron particles of between 0.14 and 0.63 microns. The range of charges on the particles was 1.18 to 9.6 fC.

Finally, all the event signals displayed on the oscilloscope are stored in a PC using LabView™. LabView™ is an icon oriented programming language sold by National Instruments. Programs written here use LabView™ on the PC to control data transfer from the oscilloscope to the PC. The same programs then permit subsequent recall and analysis of data. In this way, all the events can be re-examined. Thus, the signals that correspond to charge and light flash can be estimated to better than 1% accuracy.

4.2.3 Calibration of the Photomultiplier Tubes

For this experiment the photomultiplier tubes had to be absolutely calibrated. It was thus necessary to establish a relation between the signal (in mV) and the energy (in Joules) at a given wavelength. For that purpose, both tubes were calibrated against a continuous source of known characteristics. The lamp model used was G501 made by VCH Ltd. It had a tungsten filament at a temperature of 2410 K. The test voltage was 6.5 V, the current 300 mA ± 10% and the wattage was 1.95 W. The radiation characteristics of the lamp under these conditions were also provided by the manufacturer. However the actual energy output was of interest and not the radiated power, since the tubes were used in the integration mode. To calibrate the PM tubes the lamp was placed in a light tight box behind a baffle with a small opening. The PM tube being calibrated was placed at an external viewing port behind appropriate filters. Inside the light tight box between the lamp and the viewport was an opaque wheel with a circular hole. The wheel was 5 cm in diameter, the hole was 1 mm in diameter and positioned 4 cm radially from the centre of the wheel. Through the centre of the wheel was mounted the spindle of a 6V motor used to rotate the wheel at 36 Hz. Although the lamp was on continuously, the PM tube was only illuminated when the wheel rotated such that the hole was between the lamp and the PM tube. The set up is illustrated in Figure 4.2. Therefore, the energy of the light which comes out from the hole depends on the energy radiated

Figure 4.1: Experimental set-up

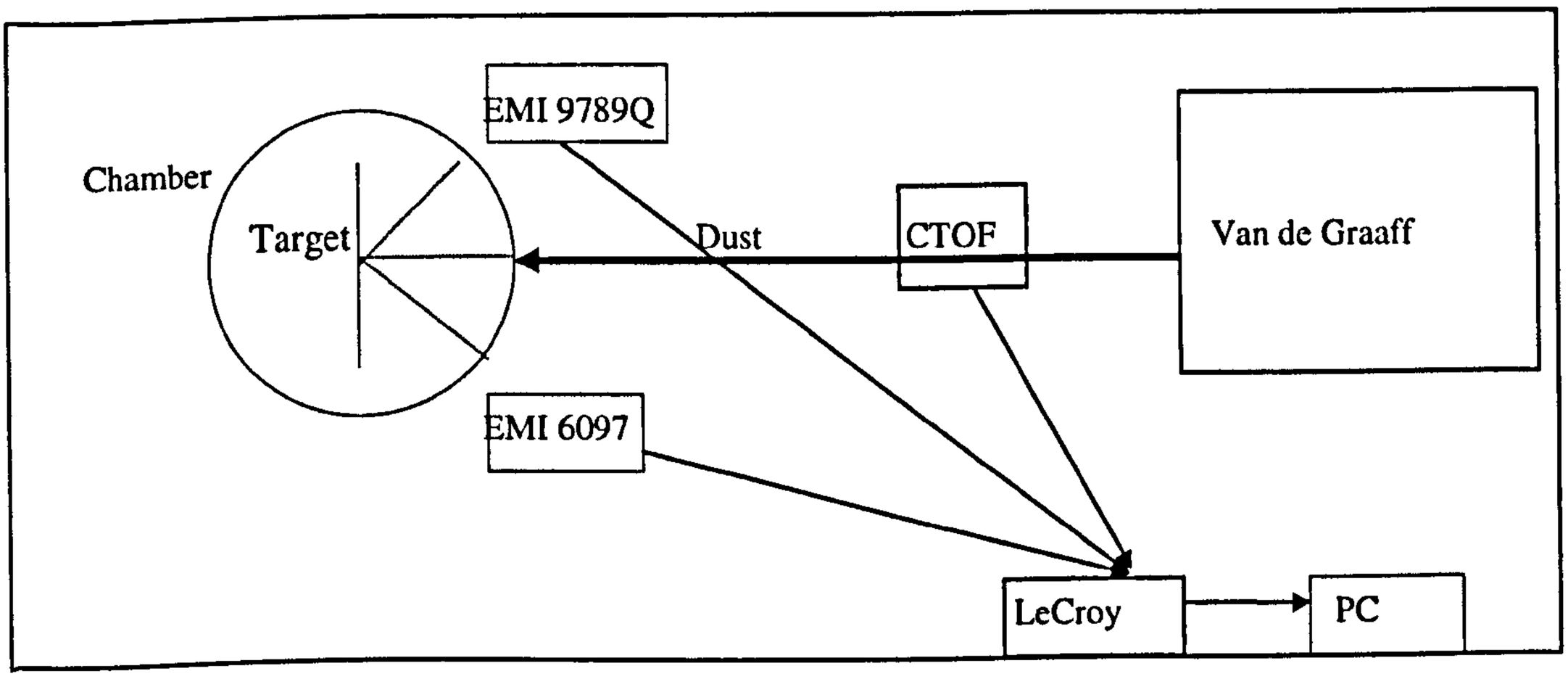

Figure 4.2: Photomultiplier calibration set up

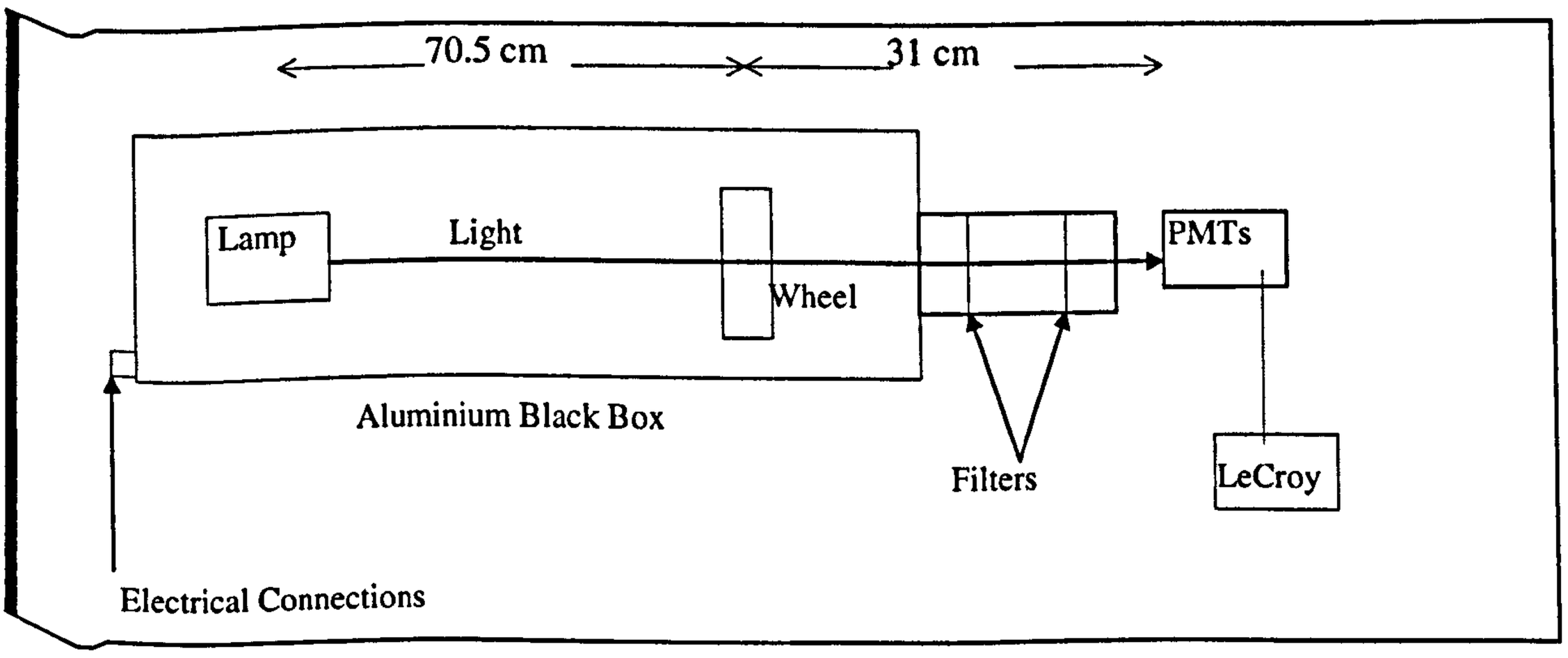

by the lamp the time the hole 'sees' the lamp and the solid angle subtended by it. The time that the hole 'sees' the lamp is given by:

$$\text{Time} = \frac{1}{\text{wheel frequency}} \cdot \frac{\text{hole area}}{\text{annulus area at hole distance}} = \frac{1}{36\ \text{Hz}} \cdot \frac{0.5\ \text{mm}}{4 \cdot 4\ \text{cm}} = 86.6\ \mu\text{s}\ .$$

In addition, the solid angle subtended by the pinhole is given by:

$$\text{Solid Angle} = \frac{\text{hole area}}{\text{sphere surface area (lamp to pinhole)}} = \frac{(0.5\ \text{mm})^{2}}{4 \cdot (70.5\ \text{cm})^{2}} = 1.26 \cdot 10^{-7}\ .$$

Therefore, the lamp radiation characteristic curve, provided by the manufacturer must be multiplied by the time and the solid angle, in order to give the energy of the light as it comes out from the pinhole. The corrected curve is illustrated in Figure 4.4.

The filters used spanned a wavelength range from 350 to 650 nm. In this way, it was possible to establish what signal each tube gives at a given wavelength. The response of each tube is illustrated in Figures 4.5 and 4.6, where the signal has been corrected for the bandwidths and transmissions of the filters. The filters were purchased by Ealing and all of them were supplied with calibration curves of their transmission properties. The fit shown on each figure is a function which describes the data well. It allows for the loss of signal at low wavelengths due to the ultraviolet cut off of the glass in the system and the fall at high wavelengths due to the characteristics of the photocathodes.

Therefore, by combining Figures 4.4-4.6, it is possible to derive a relation between signal (in mV) and light energy in (Joules). For instance, the EMI 9789Q tube at a wavelength of 400 nm, gives 17.56 mV for 10^{-15} Joules, while the EMI 6097 tube at 550 nm gives 0.99 mV for 10^{-15} Joules. The next step was to determine the linearity of the response of the PMTs as the signal strength varied. From early tests the light flash signals expected from dust impacts on glass spanned the range of 10 to 500 mV. For that reason, the linearity was checked by illuminating the tubes with the same tungsten lamp for a signal range of 1 to 1000 mV. But, the amount of light seen during a pulse was controllable by use of neutral density filters. The tubes do respond linearly in that regime, and responses are illustrated in Figures 4.7 and 4.8.

There is a final correction to be made. The photomultiplier tubes were placed at a given distance away from the target in the Van de Graaff, since they were looking the events through

Figure 4.3: Mass - Velocity Iron Dust Relationships

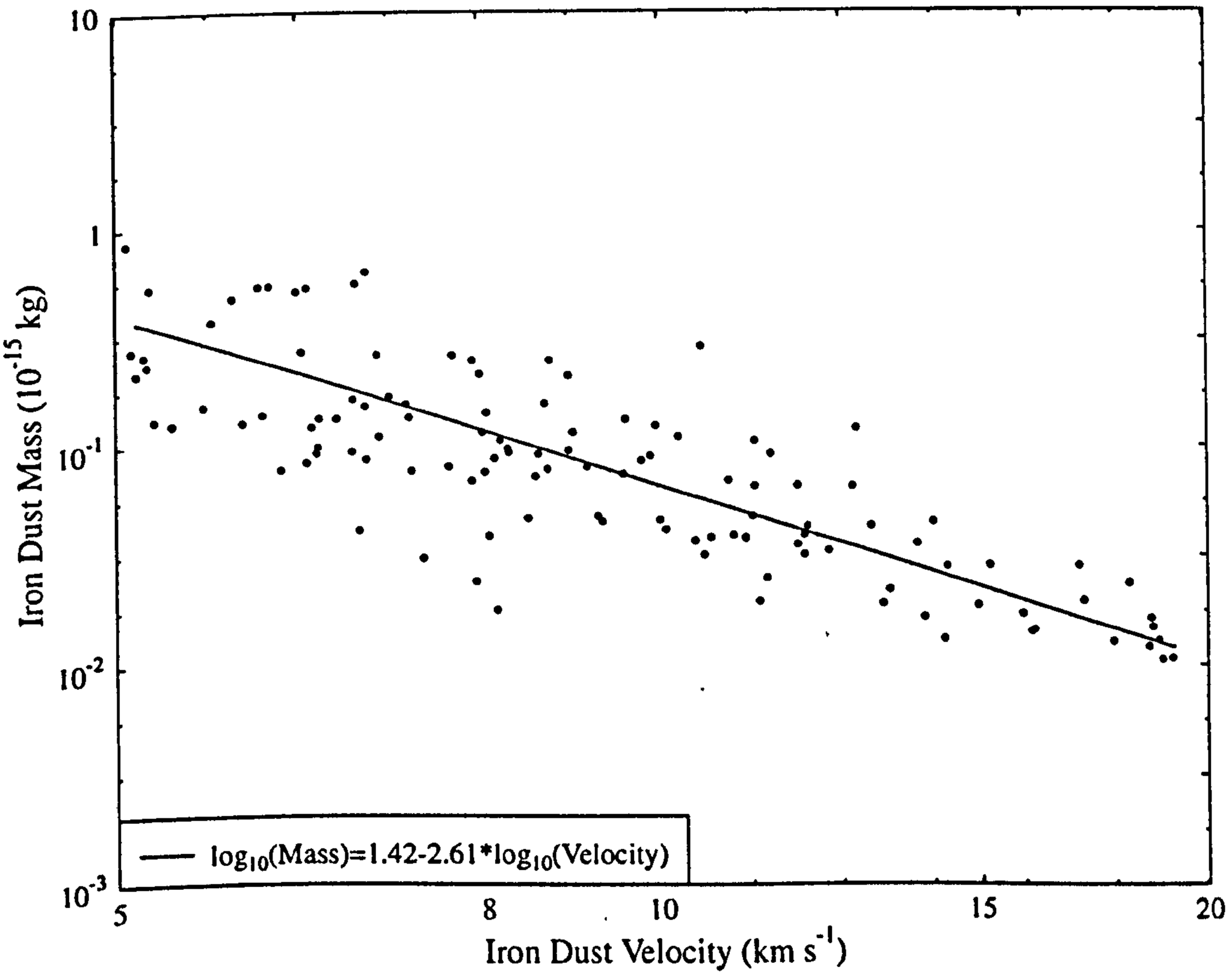

Figure 4.4: Energy of the Tungsten Lamp as arrived at the PM Tubes

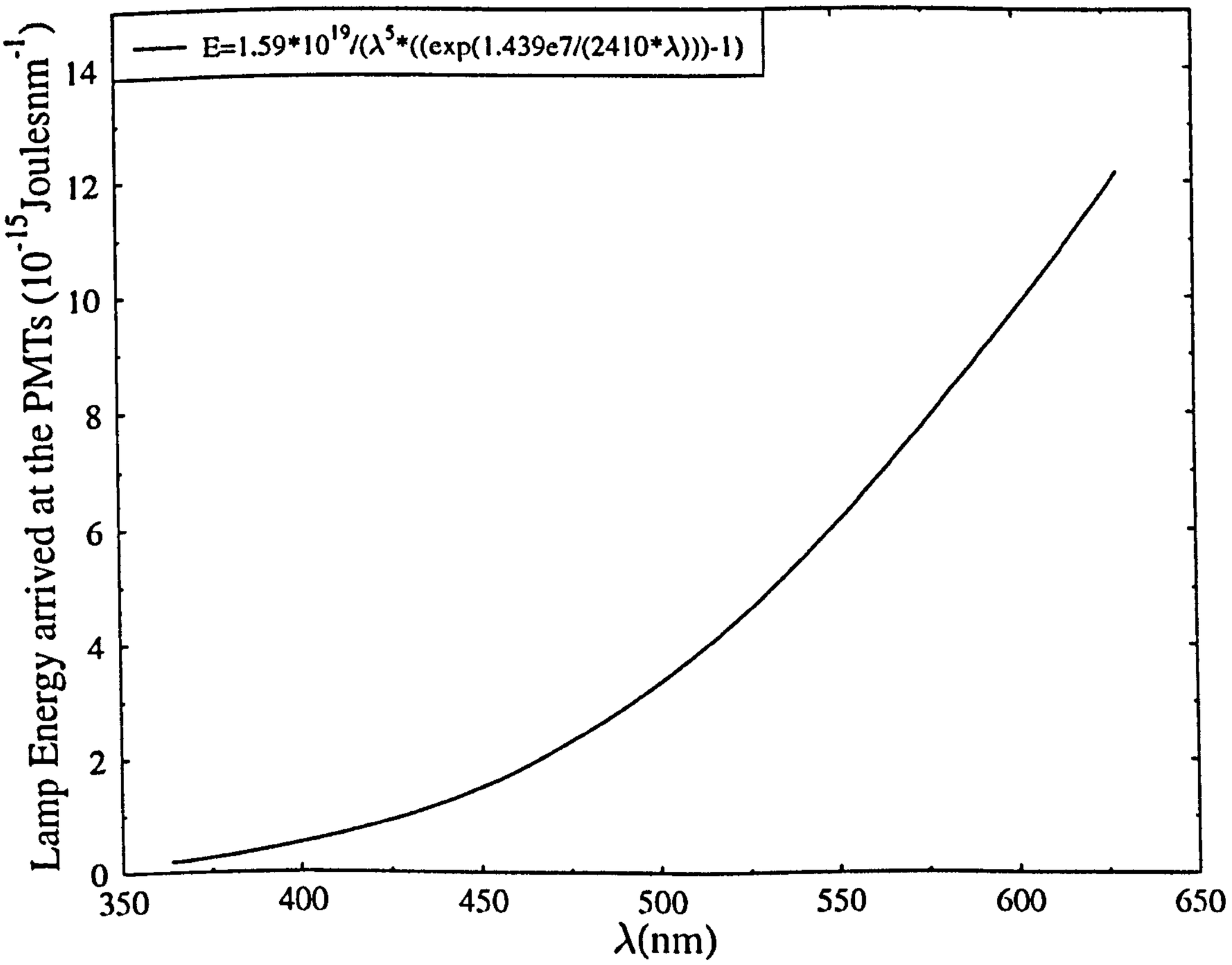

the viewports situated around the chamber. In this case, it was assumed that the field of view of the tubes was very large compared to the dimensions of the impact site.

The filters that have been used in the Van de Graaff experiments and placed in front of the photomultiplier tubes have already been described in section 4.2.1. Their peak wavelength corresponds to 400 and 550 nm, respectively.

To conclude, let us summarise all the necessary corrections in one equation. Each light flash signal must be divided with a correction factor C in order to give Joules/mV. This factor is made of

$$C = (\text{PMT solid angle}) \cdot (\text{filter tranmission and bandwidth}) \cdot (\text{PMT calibration}) .$$

$$(\text{PMT calibration}) = \frac{\dfrac{\text{oscilloscope signal}}{\text{filter transmission and bandwidth}}}{(\text{power curve}) \cdot (\text{pinhole time}) \cdot (\text{pinhole solid angle})} .$$

4.3 Experimental Results and Temperatures of the Radiating Material

In this section, the experimental results are presented together with the calculation of the light flash temperature from these results based on the assumption of black body radiation.

The data were taken for iron dust particles impacting a glass target at velocities from 5 - 20 km s^{-1}. The light flash was observed by means of two photomultipliers with filters at different wavelengths (400 and 550 nm) in front of the tubes. After all the corrections, discussed in section 4.2.3, the light energy for both wavelengths against iron dust impact velocity could be obtained. The energy was normalised for the mass of the projectiles. In this way, the dependence of the energy to the mass is eliminated. The results are illustrated in Figure 4.9. During data taking the accelerating voltage was uncertain to 4%. The particle velocity (charge) was, on average, accurate to 1% (4%) at low velocities, rising to 5% (10%) at 20 km s^{-1}. The uncertainty on the photomultiplier signal was less than 1% and was due to the background noise. The combined error is much smaller than the scatter in the data and therefore errors do not appear in the graph. The scatter observed on the data is large, i.e. at a fixed velocity the values of energy/mass span almost two orders of magnitude. However such a scatter is not abnormal in studies of hypervelocity dust impacts. Eichhorn[3)] and Burchell et al.[4)] observed a similar scatter in their data.

The data in Figure 4.9 are fitted in log-log space with an unweighted fit. In Figure 4.9 the best fits are shown. However, since the scatter in the data is quite significant, the fit is very

Figure 4.5: Calibration of the EMI 6097 PM Tube

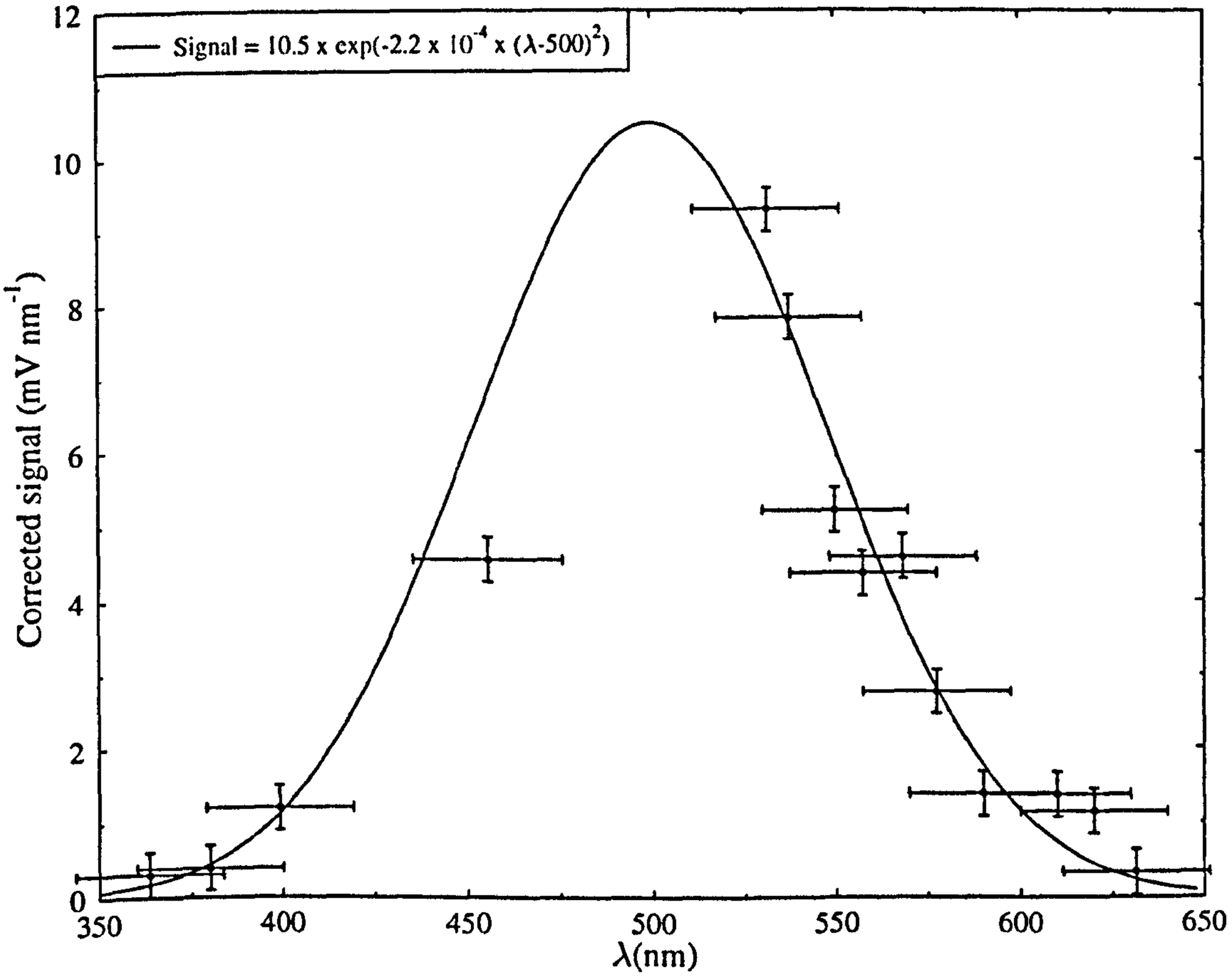

Figure 4.6: Calibration of the EMI 9789Q PM Tube

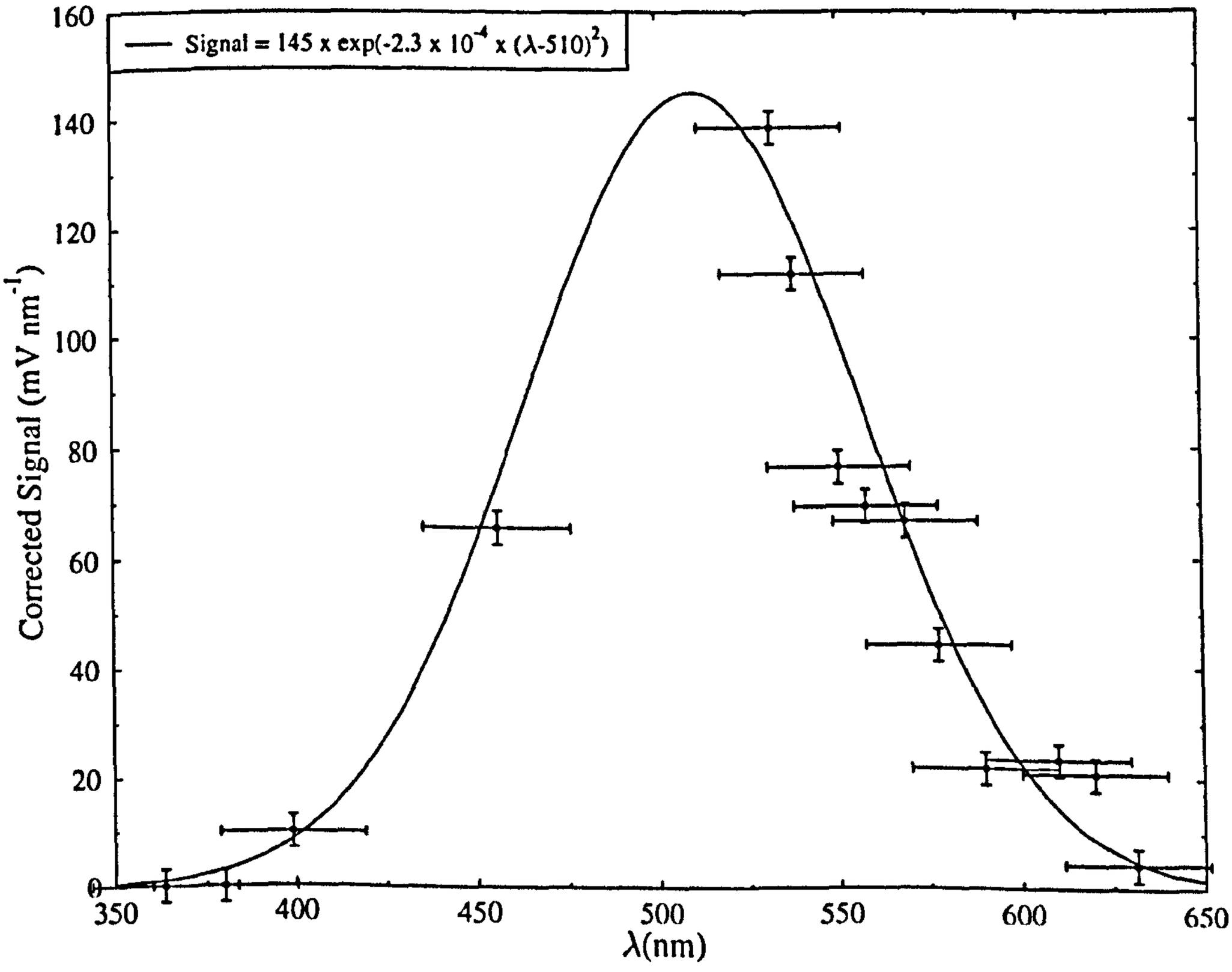

Figure 4.7: Response of pm 6097 to an attenuated light signal

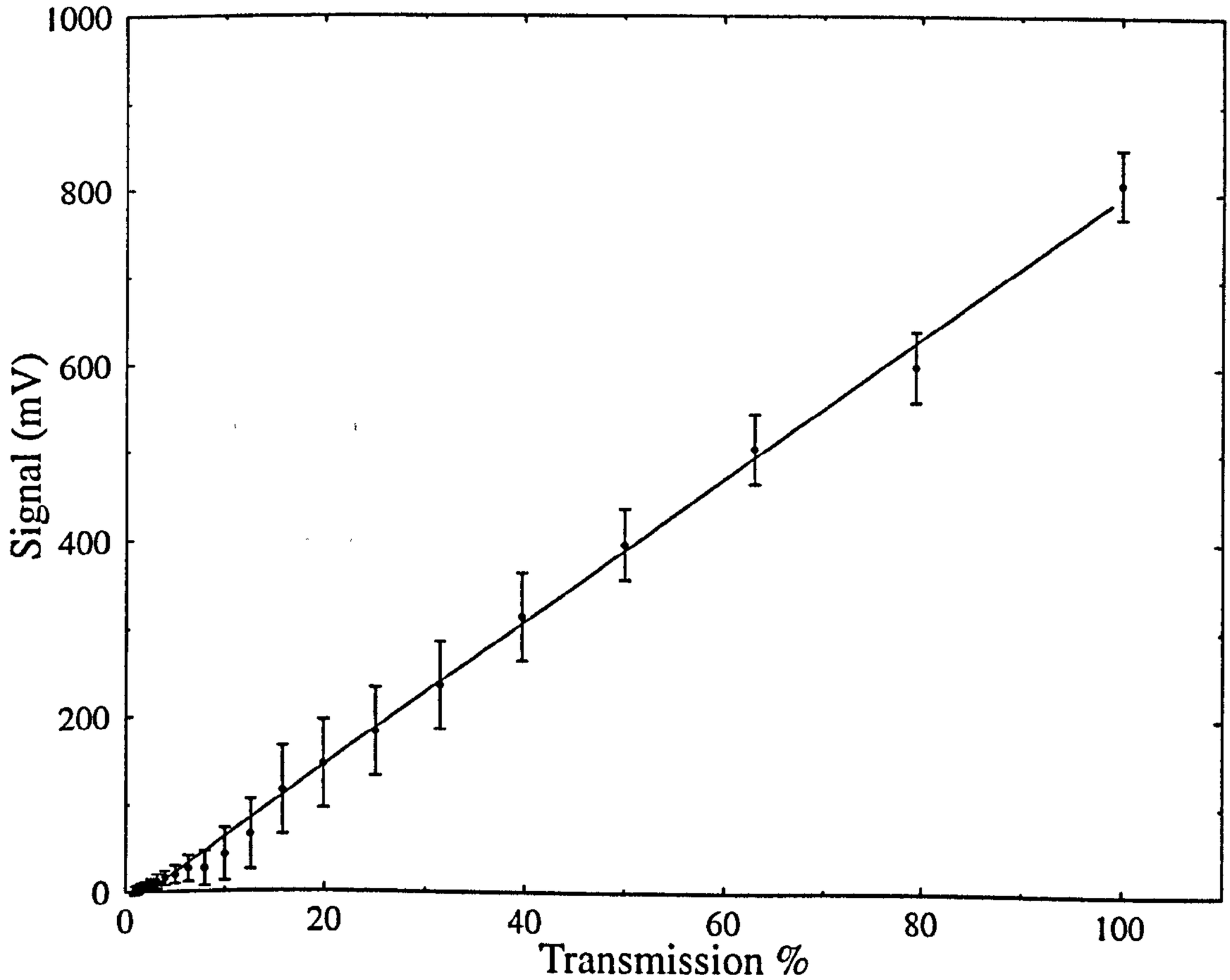

Figure 4.8: Response of pm 9789Q to an attenuated light signal

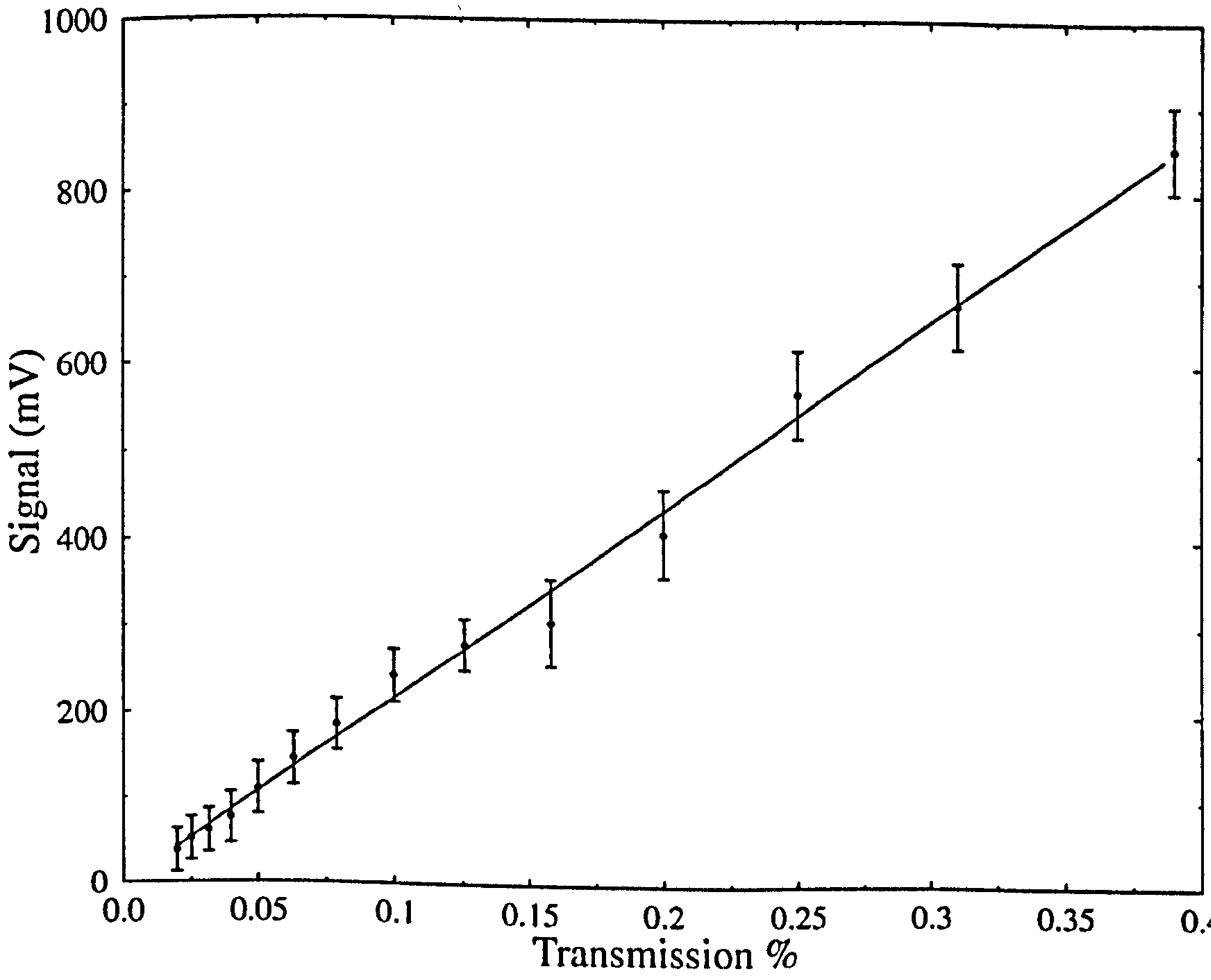

sensitive to the data. One could obtain an upper and lower bound for the fits by arbitrarily removing a few data (three at the most) points and repeating the fit. This was repeated several times leading to a range of fit parameters. Therefore, the relations of the specific energies at the two wavelengths against impact velocity are:

For λ=550 nm: $$E/m = 36.3\ (\pm 1.10)\ v^{2.34(\pm 0.04)} \quad (4.3.1)$$

For λ=400 nm: $$E/m = 3.80\ (\pm 1.00)\ v^{2.35(\pm 0.06)} \quad (4.3.2)$$

where E/m is the specific energy in J kg^{-1} nm^{-1} and v is the iron dust impact velocity in km s^{-1}. It becomes clear that both wavelengths have the same velocity dependence, within the data scatter. Taking the ratio of Equations 4.3.1 and 4.3.2, one can derive:

$$R = \frac{E_{550}}{E_{400}} = 10.6(\pm 3.5) \quad (4.3.3).$$

We next consider how the temperature may be estimated using the above results. We start by assuming black body radiation as a reasonable model for the measured light. This is in accordance with previous work by Eichhorn [4-7]. He measured the light energy of a single event using interference filters at 16 different wavelengths and found a good fit to a blackbody spectrum. Hence the light intensity emitted by a radiating black body of temperature T as a function of the wavelength λ is given by:

$$I(\lambda, T) = \frac{C_1}{\lambda^5 \left(e^{C_2/\lambda T} - 1 \right)} \quad (4.3.4)$$

where C_1 and C_2 are constants. However, since light energy was measured instead of intensity, Equation (4.3.4) must be integrated over the temperature between an initial temperature T_0 and final temperature to yield the total light energy E emitted at wavelength λ:

$$E(\lambda) = \int_{T_0}^{300K} I(\lambda, T)dT \quad (4.3.5).$$

Although temperature itself depends on time, according to Eichhorn (1976)[4] , the spectral distribution remains unaltered. More specifically, initially he assumed an exponential decrease of the temperature with time. Then, by varying the time constant by an order of magnitude the calculated spectral distribution was not affected.

We can thus combine Equations (4.3.4) and (4.3.5) for λ at 400 and 550 nm to obtain

Figure 4.9: Specific Light Energy for both Wavelenghts

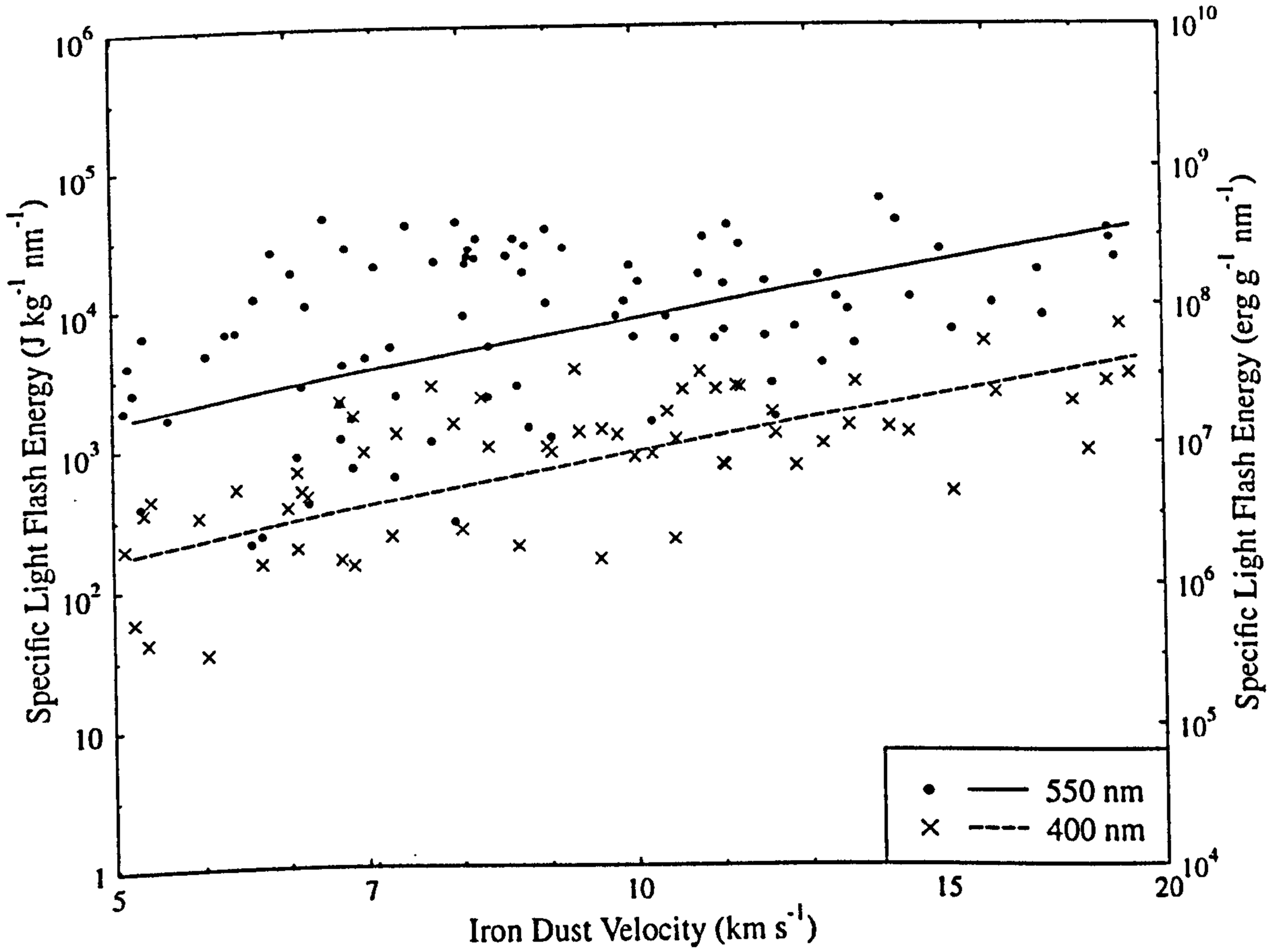

Figure 4.10: Expected Light Flash Temperature against Energies Ratio

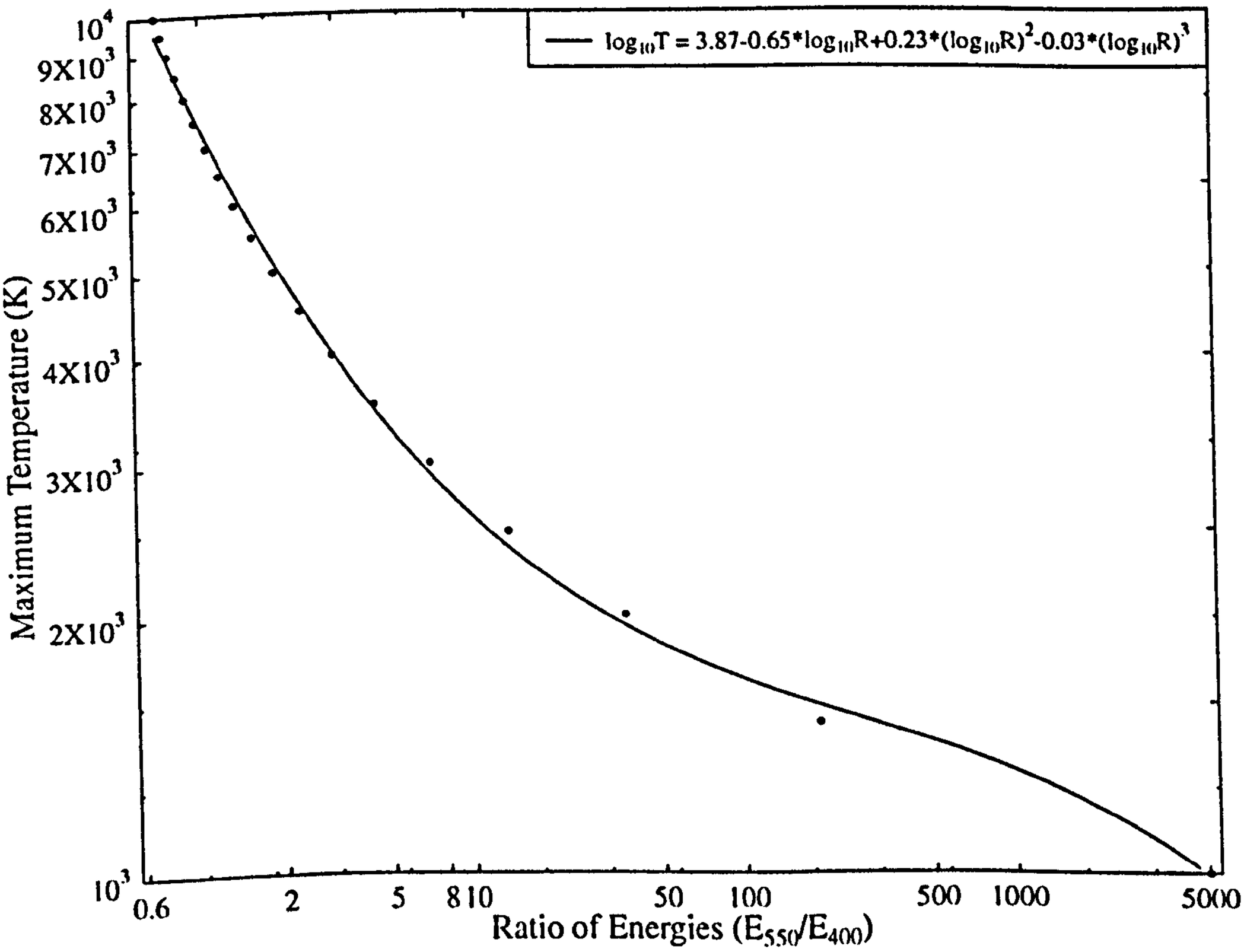

$$R = \frac{E_{550}}{E_{400}} = \left(\frac{400}{550}\right)^2 \cdot \frac{\int_{T_0}^{300K} \left(e^{C_2/550T} - 1\right)^{-1} dT}{\int_{T_0}^{300K} \left(e^{C_2/400T} - 1\right)^{-1} dT} \qquad (4.3.6)$$

It is, then, possible to calculate the ratio of the integrals for different values of T_0, using a standard software package, (Maple 3.3), and thus establish a relation between light flash temperature and the corresponding ratio of energies at two different wavelengths. This relation, is illustrated in Figure 4.10, where discrete solutions are found for various T_0 and are then fit by a third order polynomial in a log-log space:

$$\log_{10} T = 3.87 - 0.65 \log_{10} R + 0.22 (\log_{10} R)^2 - 0.03 (\log_{10} R)^3 \qquad (4.3.7)$$

Combining Equations 4.3.3 and 4.3.7, we finally obtain an estimation for the light flash temperature:

$$T_0 = 2638 \pm 263 \text{ K} \qquad (4.3.8)$$

Therefore, the temperature of the ejecta cloud is of the order of 2600 K (within the data scatter) and independent of impact velocity for the velocity range of 5-20 km s^{-1}. Although, this lack of dependence on velocity may seem to be rather strange, in the next section it will be argued that this is consistent with previous published work and that it may also be consistent with the current theories of hypervelocity impact dynamics.

4.4 Discussion of Results

In the previous section, the temperature of the ejecta cloud was found to be about 2600 K, independent of impact velocity. However, this is consistent with previous work. In the 70s Eichhorn[3,5-7] performed light flash experiments using the 2MV Van de Graaff dust accelerator facility of the Max-Planck-Institut fur Kernphysik at Heidelberg, Germany. He used a combination of different particles and targets at a velocity range from 5-20 km s^{-1}. Most of the materials were metals, except in one case where the target was duranglass (borosilicate glass). He measured light flash energy from impacts at 16 different wavelengths and presented results for temperatures at discrete velocities. The basic approach was similar to that presented here. However, the difference in the approach discussed in this chapter is that results have been obtained continuous in velocity. Eichhorn found that for iron projectiles the light energy for

different materials increases with increasing values of the melting temperature of the target. Although he did observe differences in light flash energies, the temperature of the flash remain constant with velocity or showed a small dependence. Figure 4.11 illustrates Eichhorn's results for flash temperatures of Duranglass when impacted by iron dust particles together with the upper and lower bound of the temperature results for the work presented in the previous section. The values found for temperature of the Duranglass by Eichhorn are very similar to those found here for soda-lime glass. That the values of Eichhorn are slightly higher may reflect the difference in glass composition (borosilicate vs. soda-lime glass). The important point is that for both materials, temperature seems to be independent of particle velocity.

Next, a comparison between theoretical predictions for glass temperatures given in section 3.5 and flash temperatures as estimated in section 4.3 is made. For that purpose, the measured temperature found (which lies between 2400 and 2900 K), is shown in Figure 4.12, along with the glass residual temperature calculated for different values of the Gruneisen coefficient using the model of section 3.5. In addition, Eichhorn's Duranglass are also displayed for comparison. In general, the results suggest that if the model is correct an appropriate choice for γ is in the range 0.90 to 2.00. At the lowest velocities when the temperature was measured (5 km s^{-1}) the measurements and the predictions may be beginning to diverge. The model predicts a sharp fall in temperature as the velocity falls from 5 to 2 km s^{-1}. If the temperature could be measured in this velocity range it would be a good test of the model. However it did not prove possible to obtain data at these lower velocities because the light flash signal as detected by the photomultiplier tube was too small and in the order of the background noise. Therefore more sensitive PM tubes and measurements with filters of higher wavelengths are needed, since red objects are cooler.

However, it should be remembered that the impact process itself may not be the only significant source of heating. Firstly, as already explained in section 3.4, for low velocities, ion generation and temperature increase can be caused by the electric field produced by the charged projectiles before impacting the target. In addition, for relatively, low velocities it is possible to have line emission, but a study of line emission for the glass was beyond the study of this research, although Eichhorn did not find any evidence of such emission.

In order to calculate the residual temperatures in Chapter 3, a value for the vaporisation temperature was assumed to be 3175 K. This choice was made because this is the vaporisation temperature of silicon dioxide, the most abundant constituent of glass. However, from section 4.3

Figure 4.11: Comparison of Flash Temperature Results

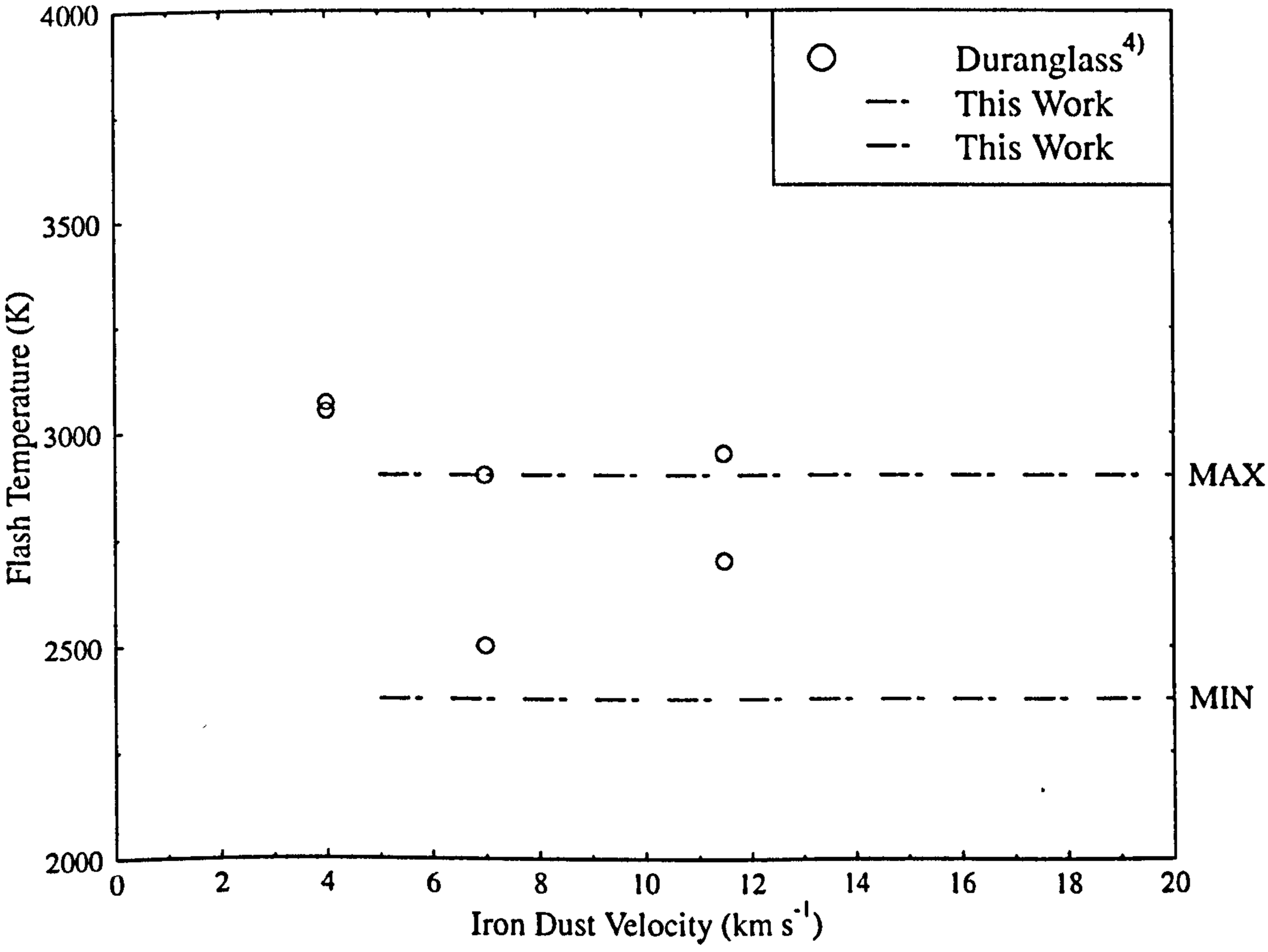

Figure 4.12:Glass Residual Temperature: Theory and Experiments

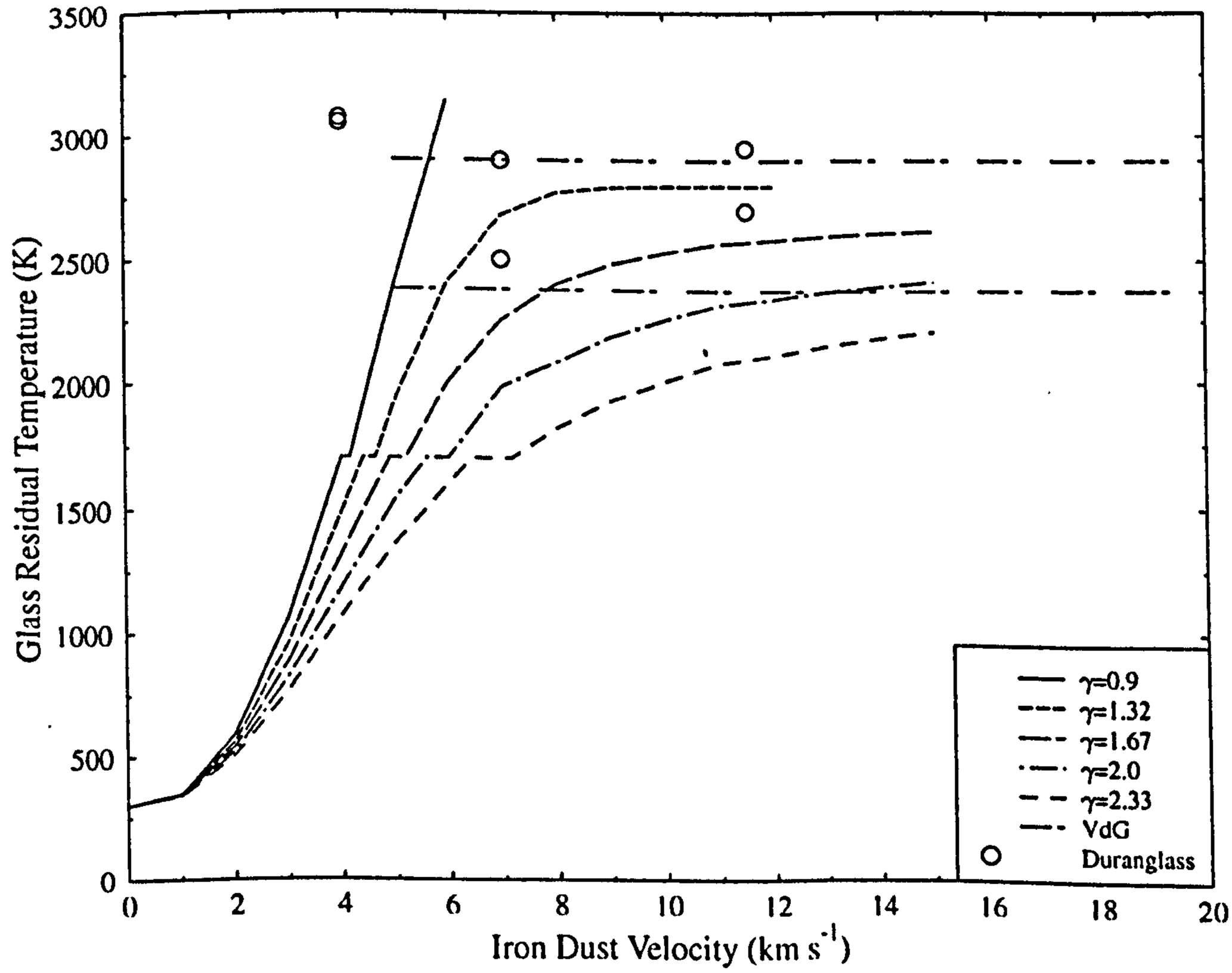

the temperature was found to lie between 2400 and 2900 K. That is, the upper bound is very close to the vaporisation temperature. If, in addition, the Gruneisen coefficient has a value between 0.9 and 2.0, then from the Figure 4.12, the velocity threshold for incipient vaporisation is about 5-15 km s^{-1}. From incipient to complete vaporisation, the residual temperature should be the same, since the system uses the heat deposited in it to go from the incipient to complete vaporisation. The same happens for the change of state associated with incipient to complete melting and can be seen in Figure 4.12, where this takes place between 3-5 km s^{-1} when the Gruneisen coefficient lays between 0.9 and 2.0. However, such calculations cannot be performed for incipient to complete vaporisation. The reason, as already explained in chapter 3, lays in the Equation of State of the material which is the Mie-Gruneisen. This EOS is derived from condensed matter principles and assumptions such as harmonic oscillations of atoms in a lattice and can be extended to liquids with care. Therefore, it is inappropriate to use it in the liquid-gas regime. Better EOS such as the Tillotson EOS may extend the calculation to the liquid-gas region. However, even this EOS is deficient if one extends to the total vaporisation regime. Although, calculations for complete vaporisation are difficult to perform, one can obtain some general features using the existing data. It can be argued that impact velocities of tens of km s^{-1} are required for total vaporisation. This can be explained both qualitatively and physically[7]. Firstly, the isentropic release curve becomes more and more asymptotic to ambient pressure as more and more energy is delivered in the initial shock state. Secondly, even though a large amount of energy is available from the shock process, the 'adiabatic' expansion of the vaporised material absorbs a significant amount of the available energy. It is, therefore, possible, that, the experimental value of the temperature is constant (for the velocity regime of 5 to 20 km s^{-1}) because the material is between the incipient and complete vaporisation stages, and that this temperature is, simply, the vaporisation temperature of glass. Hence, one can, also, argue that the vaporisation temperature of the soda-lime glass lays between 2400 and 2900 K.

However, there may be another explanation for the non-dependency of the temperature on impact velocity. The light flash observed is from the peak emission which for a fast impact, will be after the crater has expanded enough and hence it will be similar to a low velocity crater ejecta.

4.5 Conclusions

In this chapter, we described experiments performed with the 2MV Van de Graaff dust accelerator facility of UKC, in soda-lime glass targets using iron particles. The light flash from

the impact was observed by means of two photomulptiplier tubes at two different wavelengths. Relations for the specific energy at both wavelengths against impact velocity were established. Assuming black body radiation for the light flash, the temperature was estimated to lay between 2400 and 2900 K, independent of particle velocity. This is compatible with previous published data, and may be explained assuming that the temperature found is close to the vaporisation temperature of the material.

References

1. Medina D F , et al., (1996), 'Reconstruction of a Hypervelocity Impact Event in Space', Characteristics and Consequences of Orbital Debris and Natural Space Impactors, (Maclay T, and Allahdadi F A (Eds.), Proc. SPIE, **2813,** 137-147.
2. Green S F, et al., (1988), 'A 2MV Van de Graaff Accelerator for Cosmic Dust Impact Simulation', *J. British Interplanetary Soc.*, **41,** 393-396.
3. Eichhorn G, (1976), 'Analysis of the Hypervelocity Impact Process from Impact Flash Measurements', *Planet. Space Sci.*, **24,** 771-781.
4. Burchell M J et al, (1996), 'Light Flash and Ionisation from Hypervelocity Impacts on Ices', *Icarus*, **122,** pp 359-365.
5. Eichhorn G, (1975), 'Measurements of the Light Flash Produced by High Velocity Particle Impact', *Planet. Space Sci.*, **23,** 1519-1525.
6. Eichhorn G, (1978), 'Heating and Vaporisation during Hypervelocity Particle Impact', *Planet. Space Sci.*, **26,** 463-467
7. Eichhorn G., (1978), 'Primary Velocity Dependence of Impact Ejecta Parameters', *Planet. Space Sci.*, **26,** 469-471
8. Anderson C E, et al., (1990), 'Debris Cloud Dynamics', *Int. J. Impact Engng,* **9,** 89-113

CHAPTER 5

Hydrocode Modelling

5.1 Introduction

In chapter 3 residual temperatures of ejecta during a hypervelocity impact were predicted from first principles, while in chapter 4 experimental data of light flash from ejecta were presented. However, the theoretical predictions were one dimensional (no particle size could be accounted for; responsible for strain rate effects), while the Van de Graaff dust particle accelerator used for the experiments was restricted to a single projectile density (Iron) and was not able to accelerate heavy particles to high velocities.

However, hydrocodes (already explained in section 2.5) may give the flexibility and availability of different densities, sizes and velocities regime we require for a fuller understanding of the phenomena. But in order to have faith in the temperature data that are produced, an accurate model for the description of the soda-lime glass is needed. Since we are dealing with high impact velocities and hence higher pressures and temperatures, phase change upon release will take place. Thus an Equation of State (EOS) which accounts for such changes must be used. As it has been discussed in chapter 2, the most suitable, currently available EOS is the Tillotson EOS. However, no parameters are available for soda-lime glass. Thus the second best EOS was used, the Mie-Gruneisen, since it gives the same results as the Tillotson up to the point of incipient vaporisation and all necessary parameters can be found. In the case of a yield strength, the Mohr-Coulomb has been used, already discussed in chapter 2. More information for

the parameters used will be given in a later section. Since the model was developed from 'scratch' without previous verification of its validity, it was necessary to validate it against experimental data of hypervelocity impact on soda-lime glass crater dimensions being obtained by E A Taylor[1,2] using the two stage Light Gas Gun (LGG) facility of the University of Kent at Canterbury.

Results for crater dimensions using this hydrocode model (from now on we shall refer to it as the Glass Analogue Model (GAM)) carried out by the author will be presented and compared against the experimental work and hydrocode simulations using the Johnson-Holmquist model (JH), already discussed in chapter 2, both carried out by EA Taylor. Future improvement of the J-H model will also be presented. A theoretical section which describes how temperature is calculated in AUTODYN™ [3], is, also, presented and compared against equations derived in chapters 2 and 3. Finally, we assess the possibility of estimating ejecta temperatures using AUTODYN and some of the problems that arise.

5.2 The AUTODYN™ Hydrocode

5.2.1 Introduction

Before presenting the models and the data a brief description of the hydrocode used, AUTODYN™ [4], must be given. AUTODYN™ is a software for non-linear dynamics which was firstly released by Century Dynamics Inc. in 1986 with the introduction of AUTODYN 2D. In 1991, AUTODYN 3D, the three-dimensional analogue to AUTODYN 2D was introduced. Both AUTODYN programs are general purpose engineering software packages which use finite difference, finite volume, and finite element techniques, as described in section 2.6, to solve a wide variety of non-linear problems in solid, fluid and gas dynamics. Some applications of AUTODYN include impact and penetration, armour and anti-armour systems, kinetic energy and chemical energy devices, gas and dust explosions etc.

As well as the two common Eulerian and Langrangian processors, described already, AUTODYN™, also, contains the ALE (Arbitrary Langrange Euler) and the latest one, the SPH (Smooth Particle Hydrodynamics)[5] . In this chapter, ALE is ignored since it is an extension of the Langrangian scheme.

5.2.2 Smooth Particle Hydrodynamics (SPH)

SPH is a gridless technique for solving computational continuum dynamics problems and has several potential advantages over the grid based Langrange and Euler processors. Firstly, it does not require a numerical grid therefore it does not suffer from grid tangling problems or need erosion algorithms. In addition, SPH is a Langrangian technique, hence it has all the advantages of a Langrangian technique like efficient tracking of material deformation and history dependent behaviour.

However, the SPH algorithms are still a relatively new technology and are still being evolved. Although the SPH technique is very promising, it is not as robust as the existing Eulerian and Langrangian techniques. Under certain conditions, the SPH can become unstable. Describing the reasons of such instabilities is beyond the scope of this brief description. However, some of these instabilities have the consequence of violating the law of conservation of energy! Although, in every technique, an error of 5% is expected due to numerical errors and/or erosion algorithms, SPH produces energy losses of about 50%, therefore making the end result dubious, and residual temperatures impossible to predict.

5.2.3 Erosion Algorithms

Under certain circumstances in a Langrangian calculation some cells may be severely distorted. This may occur at the interface of target-projectile material in a hypervelocity impact problem. This may cause, for example, extremely small time steps and, in general, impair the progress of the calculation. To remedy this problem, special algorithms have been devised which remove such Langrangian cells from the calculation if a pre-defined strain exceeds a specified limit. When a cell is removed from the calculation the cell mass can either be discarded or distributed to the corner nodes of the cell. If the mass is retained, conservation of inertia and spatial discontinuity of inertia are maintained. However the compressive strength and internal energy of the material within the cell are lost whether or not the mass is retained.

This procedure is known as erosion. However, it is important to realise that it is *not* a physical phenomenon, but a pure computational trick to remedy the problems arisen by heavily distorted cells. Reference 6 explains the effect of the erosion values on the final crater dimensions in a hypervelocity impact problem.

5.2.4 AUTODYN Set up

AUTODYN has one of the most advanced and user friendly pre-processors, making the set up of a given simulation quite easy to do. Possibly the most difficult problem is to define and generate the computational mesh or grid. The space of both target and projectile have to be divided into very small cells so that the integration of the differential equations becomes discrete. Thus the smaller the cells one has the more accurate the result will be. However, as more cells are introduced, the calculation starts to become slow. For instance, in AUTODYN-2D, if one has a target of 100 by 100 nodes and a projectile of 41 by 21, in a Langrangian grid using axial symmetry, at least four days are needed on a P166 PC. Therefore one has to either have an powerful computer (such as a CRAY) or choose the grid such that the result will be accurate enough without the expense of computational time. To understand the above, think of a given impact problem. Suppose that a 1mm spherical projectile impacting a 10 cm by 10 cm target is simulated. The target, of course, is supposed to be semi-infinite since, by the time the 'shock' wave arrives in the lateral surfaces, it will have decayed to an elastic one. One needs a lot of nodes to characterise the size of the target. However, since in our case we are only interested in the final crater sizes (~ few mm) only the first mm of the target need to be modelled. Therefore, one can easily model only half the size of the target, that is the first 5 cm. Sometimes, even smaller sizes can be modelled.

The second important step for the set up is the material model. AUTODYN, like many other hydrocodes includes a variety of different Equation of States and Strength models. In addition different material parameters exist for these models inside the hydrocode libraries. However, one must know the needs and requirements of a given problem and the limitations of a given model. Let us give an example. In a case of a hypervelocity impact at 10 km s^{-1}, extended phase changes are expected for both projectile and target. Therefore a linear EOS (an extension of the Hooke's law) is definitely inappropriate. However such simulations have been taken place in the past [7]. For an impact at 10 km s^{-1}, strictly speaking, only the Tillotson EOS is appropriate. Of course, due to the lack of Tillotson parameters for many materials, one can use the shock EOS realising that it will give relatively sufficient results up to the point of incipient vaporisation. Therefore, it is not unwise to say that hydrocodes are only as good as their users. S B Segletes [8,9] gives an excellent account for some of the problems that may arise due to inappropriate use of material models.

Other important steps for the set up include symmetry, cut-off values, subgrids interaction, detonation points etc. Therefore, it becomes apparent that setting up a given problem in a right way is a rather formidable task and care must be taken when one analyses the end results.

5.3 Material Modelling

In chapter 2 we, generally, described both the EOS and Strength Models which are more appropriate for hydrocode modelling of soda-lime glass. There are the Mie-Gruneisen forms of EOS, and the Mohr-Coulomb and Johnson-Holmquist Strength Models.

In chapter 3, we showed how to calculate residual temperatures from first principles using basic thermodynamics and the impedance match method. In order to do so a linear shock - particle velocity relation was required. That is why, we fit the Hugoniot curve of the Johnson-Holmquist model[10] to a shock - particle velocity one. The fit is illustrated in Fig. 3.3. However, if any comparison is to be attempted between theoretical predictions and hydrocode results for residual temperatures, consistency on the material EOS is tantamount. That is why, the same Hugoniot curve was used. The value for the Gruneisen parameter was 1.32.

In addition, a Strength Model had to be chosen for the hydrocode simulations. Since the Johnson-Holmquist model was not available in AUTODYN at that moment, the Mohr-Coulomb was chosen. As we have, already, explained in chapter 2, four points on the yield stress-pressure are required. They were taken by the J-H model paper and they correspond to the maximum tensile hydrostatic pressure and calibration data from biaxial tests.

Finally, for simulating onset of failure, the principal stress directional failure was used. Two values were required; maximum tensile failure stress and maximum shear stress. Failure is initiated if the maximum tensile principal stress, or the maximum shear stress, exceed their specified limits. The first value was the tensile strength of the glass used by ESI[11] to simulate space debris and micrometeoroid impacts on the Columbus-viewport glass panes, while the second value was calculated as the product of the shear modulus and the maximum plastic strain the same material can withstand. The parameters used for the Glass Analogue Model (GAM) are presented in table 5.1.

However, as the testing of the GAM was continuing, E A Taylor (in collaboration with Century Dynamics Ltd.) was implementing the original Johnson-Holmquist in AUTODYN-2D[1].

Therefore, a second glass model was available for testing and comparison. In the following section we shall present and compare data for crater dimensions using both models and against experimental data. For the remaining of this section the GAM and J-H models will be, directly compared, and the need for further possible improvements of the latter model will be discussed.

Table 5.1: The GAM Parameters

EQUATION OF STATE	
ρ (g cm^{-3})	2.23
c_0 (km s^{-1})	3.3
S	1.5
Γ	1.32
STRENGTH MODEL	
G (GPa)	27.9
Y_1 (GPa)	0
P_1 (GPa)	-0.15
Y_2 (GPa)	0.42
P_2 (GPa)	0.08
Y_3 (GPa)	0.58
P_3 (GPa)	0.11
Y_4 (GPa)	0.62
P_4 (GPa)	0.12
FAILURE MODEL	
Tensile Stress (GPa)	0.21
Shear Stress (GPa)	1.395

Figure 5.1: GAM & and J-H Model at different strain rates

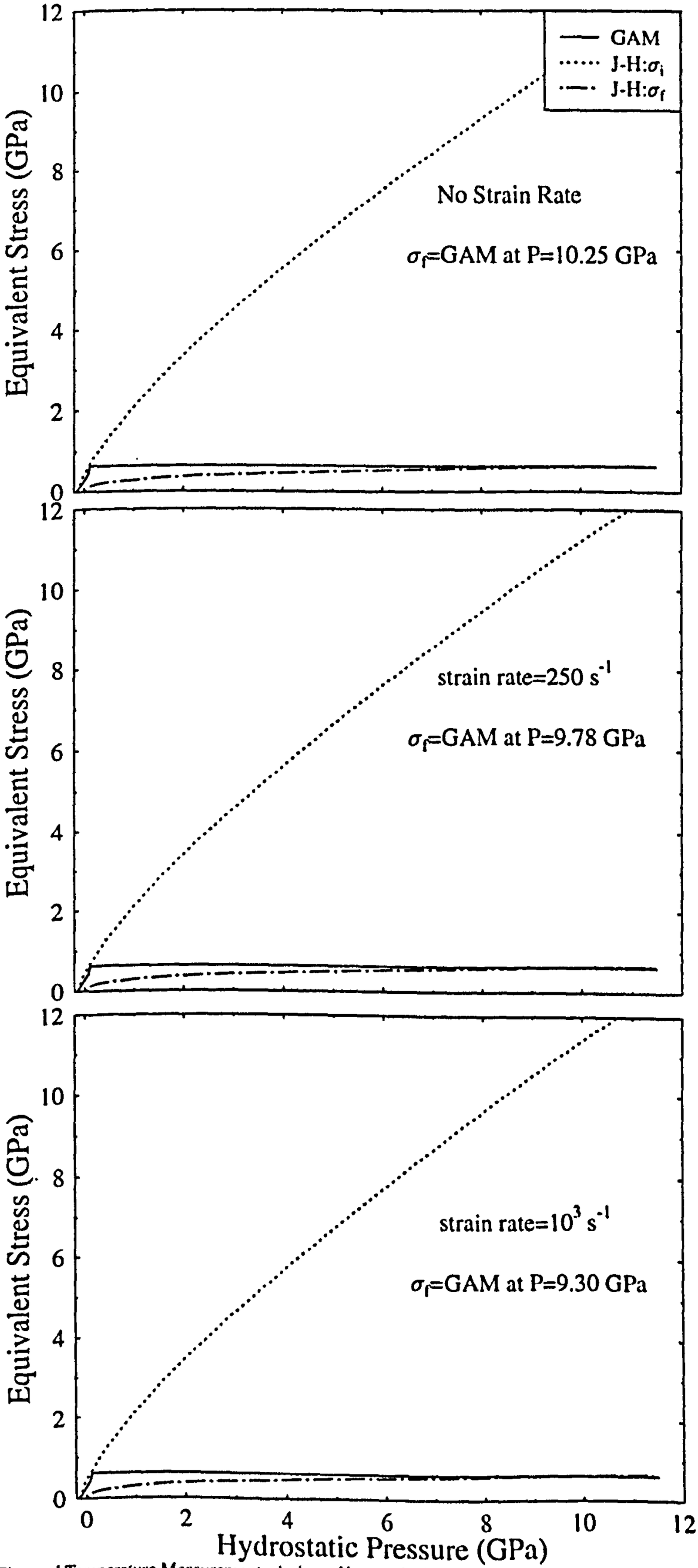

Figure 5.2: The Johnson-Holmquist Strength Model

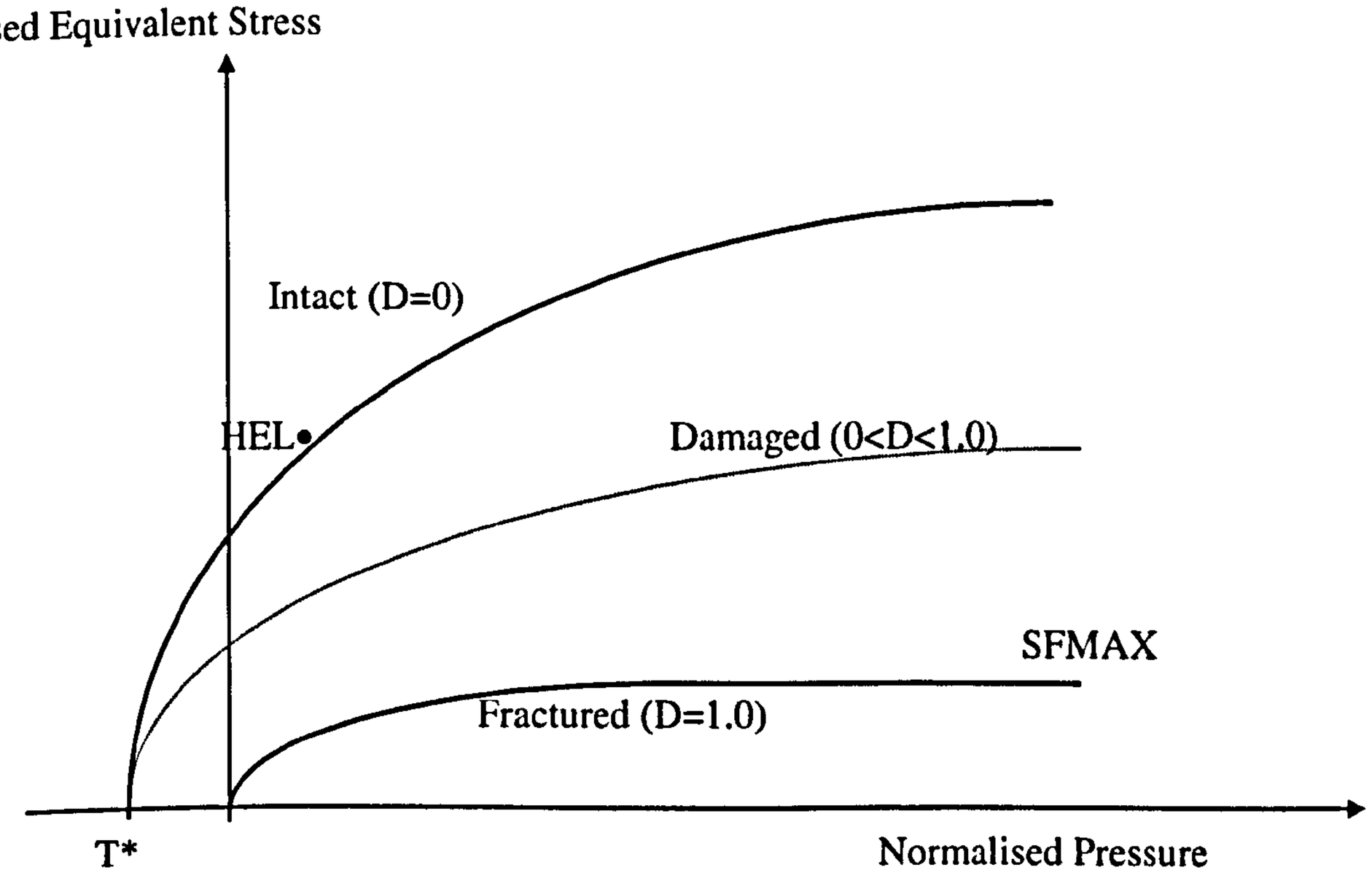

*Figure 5.3:*The Johnson-Holmquist EOS with the Bulking Pressure

$$P = K1 \cdot \mu + K2 \cdot \mu^2 + K3 \cdot \mu^3 + \Delta P.$$

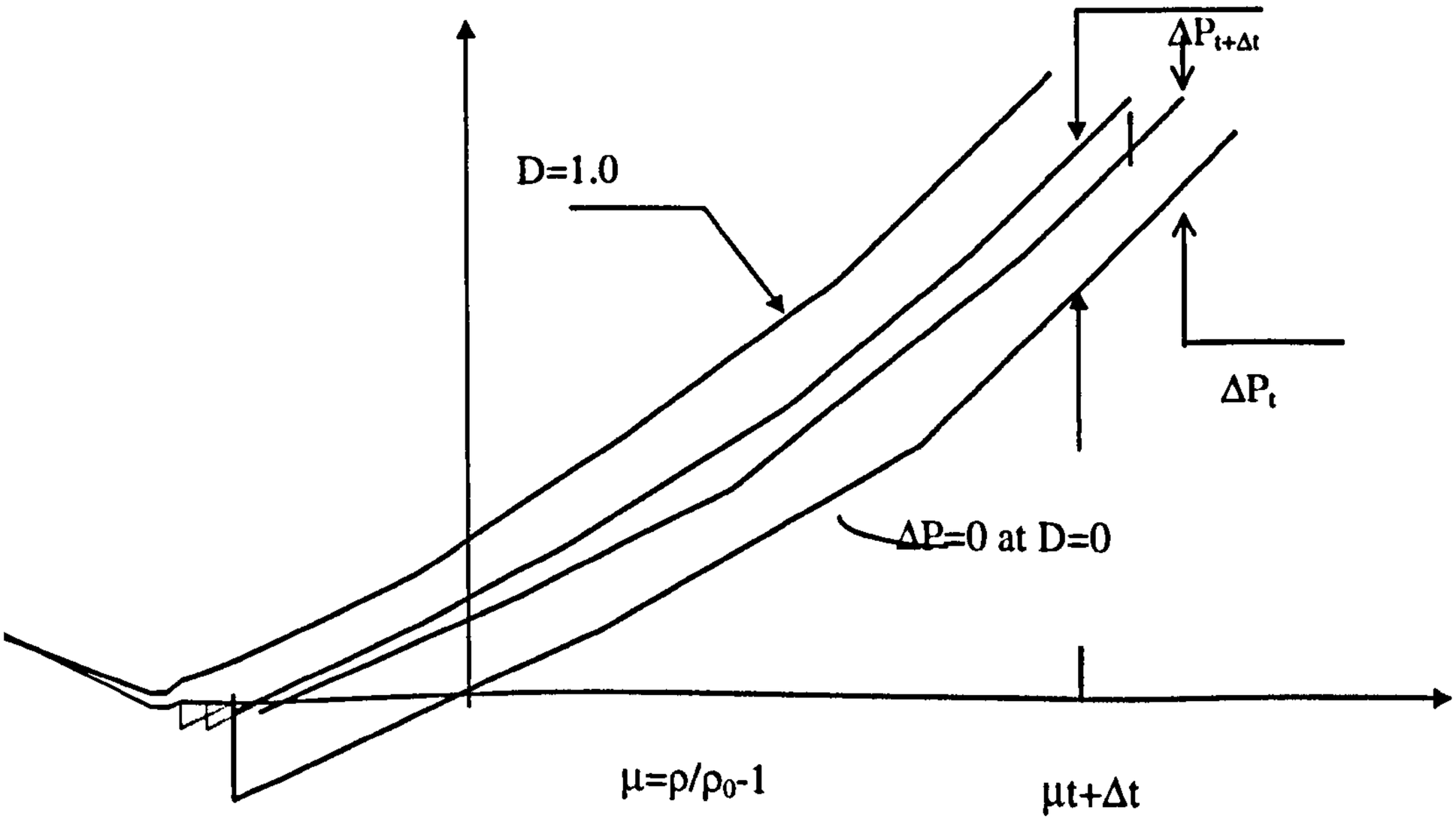

Figure 5.4: A closer look at the J-H bulking term

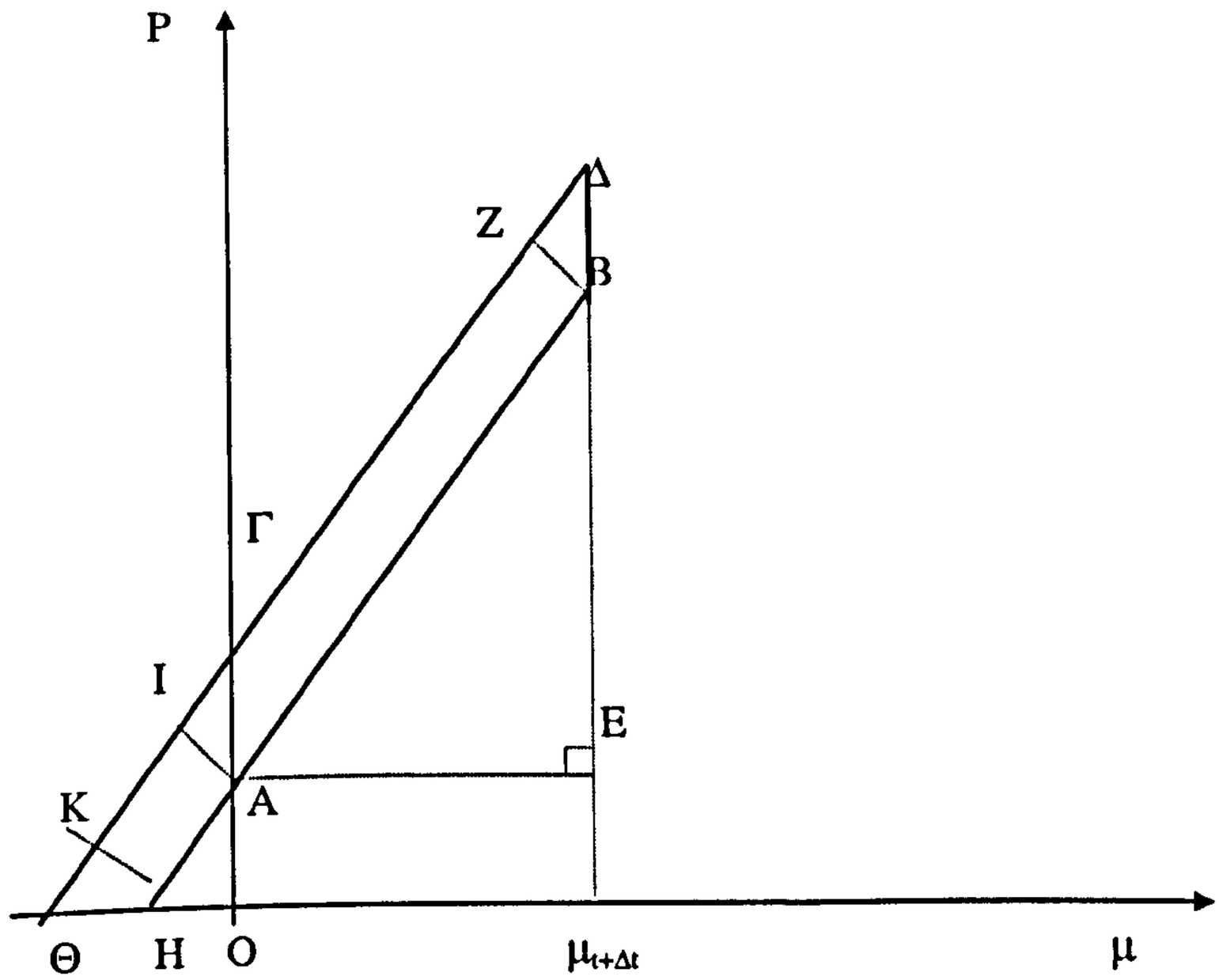

(angles: KΘH=IAΓ=BAE=ZBΔ=α)

Table 5.2: The J-H model parameters

EQ. OF STATE		STR. MODEL				FAIL. MODEL	
$\rho_0(g/cm^3)$	2.53	σ_{HEL}(GPa)	4.54	B	0.088	D_1	0.053
K_1(GPa)	45.4	P_{HEL}(GPa)	2.92	M	0.35	D_2	0.85
K_2(GPa)	-138.0	HEL	5.95	C	0.003	SFMAX	0.50
K_3(GPa)	290	A	0.93	T(GPa)	0.15	-	-
-	-	N	0.77	G(GPa)	30.4	-	-

The equivalent stress in the J-H model is a function of intact and fracture strength, and as damage accumulates, will always lie between σ_i and σ_f. In table 5.2 the J-H model parameters are presented and in Figure 5.1 the intact and fracture strength are illustrated for different strain rates (0 s^{-1}, 250 s^{-1} and 10^5 s^{-1}, respectively). For comparison purposes, the strength model of the GAM is also illustrated. Hence, one can see that the GAM lies between near the fractured strength of the J-H model. However, there is a big difference between the two models. The GAM

model will always have a constant yield strength if the hydrostatic pressure exceeds 0.12 GPa. The J-H model, on the other hand, behaves differently. The yield strength will always be decreasing as a pressure increases, but in the same time it will decrease as damage accumulates. Therefore, the J-H model seems to be superior of the GAM.

The J-H model, as we have explained in chapter 2, does not account for energy effects, that is, it is assumed that the Gruneisen coefficient Γ is zero. However this is not the case for all brittle materials. For instance, Quartz has Γ=0.9, MgO has Γ=1.32 [12], concrete has a value of 0.3[13], while water ice has a value of 0.35[14]. In addition, the Gruneisen coefficient for Soda-Lime Glass is not well known and a variety of coefficients should be tried, especially when the impact pressure is high, so as to ensure that the simulations give the correct result. In addition, it is well known that glass can reach its liquidus relatively easily as temperature increases. This will, significantly affect its yield strength, especially for high impact velocities. For the rest of this section we present a possible two-fold way of improving the current J-H model.

The first suggestion involves the use of energy effects and the use of the Mie-Gruneisen Equation of State. Let us consider the general expression for the elastic internal energy of the shear and deviatoric stresses.

$$U = \sigma^2 / 6G \tag{5.3.1}$$

where σ is the equivalent plastic flow stress, given by the Von Mises criterion, and G is the shear modulus of elasticity. The incremental internal elastic energy will decrease due to the decrease of deviator stresses. Thus, the incremental energy loss is

$$\Delta U = U_{D(t)} - U_{D(t+\Delta t)}, \tag{5.3.2}$$

where $U_{D(t)}$ and $U_{D(t+\Delta t)}$ are computed from Eq. (2.4.3.14) using $Y_{(t+\Delta t)}$ for both energies.

However, this loss will be converted to potential hydrostatic energy due to the incremental bulking pressure. Fig. 5.3 shows the incremental bulking pressure with respect to the compression of the material.

To find the energy loss which is converted to hydrostatic energy, we need to find an approximate relation for this. Let us redraw Fig. 5.3 to 5.4. If we compare the two diagrams then:

$OA=\Delta P_t$, $A\Gamma=\Delta B=\Delta P_{t+\Delta t} - \Delta P_t$, $AE=\mu_{t+\Delta t}$.

The gain in hydrostatic energy due to bulking is, then, given by the sum of the areas (AΓΔBA) and (HΘΓAH).

- Area (AΓΔBA) is:

$$(ZB)\cdot(AB) = \cos\alpha\cdot(\Delta B)\cdot\frac{(AE)}{\cos\alpha} = (\Delta B)\cdot(AE) = (\Delta P_{t+\Delta t} - \Delta P_t)\cdot\mu_{t+\Delta t} \tag{5.3.3}$$

- Area (HΘΓAH) is the area of a trapezoid (=1/2h(a+b), where a and b are the parallel sides and h is the distance between them).

$$\therefore \quad (H\Theta\Gamma AH) = \frac{1}{2}\cdot(IA)\cdot[(HA)+(\Theta\Gamma)] = \frac{1}{2}\cdot\cos a\cdot(A\Gamma)\cdot\left[\frac{(OA)}{\sin a}+\frac{(O\Gamma)}{\sin a}\right] = \tag{5.3.4}$$

$$= \frac{1}{2}\cdot\cot a\cdot(A\Gamma)\cdot[(OA)+(O\Gamma)]$$

From the triangle HOA we have: $\tan\alpha=(OA)/(OH)$

$$\therefore \quad (H\Theta\Gamma AH) = \frac{1}{2}\cdot\frac{(OH)}{(OA)}\cdot(A\Gamma)\cdot[(OA)+(O\Gamma)] \tag{5.3.5}$$

Since $(OA) = \Delta P_{t+\Delta t}$ and $(A\Gamma) = \Delta P_{t+\Delta t} - \Delta P_t$

$$\therefore (H\Theta\Gamma AH) = \frac{1}{2}\cdot\frac{(OH)}{\Delta P_t}\cdot(\Delta P_{t+\Delta t}-\Delta P_t)\cdot(\Delta P_{t+\Delta t}+\Delta P_t) = \frac{(OH)}{2\Delta P_t}\cdot\left[(\Delta P_{t+\Delta t})^2-(\Delta P_t)^2\right]$$

(5.3.6)

From Equation (2.4.3.13) $P = K1\cdot\mu + K2\cdot\mu^2 + K3\cdot\mu^3 + \Delta P$. However, if we take μ to be very small, then

$$P \approx K1\mu + \Delta P \tag{5.3.7}$$

In the case of $\mu = (OH)$, P becomes zero. Thus $(OH) = \Delta P_t/K1$, taking the absolute value.

Hence Equation (5.3.6) takes the form:

$$(H\Theta\Gamma AH) = \frac{\left[(\Delta P_{t+\Delta t})^2-(\Delta P_t)^2\right]}{2K1} \tag{5.3.8}$$

But, the potential hydrostatic energy is the sum of the two areas. Thus, the energy conservation takes the form:

$$(\Delta P_{t+\Delta t}-\Delta P_t)\mu_{t+\Delta t} + \frac{\left[(\Delta P_{t+\Delta t})^2-(\Delta P_t)^2\right]}{2K1} = \beta\cdot\Delta U \tag{5.3.9}$$

where β is the fraction ($0\le\beta\le1$) of the elastic energy loss converted to potential hydrostatic energy. Solving the above equation for the updated ΔP gives:

$$\Delta P_{t+\Delta t} = -K1\cdot\mu_{t+\Delta t} + \sqrt{\left\{K1\cdot\mu_{t+\Delta t}+\Delta P_t\right\}^2 + 2\cdot\beta\cdot K1\cdot\Delta U} \tag{5.3.10}$$

Thus a closed form for the bulking pressure has been found. This form can be used in a program such as a hydrocode.

Suppose, now, that instead of Equation (2.4.3.13) we have

$$P_H = \frac{\rho_0 c_0^{\,2}\mu(1+\mu)}{[1-(s-1)\mu]^2} + \Delta P = \frac{\rho_0 c_0^{\,2}(\mu+\mu^2)}{1-2(s-1)\mu+(s-1)^2\mu^2} + \Delta P \qquad (5.3.11)$$

If we take μ to be very small, then, in the limit, the above Equation becomes:

$$\lim_{\mu\to 0}(P_H) = \frac{\rho_0 c_0^{\,2}\mu}{1-2(s-1)\mu} + \Delta P \qquad (5.3.12)$$

In the case of (OH), $\lim(P_H)$ is zero. Thus:

$$(OH) = \frac{\Delta P_t}{\rho_0 c_0^{\,2} - 2(s-1)\Delta P_t} \qquad (5.3.13)$$

taking the absolute value.

Substituting Equation (5.3.13) into Eq. (5.3.6) we get:

$$(H\Theta\Gamma AH) = \frac{\left[\left(\Delta P_{t+\Delta t}\right)^2 - \left(\Delta P_t\right)^2\right]}{2\left[\rho_0 c_0^{\,2} - 2(s-1)\Delta P_t\right]} \qquad (5.3.14)$$

Instead of Equation (5.3.9) we have

$$\left(\Delta P_{t+\Delta t} - \Delta P_t\right)\mu_{t+\Delta t} + \frac{\left[\left(\Delta P_{t+\Delta t}\right)^2 - \left(\Delta P_t\right)^2\right]}{2\left[\rho_0 c_0^{\,2} - 2(s-1)\Delta P_t\right]} = \beta\cdot\Delta U \qquad (5.3.15)$$

Solving for the updated ΔP we get:

$$\Delta P_{t+\Delta t} = -\left[\rho_0 c_0^{\,2} - 2(s-1)\Delta P_t\right]\cdot\mu_{t+\Delta t} + \sqrt{\left\{\left[\rho_0 c_0^{\,2} - 2(s-1)\Delta P_t\right]\cdot\mu_{t+\Delta t} + \Delta P_t\right\}^2 + 2\cdot\beta\cdot\left[\rho_0 c_0^{\,2} - 2(s-1)\Delta P_t\right]\cdot\Delta U} \qquad (5.3.16)$$

Therefore, Equation (5.3.10) can be substituted by Equation (5.3.16) to find the updated ΔP, if we want to use a different form for the Hugoniot curve.

Suppose, now, that energy effects are significant, that is, if we use the Mie-Gruneisen EOS then the Gruneisen constant has a non zero value. Then from Equation (2.3.3.22) we have:

$$P = P_H(V) + \frac{\gamma(V)}{V}\left[E - E_H(V)\right] \qquad (5.3.17)$$

However, in this case, $P_H(V)$ is given by Equation (5.3.11). If, in addition, we assume that the bulking pressure in independent of the internal energy then Equation (5.3.17) takes the form:

$$P = \left(\frac{\rho_0 c_0^2 \mu(1+\mu)}{\left[1-(s-1)\mu\right]^2} + \Delta P \right) + \frac{\gamma(V)}{V}\left[E - E_H(V)\right] \qquad (5.3.18)$$

Thus the dilation factor has been included in an energy dependent EOS. The reason for this inclusion is that during a hypervelocity impact process, the material may change phase upon release. Thus the change in internal energy plays a significant role.

Finally, it is known that during HVI thermal softening effects becomes significant and, thus, materials lose their strength. Thus we suggest that such an effect should be taken into account in the Johnson-Holmquist model.

In the case of the Johnson-Cook strength model, the thermal softening effect is modelled as a term in the yield strength given as (1- T_H^m) where T_H is the homologous temperature,

$$\text{i.e.} \quad T_H = \frac{T - T_{room}}{T_{melt} - T_{room}} \qquad (5.3.19)$$

We suggest a similar term to be placed in the equations for the normalised intact and fractured strength of the Johnson-Holmquist model. Thus if:

$$Y^* = Y_i^* - D \cdot (Y_i^* - Y_f^*) \qquad (5.3.20)$$

then

$$Y_i^* = A \cdot \left(P^* + P_{MIN}^*\right)^N \cdot \left(1 + C \cdot \ln\dot{\varepsilon}^*\right) \cdot \left(1 - T_H^Q\right) \qquad (5.3.21)$$

$$Y_f^* = B \cdot (P^*)^M \cdot (1 + C \cdot \ln\dot{\varepsilon}^*) \cdot \left(1 - T_H^Q\right) \le SFMAX \qquad (5.3.22)$$

(where we have replaced T* in the original formulation with P_{min}* , to avoid confusion with temperatures) and Q is a material parameter.

As well as showing how the JH model can be written in a form suitable for use in hydrocodes, two extensions have also been presented, which if implemented will take into account the energy dependence for phase changes and thermal softening of glass. Both are important in a hypervelocity impact process. However, in order to assess their suitability they have to be implemented in a hydrocode and tested against experimental results.

5.4 Temperatures Calculations in AUTODYN™

Since the main area of this research is to establish the residual temperatures of the ejecta cloud, it is important to explain how temperatures are calculated within AUTODYN™. We follow the same approach as in AUTODYN theory manual, but only the main result will be given. However, the results will be compared against results derived in section 2.3.3.6 and 3.2.

The change in temperature of a system is given by:

$$dT = \frac{dQ}{C_v} - \gamma(V)\rho_0 T dV + \frac{VS_\lambda d\theta_\lambda^p}{C_v} - \frac{qdV}{C_v} \tag{5.4.1}$$

with a Equation of State of the form

$$P = A(V) + \gamma(V)\rho_0 e \tag{5.4.2}$$

where T is the temperature , Q is the heat added to the system, C_v is the specific heat at constant volume, $\gamma(V)$ is the Gruneisen parameter, ρ_0 is the initial density, dV is the specific volume, S_λ ($\forall\ \lambda = 1,2,3$) are the deviator stresses, θ^p is the plastic strain deviator tensor and q is the artificial viscosity.

Suppose that the deviator stresses are zero (fluid) or negligible compared to the volumetric response (hypervelocity impact) and exclude the artificial viscosity. Then Equation 5.4.2 becomes:

$$dT = \frac{dQ}{C_v} - \frac{T\gamma(V)}{V_0} dV \tag{5.4.3}$$

Suppose, now, that we go from the initial state A (P_0, V_0, E_0) to the shock state B (P_H, V_H, E_H). Then the internal energy is given by the Hugoniot relations:

$$E_H = \tfrac{1}{2} P_H (V_0 - V_H) \tag{5.4.4}$$

where we assumed that the initial pressure and internal energy are negligible.

Therefore, the total differential of the internal energy is:

$$dE_H = \tfrac{1}{2}\left[(V_0 - V_H)dP_H - P_H dV_H\right] \tag{5.4.5}$$

However, from the first law of thermodynamics we have:

$$dQ = dE + PdV \tag{5.4.6}$$

Finally, from Equations 5.4.3-5.4.6 we derive:

$$\frac{dT_H}{dV_H} = -\frac{T_H\gamma(V)}{V_0} + \frac{1}{2C_v}\left[(V_0 - V_H)\frac{dP_H(V)}{dV} + P_H\right] \tag{5.4.7}$$

Equation (5.4.7) is the same as the Equation (2.3.3.34). Thus we shown that the equation derived to calculate shock temperatures is a special case of the temperature calculations in AUTODYN.

From Reference (15), the specific heats are related by :

$$C_P - C_V = \frac{TV\beta^2}{K} \tag{5.4.8}$$

where C_P is the specific heat capacity at constant pressure, β is the coefficient of volumetric expansion and K is the isothermal bulk modulus. The definitions for β and K are:

$$\beta = \frac{1}{V}\left(\frac{\partial V}{\partial T}\right)_P \tag{5.4.9}$$

$$K = -V\left(\frac{\partial P}{\partial V}\right)_T = \frac{1}{K} = -\frac{1}{V}\left(\frac{\partial V}{\partial P}\right)_T \tag{5.4.10}$$

We also know from Equation (3.3.11) that:

$$\gamma(V) = \frac{K\beta}{C_v} \tag{5.4.11}$$

From Equations (5.4.3), (5.4.6) and Equations (5.4.8)-(5.4.11) we derive

$$dE = C_p dT - PdV - \frac{T\beta}{\rho}\left(\frac{\beta}{K}dT - K\beta dV\right) \tag{5.4.12}$$

Suppose that the volume is a function of pressure and temperature. In differential form change in volume may be written:

$$dV = \left(\frac{\partial V}{\partial T}\right)_P dT + \left(\frac{\partial V}{\partial P}\right)_T dP \tag{5.4.13}$$

From Equations (5.4.9)-(5.4.10) and (5.4.13) we derive:

$$\frac{\beta}{K}dT - K\beta dV = dP \tag{5.4.14}$$

From Equation (5.4.12) and (5.4.14) we, finally, obtain:

$$dE = C_p dT - PdV - \frac{T\beta}{\rho}dP \tag{5.4.15}$$

This is the Equation (3.1.6) used to calculate residual temperatures of the ejecta cloud in chapter 3. Therefore, the theory behind temperature calculations in AUTODYN is equivalent to the method used in chapter 2.

Figure 5..5: Glass Impact Morphology

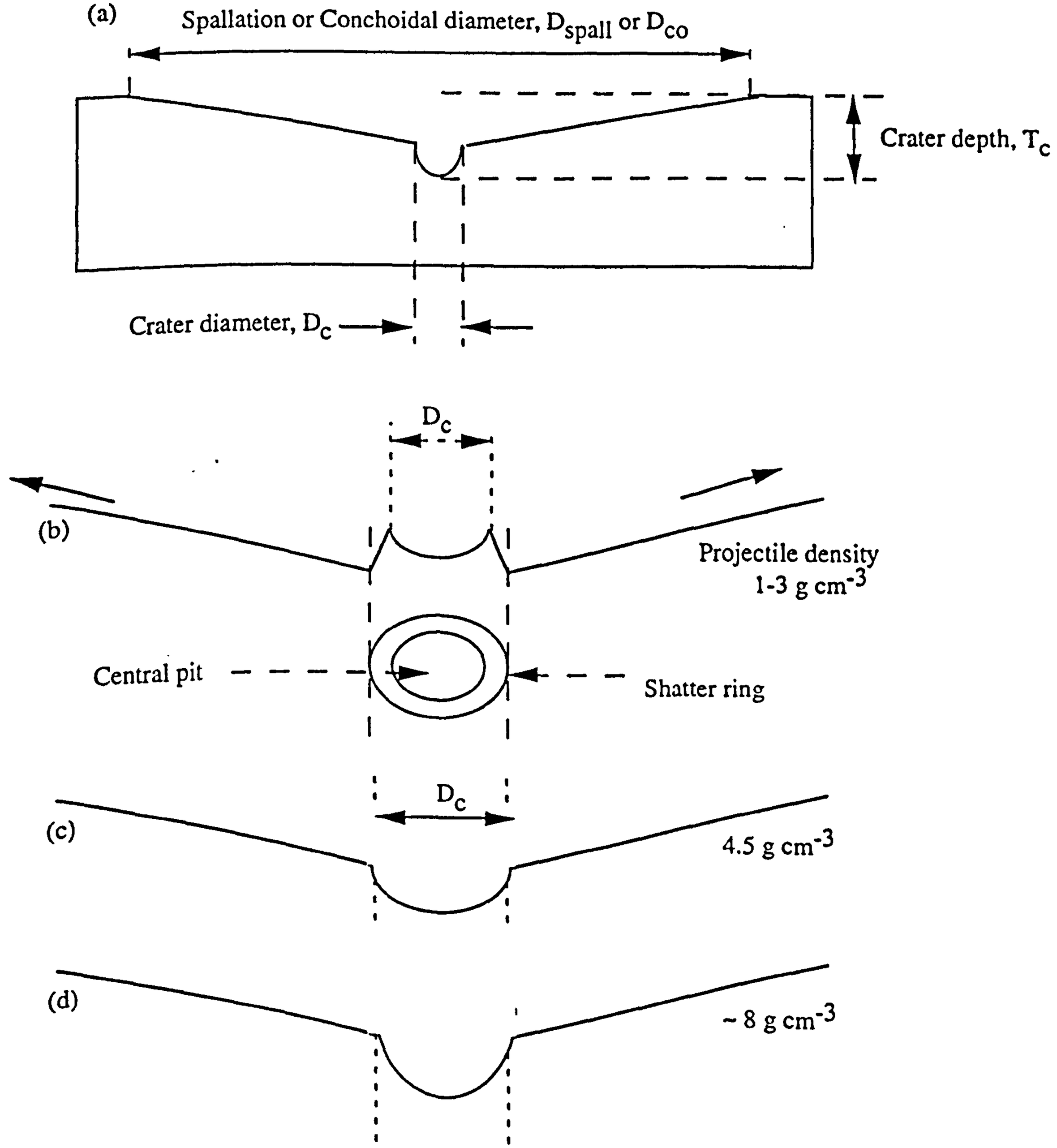

5.5 Comparison of Crater Dimensions against Experimental Results using the GAM and J-H Model

As mentioned in the introduction of this chapter, the Glass Analogue Model can be validated against experimental results onto 25 mm x 150 mm x 0.5 mm disk shaped soda-lime glass targets and hydrocode simulations using the J-H model both performed by EA Taylor[1,2]. The glass impact morphology is illustrated in Fig. 5.5[1]. One can see the central pit together with the spallation region and sub-surface fracture. In this section, only the central pit depth and diameter are compared, since both hydrocode models fail to predict any spallation region. For more information about the glass crater morphology under hypervelocity impact one can refer to EA Taylor and JAM McDonnell (1996)[16].

In the experimental program carried out by EA Taylor[1,2] different projectile densities (range 1.15-8.47 g/cm^3) and sizes (0.8-2.0 mm) were used at an almost constant velocity (5.06±0.27 km/s). In hydrocode modelling the same material densities and sizes should be modelled. However, due to lack of material parameters availability in AUTODYN, only some of the materials were modelled. These are summarised in table 5.3. Detail descriptions of the models are given in chapter 2.

Soda-Lime Glass Crater depth and diameters are illustrated in Figures 5.6 through 5.8. Figure 5.6 includes crater dimensions for the low density projectiles (Cellulose Acetate, Nylon and Aluminium), while Figure 5.7 includes the intermediate density projectiles (Titanium and Ruby) and Figure 5.8 the high density projectiles (Stainless Steel 304, 316 and 420).

Table 5.3: Projectile Materials used in Simulations

MATERIAL	EQUATION OF STATE	STRENGTH MODEL
Aluminium 2024	Tillotson	Steinberg-Guinan
Nylon	Shock	Von Mises
Titanium	Tillotson	Steinberg-Guinan
Stainless Steel 304	Shock	Steinberg-Guinan

It is clear that Glass Analogue Model predictions compare well against experimental data, although it, generally, , underpredicts experiments (10% for low projectile diameters up to 20% for higher diameters). By contrast, the results from the J-H model are, typically, less accurate than the GAM results overpredicting most experimental data. However, this comparison is limited by the present lack of results for the J-H model and more simulations are being, currently, performed by EA Taylor to confirm this.

The validation of the hydrocode model has been carried out against experimentally produced data. However, what happens when no such data exist, like, for instance, for impact velocities greater than 5 km s^{-1}? In this case, one can test hydrocodes against power-law damage equations which are frequently used to predict the damage sustained in the space environment. The two equations, currently, used to predict the depth of a glass crater under hypervelocity impact are

McHugh-Richardson[17] :
$$T_c = 0.64 d_p^{1.2} \rho_p^{0.5} v_p^{0.67} \quad (5.5.1)$$

and

Cour-Palais[18] :
$$T_c = 0.53 d_p^{1.06} \rho_p^{0.5} v_p^{0.67} \quad (5.5.2)$$

where T_c is the crater depth, d_p, ρ_p and v_p are the diameter, density and impact velocity of the projectile, respectively. Both equations have been extensively reviewed in EA Taylor et al. (1997)[1], where it has been suggested that the velocity exponent of the damage equation is not accurate enough. This was based on a large dataset (165 data) for different target and projectile materials and velocities. The data used in the comparison was a compilation of all previously published events in the general literature. It covered projectile size range of 48 - 2500 μm, a density range of 2 - 20 g cm^{-3} and a velocity range of 2-17 km s^{-1}. A further complication is that one of the basic assumptions on constructing the damage equations was that all the glass targets have similar behaviour under hypervelocity impact. However, further work by EA Taylor[2] suggests the opposite where quartz, pyrex, soda-lime and borosilicate glass excibit different behaviour.

In order to assess the validity of the glass damage equations, further simulations were performed using the GAM at 5-15 km s^{-1} with an 1 mm spherical Aluminium 2017 projectile. Crater depth results are illustrated in Figure 5.9 together with damage equation predictions, some experimental data[1] and AUTODYN simulations using the J-H model[1,2]. It is clear that both models predict a much smaller velocity dependence than the damage equations. By fitting an equation of the form

Figure 5.6: Low density projectiles + hydrocode runs

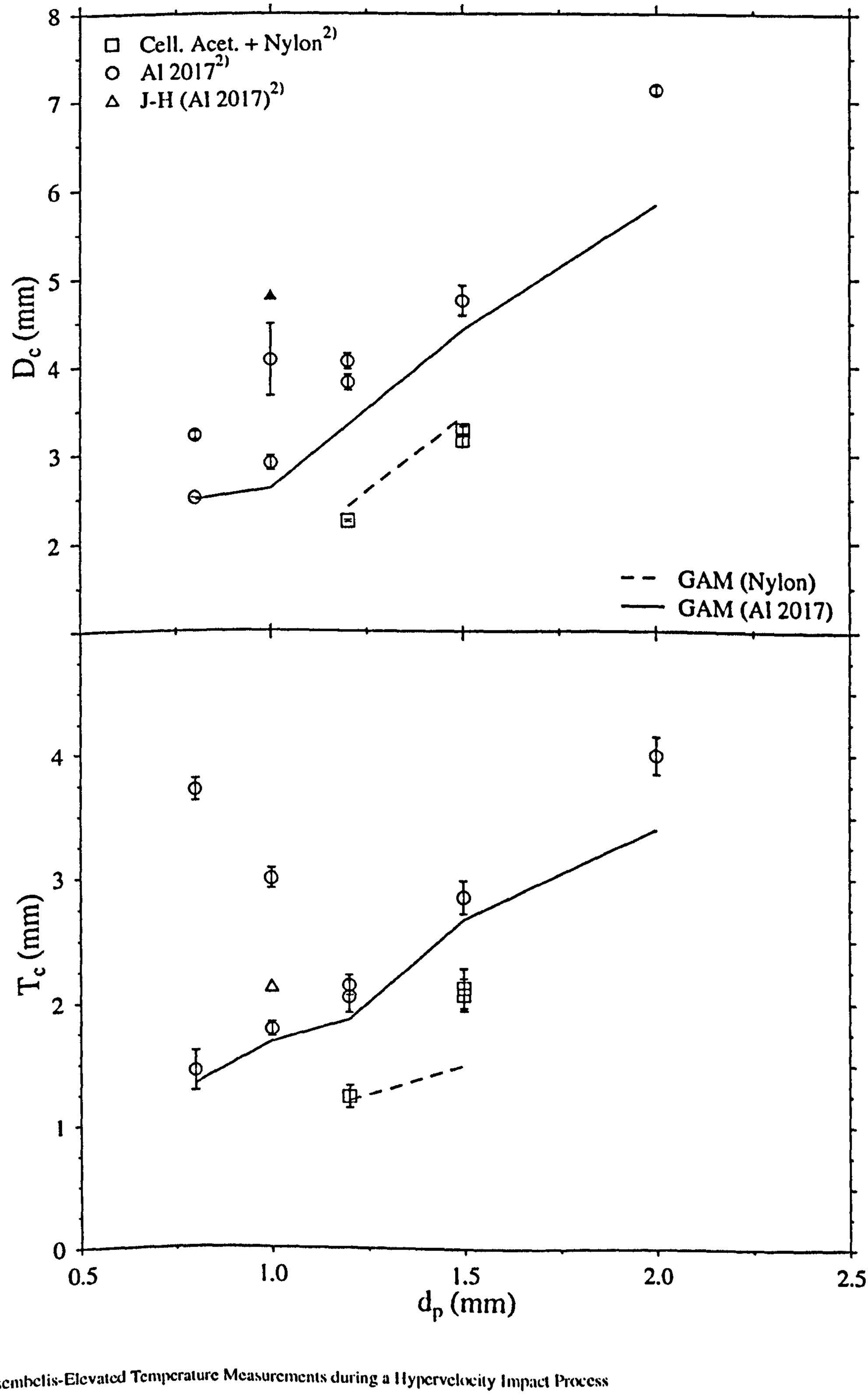

Figure 5.7: Medium density projectiles + hydrocode runs

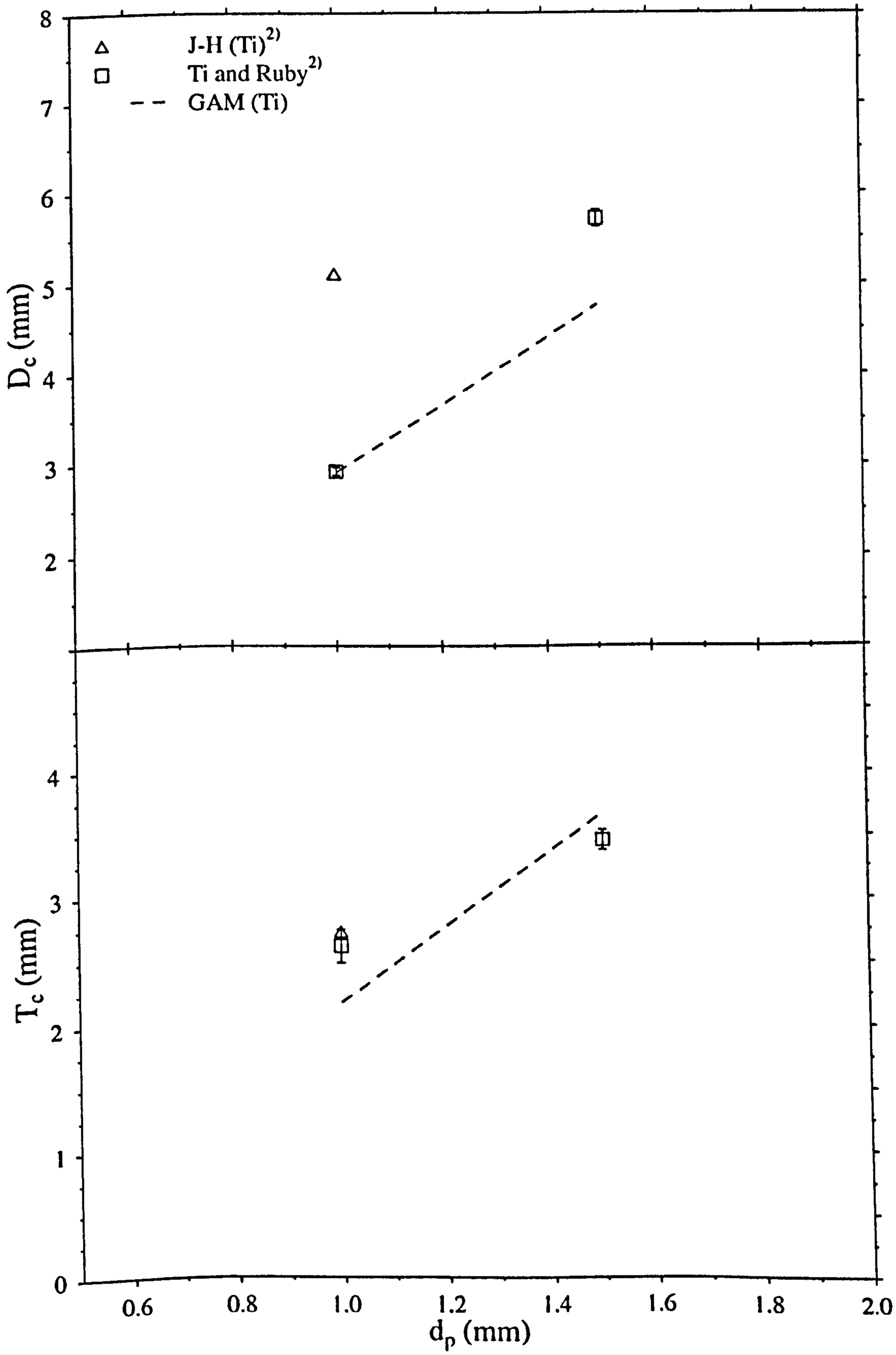

Figure 5.8: High density projectiles + hydrocode runs

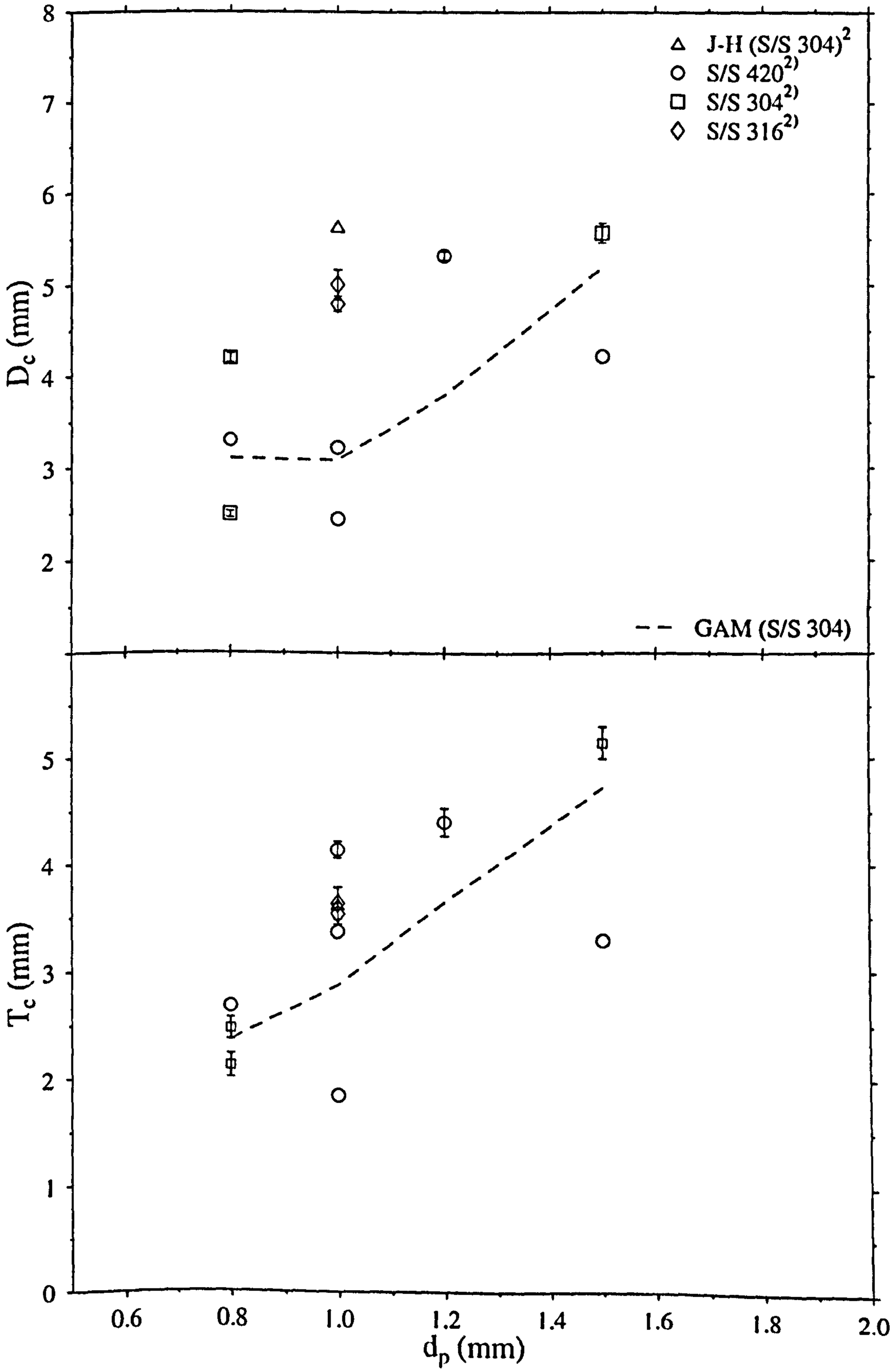

Figure 5.9: Comparison with Damage Equations

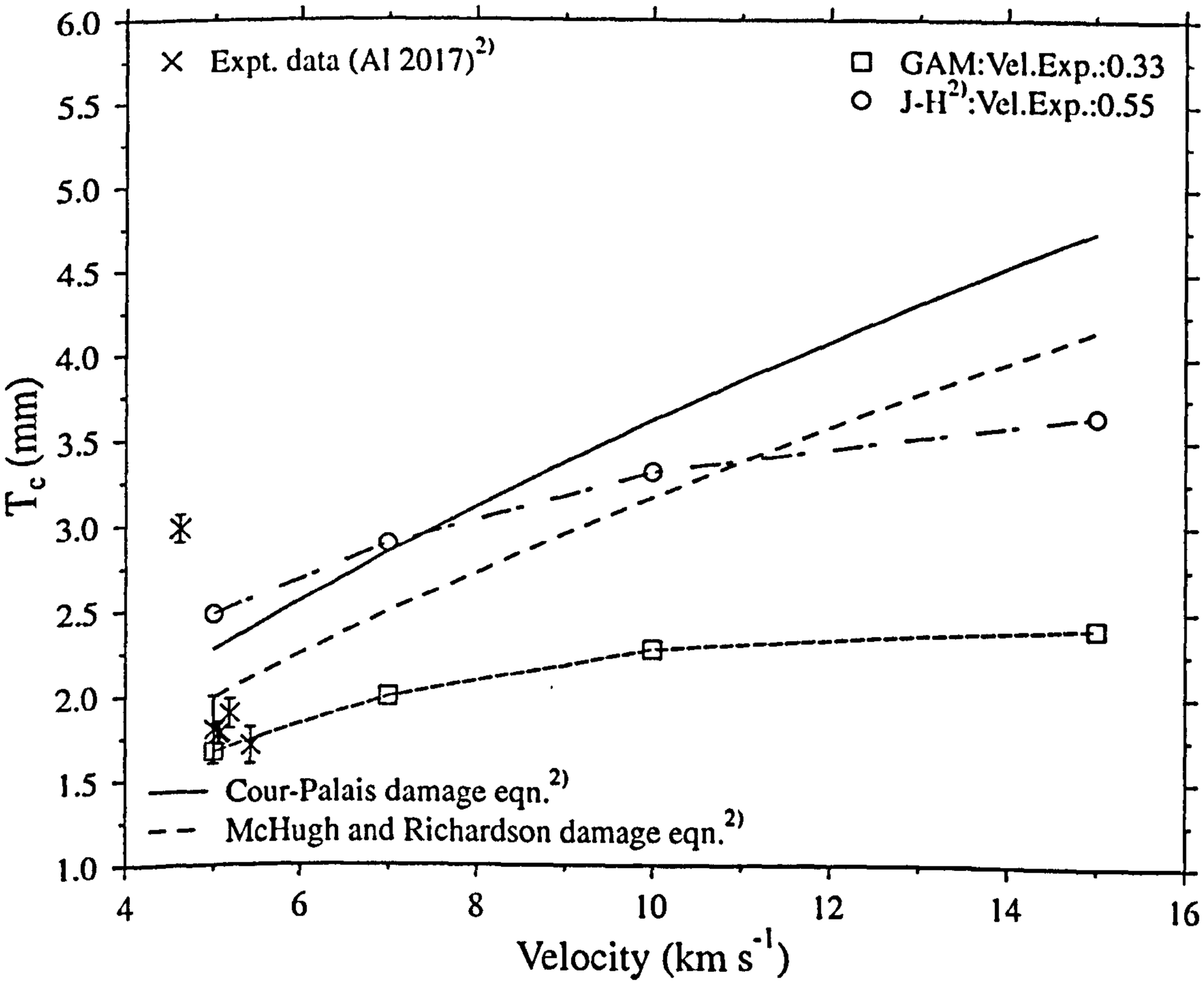

Figure 5.10:Fractional increase of intact and fractured strength with strain rate

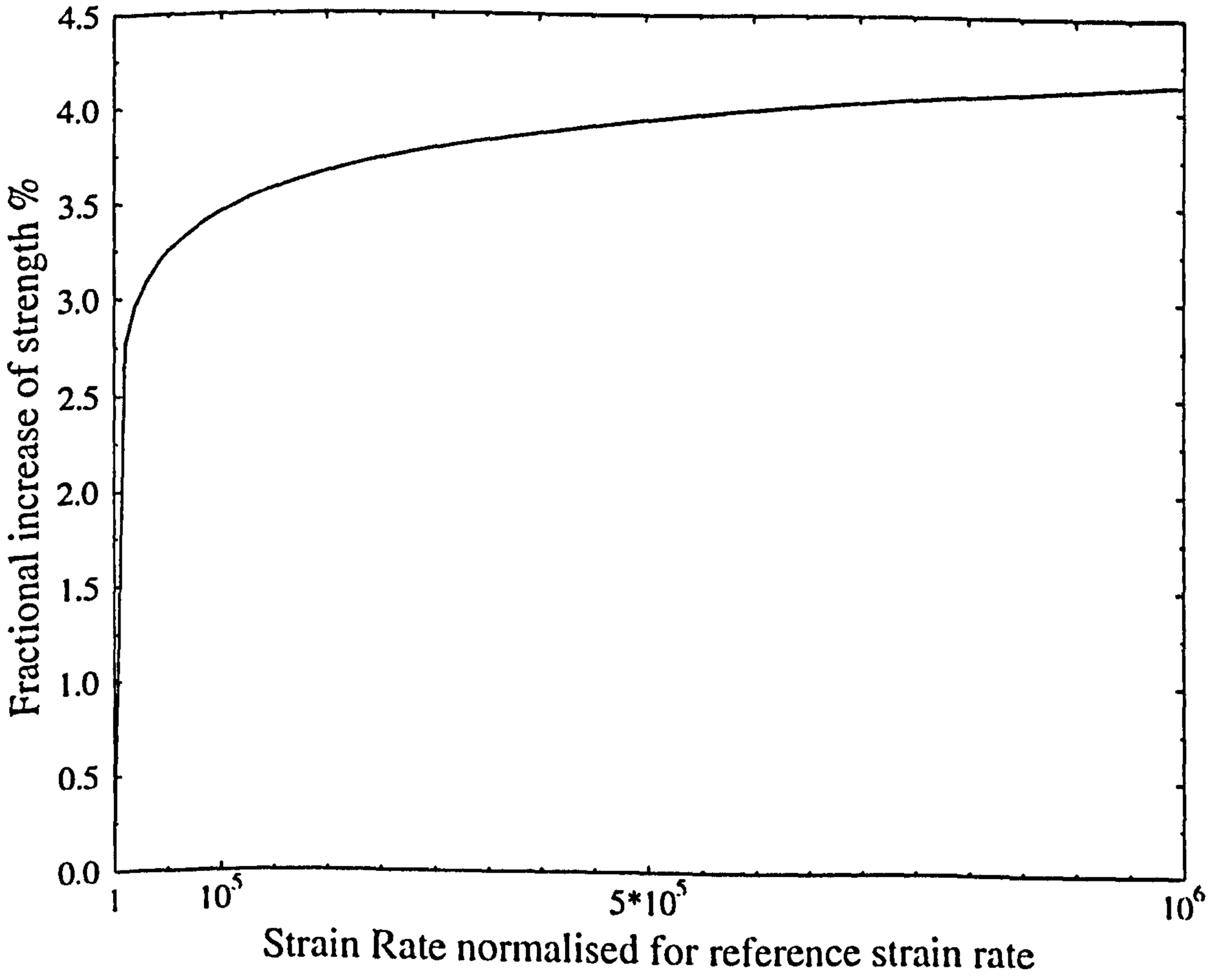

$$T_c = a v_p^{\,b} \tag{5.5.3}$$

to the hydrocode simulation results, one get

using GAM: $T_c = 0.99 v_p^{\,0.33}$ (5.5.4)

using J-H model: $T_c = 1.01 v_p^{\,0.55}$ (5.5.5)

The discrepancy between the damage equations and the simulations may arise from the fact that the damage equations or the models used are inaccurate. Unfortunately, in this stage there is no way to predict which is the case. Therefore, further experiments are needed at higher velocities to clarify this important result and determine which value of b is correct.

5.6 Discussion of Crater Dimension Results and Further Improvements

As it was mentioned in the previous section, the GAM and J-H models give different results, where the former underpredicts while the latter overpredicts the experimental results. This discrepancy, may, partly, be attributed to the different way the yield strength is being calculated. In the Glass Analogue Model the yield strength increases with pressure up to a point and then remains constant as pressure increases. Although the same happens with the J-H model, there is a big difference. The yield strength decreases as damage accumulates. Therefore, if the value of damage becomes unity (i.e. fully fractured material) relatively early in the calculation, the yield strength as calculated by the J-H model will be smaller than the one estimated by the GAM. Hence, the material in the GAM will be stronger and the crater dimensions smaller.

This is illustrated in Figures 5.11-5.13 where a Titanium projectile of 1 mm diameter impacts on glass at 5 km/s. Figure 5.11 shows the yield strength of the glass target 18 μs after the impact using the GAM, while Figure 5.12 and 5.13 (courtesy of EA Taylor) illustrate the glass yield strength and cumulative damage, respectively, 13 μs after the impact using the J-H model. One can see that the yield strength is 0.62 GPa (this corresponds to maximum strength) underneath the crater using the GAM. However, in the J-H case, since damage is one, the strength is almost close to zero, or rather to the fracture strength.

A way to remedy the situation, is to use the strain rate dependence in the J-H model. The J-H simulations were performed without the strain rate dependence option, thus making the material less stronger than it should, normally, be for the high strain rates applicable to a hypervelocity impact. However, the strain rate constant is only 0.003, suggesting a rather weak dependence on the strain rate. The fractional increase of both the intact and fractured strength of the J-H model as a function of strain rate is illustrated in Figure 5.10. Even at a strain rate of 10^{6}

s^{-1}, the fractional increase is only 4%. Hence, only the implementation of the strain rate dependence will give an insight to this option.

The way that damage accumulates may play a significant role to the final crater dimensions. Although the damage is a function of the hydrostatic pressure, the rate of damage with strain is not. In this way, there is no time between the passage of the shock wave and material failure lading to higher failed material volumes. Therefore, more complex failure models are required where the rate of damage itself is a function of damage and stress[17] leading to time-dependent models. However, most such models are still in their development and testing stage by the Ministry of Defence and its related agencies. Hence, not many of them exist in the published literature.

Another possible reason for discrepancy between the two models may lie inside the EOS. The J-H did not include any energy dependence, while in the GAM a Mie-Gruneisen EOS form was used which includes energy dependence. Therefore, it is possible that some of the energy transferred to the target by the projectile kinetic energy, (that would, normally, used to melt the material), was, instead, used as kinetic energy, hence the material had higher velocity, which could imply larger crater.

Although in principle the J-H model should be superior to GAM, it is not in practise. We have already discussed and suggested ways for improvement. These include:

- Estimation of how quickly damage accumulates in the J-H model. This may, partly, explain the discrepancy between the two models.
- Inclusion of the strain rate dependence.
- Inclusion of energy dependence, and for more flexibility Equation (5.3.16) could be implemented.
- Inclusion of thermal softening effects by implementation of Equations (5.3.21) and (5.3.22).

If these changes are made it would be interesting to see how the J-H model predictions change.

5.7 Problems with Temperature Calculations using AUTODYN™

For the ejecta temperature estimations, the three main AUTODYN schemes were used; Langrange, SPH, and Euler. Unfortunately, all the three of them had problems which prevent the estimation of the temperatures. In this section, a summary of the problems will be given together with some future improvements to remedy the situation.

Firstly, the Langrangian scheme, suffers from the erosion algorithms. As mentioned in section 5.2, erosion algorithms are used in a Langrangian calculation to 'delete' cells that have been, severely, distorted. However, the fastest and hottest ejecta, in a hypervelocity impact process, come from material regions that have been subjected to high pressures/temperatures and thus are significantly volumetrically distorted. Therefore, these regions, in a Langrangian hydrocode simulations, will be discarded. Hence it is impossible to use the Langrangian scheme to estimate ejecta temperatures.

The SPH technique is more promising, since it does not involve any erosion algorithms. However, as it is already mentioned, its present form cannot conserve energy, and energy errors are of the order of 50%. Therefore, estimation of ejecta temperatures is redundant.

Thus, only the Euler scheme is left to try. A few runs were tried, where a 1mm iron spherical projectile was impacted onto soda-lime glass at 5, 7, 15 km/s. Unfortunately, even in the case of this scheme, two problems appeared.

1. Not a lot of ejected material was observed, even at velocities of 10 km/s. This problem arises from the fact that a very fine grid is required to accurately track the small particles of material as it moves through the grid. However, an extremely fine grid is impossible to use in a PC because of time. The remedy would be to use a much more powerful computer would be suitable for this work.
2. A bigger problem was that almost every run crashed due to floating point errors. The problems emanated from individual cells which had temperature values of the order of 10^{25} K! This was, of course, unreasonable, and hence the calculation was terminated. This problem partly arises from the fact that Euler schemes have difficulties associated with calculating the temperature for multi-material cells which contain small amounts of one material and the temperature can sometimes become very large[18]. In addition, lack of material data in the high velocity regime makes temperature calculations in hydrocodes difficult[19]. Ideally, one would want to know how the various heat capacities behave over the changes that exist in a given impact, including the effects of phase changes.

The problem of extremely high cell temperatures can be, numerically, solved by 'capping' the temperature. I therefore suggest that a user subroutine be used in AUTODYN™ to impose a maximum value on the temperature. Of course, whilst avoiding numerical errors it is no guaranteed of accurate results.

Thus whilst the theory behind temperature calculations is rigorous, AUTODYN™ has several deficiencies that prevent accurate calculations of temperature. Therefore, until some of

the aforementioned problems solved, it would difficult to reliably, estimate the ejecta temperatures using AUTODYN™.

5.8 Thermodynamic Stability of the GAM EOS in hydrocode simulations

A good Equation of State should be consistent with thermodynamics and basic rules of shock wave physics. For that reason, Segletes[8,9] devised four criteria that a Mie-Gruneisen EOS should meet in order not to violate thermodynamics. Violating basic laws in hydrocode calculations should lead to negative absolute energies or pressures exploding or collapsing elements or negative element stiffnesses[8]. These inconsistencies may, for example, result in the decrease of entropy along shocks. In this section, these criteria will be presented and used to check the GAM EOS validity.

The GAM EOS has already been described in section 5.3. It is given by the following equations:

$$P-P_H = \gamma\rho(E-E_H) \tag{5.8.1}$$

with

$$P_H = \frac{c_0^2(V_0-V)}{\left[V_0-S(V_0-V)\right]^2} = \frac{\rho_0 c_0^2\mu(1+\mu)}{\left[1-(S-1)\mu\right]^2} \tag{5.8.2}$$

and

$$\gamma=\gamma_0\rho_0/\rho = \gamma_0/(\mu+1) \tag{5.8.3}$$

with c_0=3.3 km s^{-1}, S=1.5, γ_0=1.32 and ρ_0=2.23 g cm^{-3}. V is the specific density ($1/\rho$) and μ is the compression ($\mu=V_0/V-1$).

The four criteria or instability modes are described as following:

1) At a post-shock state (P_H, V_H), the slope of the Hugoniot curve with respect to density must exceed the slope of the Rayleigh line connecting the pre-shock state (P_0, V_0) and the post-shock one. That is the Hugoniot must rise more steeply (with decreasing V) than the Rayleigh line. Therefore:

$$\frac{dP_H/d\rho}{\partial P/\partial\rho|_R} > 1 \tag{5.8.4}$$

or

$$\frac{dP_H/d\rho}{\partial P/\partial\rho|_R} = \frac{\left[1+(S+1)\mu\right]}{\left[1-(S-1)\mu\right]} > 1 \tag{5.8.5}$$

Clearly, Equation (5.8.5) is always valid $\forall S \in (0, \infty)$.

2) At the state (P_H, V_H), the slope of the isentrope must lie between the slope of the Hugoniot and the slope of the Rayleigh line connecting pre-shock and post-shock states. This criterion, simply, states that the slope of the isentrope which is related to the sound speed need to be not only positive but greater than the Rayleigh line. Mathematically, the Mode II criterion can be proved[8] to be expressed as:

$$0 < \gamma < 2/\mu \tag{5.8.6}$$

However, the compression μ cannot increase indefinitely. From Equation (5.8.2) one can see that the pressure goes to infinity when $\mu=\mu_x=1/(S-1)$. In addition, at μ_x the value of the Gruneisen coefficient γ_x should also satisfy Equation (5.8.6).

3) The slope of an isentrope with respect to density (i.e. the sound speed) is always greater than zero. Although this has been covered in the Mode II criterion, Mode III gives the opportunity to study stability at all states in the P-V or P-μ plane, not just along the Hugoniot. Mathematically, for a Mie-Gruneisen EOS, it can be given as:

$$\left(\frac{\gamma+1}{1+\mu}+\frac{1}{\gamma}\frac{d\gamma}{d\mu}\right)(P-P_H)+\frac{dP_H}{d\mu}\left(1-\frac{\gamma\mu}{2}\right)+\frac{\gamma}{2(1+\mu)}(P_H-P_0)>0 \tag{5.8.7}$$

4) The last criterion states the trivial fact that the post-shock pressure must always be higher than the pre-shock one. Mathematically, it is expressed in the following form:

$$\gamma \geq \frac{\gamma_0}{1+(\gamma_0+1)\mu} \tag{5.8.8}$$

Modes I-IV should be valid for all the Mie-Gruneisen EOS's. However, the material of interest is the soda-lime glass. Throughout the rest of this section it will be shown that the EOS used in the GAM model satisfy all the four criteria, and thus, it is thermodynamically stable to use in hydrocodes.

Figure 5.11

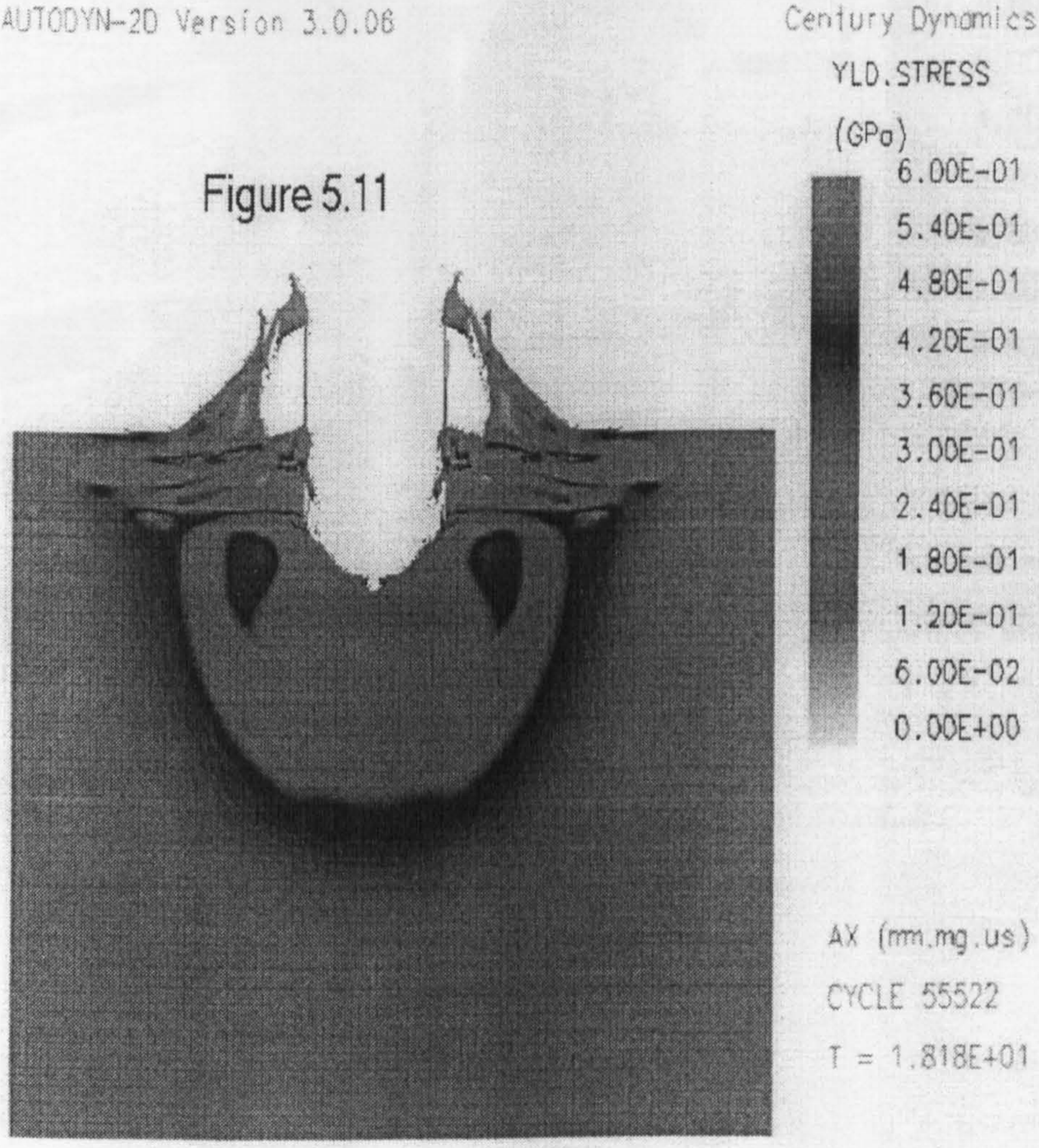

GLAT10: 1.0 MM TITANIUM TO GLASS AT 5 KMS-1

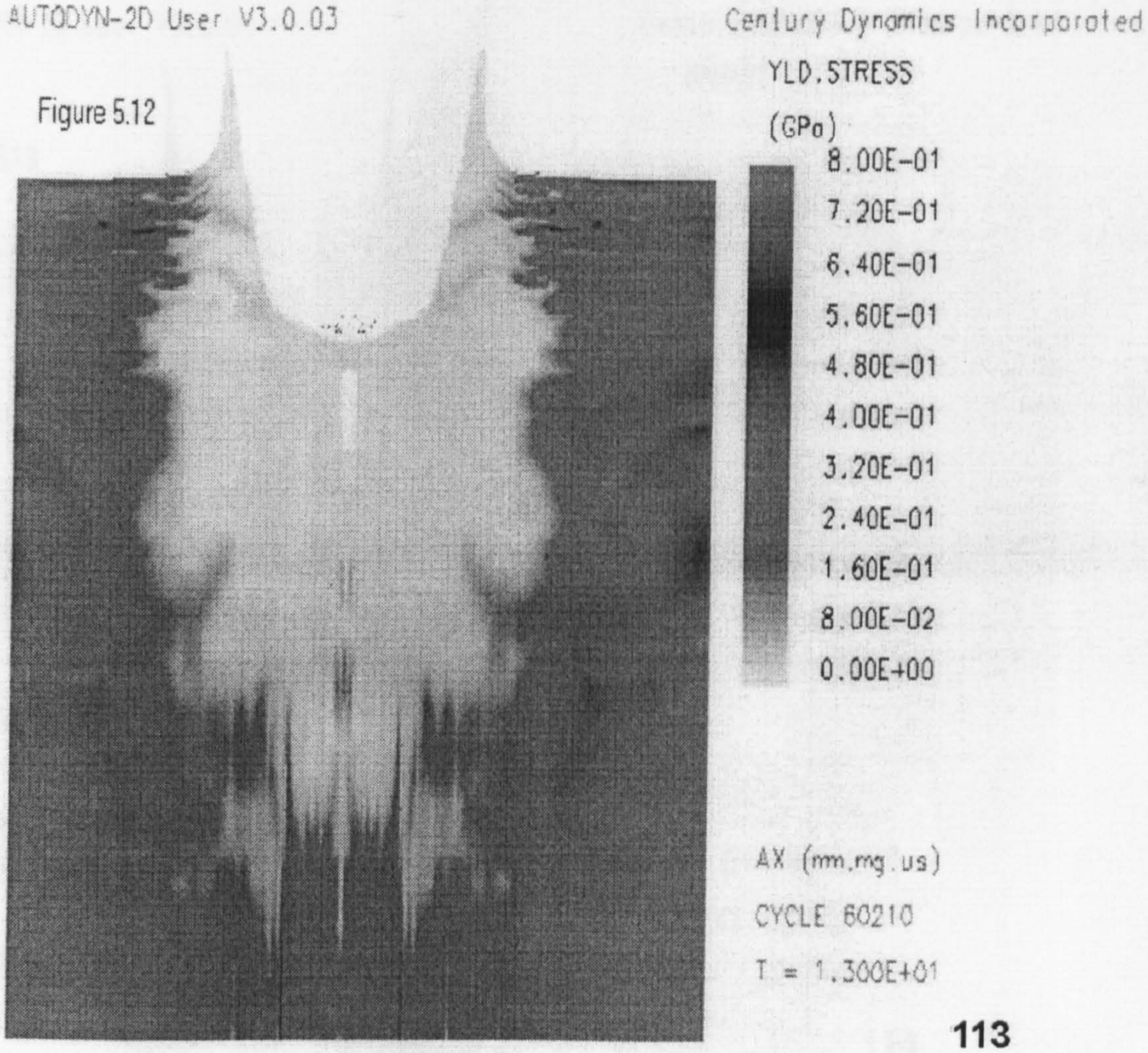

Figure 5.12

KTT101: 1.0 MM TITANIUM TO GLASS AT 5 KMS-1

Figure 5.13

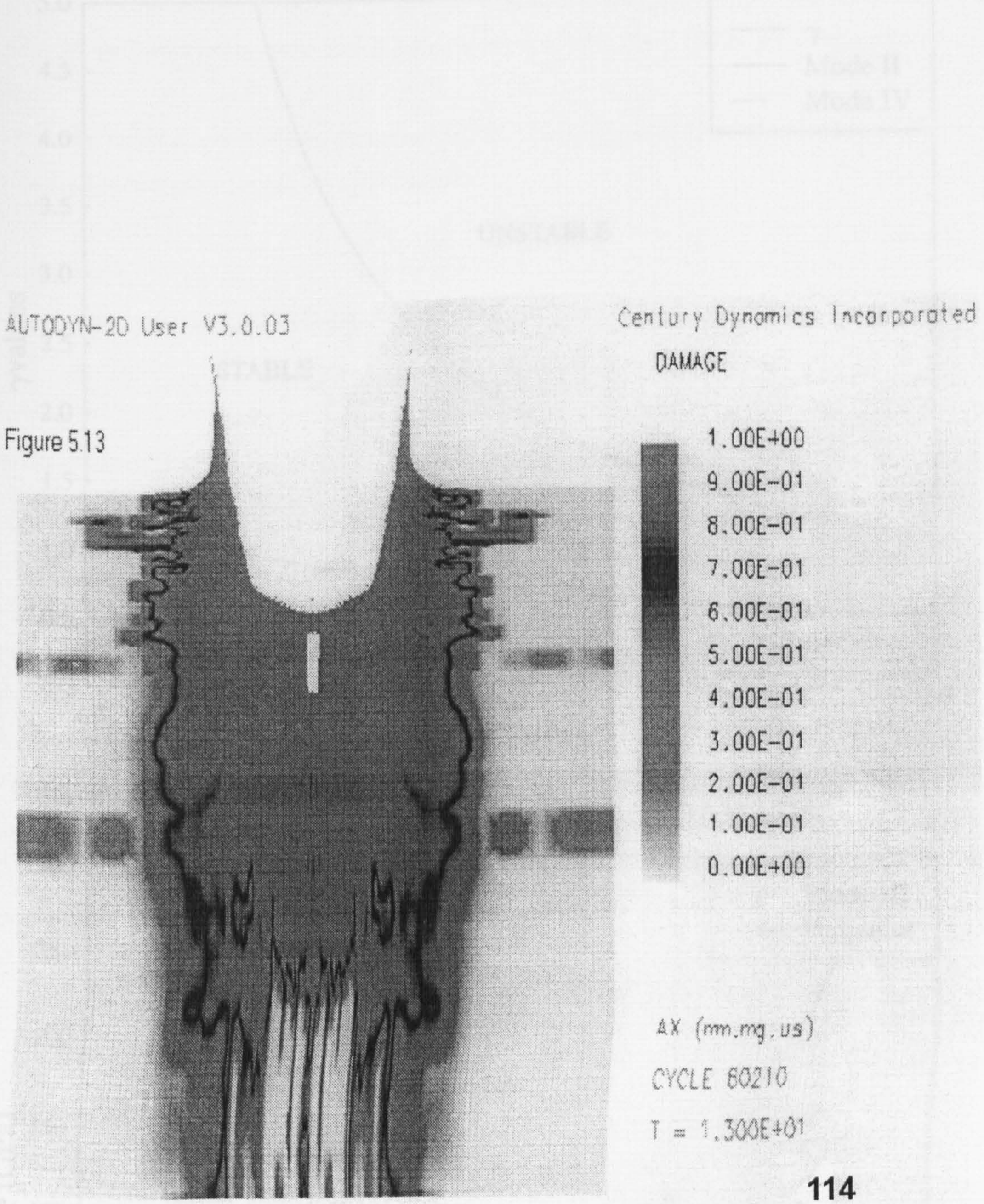

KTTI01; 1.0 MM TITANIUM TO GLASS AT 5 KMS-1

Figure 5.14: Modes II and IV Criteria for GAM EOS

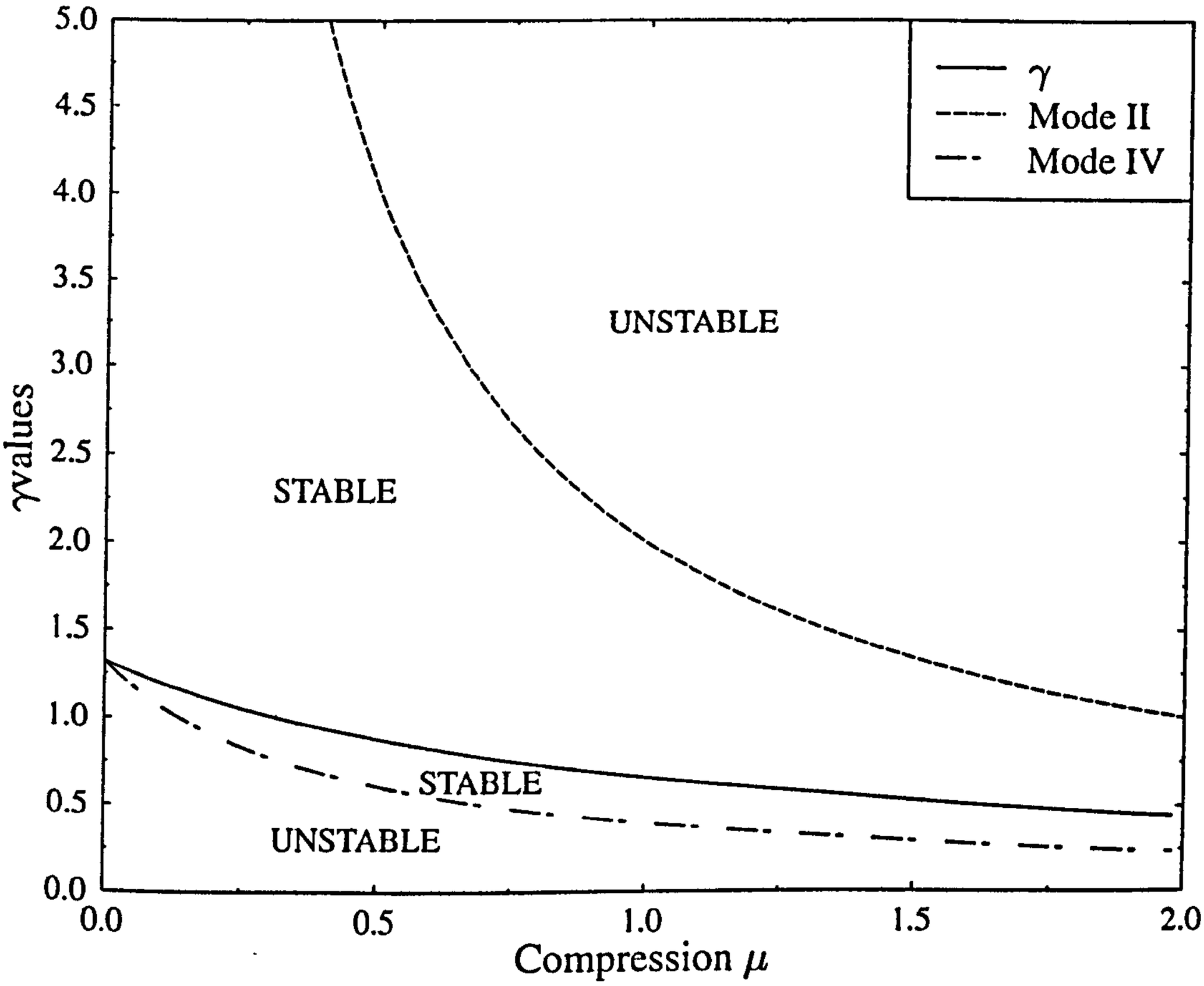

Figure 5.15: Mode III Criterion for GAM EOS

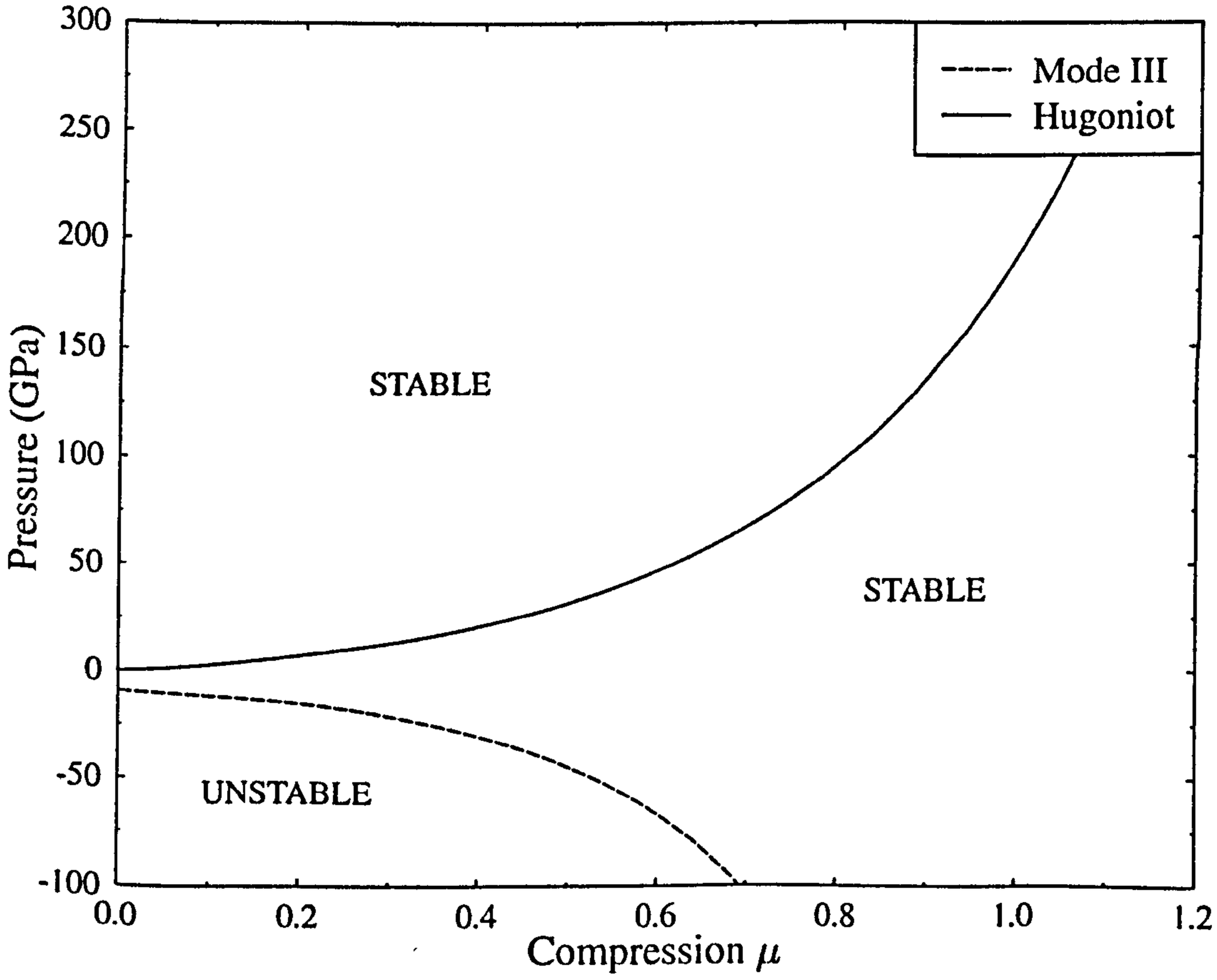

Mode I criterion is immediately satisfied since S has a value of 1.5, which is greater than zero.

The value of γ is given by Equation (5.8.3). Combining Equations (5.8.3) and (5.8.6) we derive the Mode II criterion for the GAM model:

$$0 < \frac{\gamma_0}{\mu+1} < \frac{2}{\mu} \quad \forall\, \mu > 0 \tag{5.8.9}$$

Rearranging Equation (5.8.9) we derive that the Mode II criterion finally is:

$$0 < \gamma_0 < 2 + \frac{2}{\mu} \quad \forall\, \mu > 0 \tag{5.8.10}$$

The rhs of inequality (5.8.10) becomes minimum when μ is maximum, i.e., when $\mu = 1/(S-1)$:

$$\gamma_0 \in (0,\ 2S) \quad \forall\, \mu > 0 \tag{5.8.11}$$

However, the value of γ_0 is 1.32, therefore, the GAM model is Mode II stable. It can also be seen graphically. Equation (5.8.9) is illustrated in Figure (5.14), where it can be seen that Mode II is never violated. The maximum compression for glass is $\mu_x = 1/(S-1) = 2$. At this value the Gruneisen coefficient has a value of 0.44 which is smaller than $1/\mu_x = 4$. It is interesting to say that Equation (5.8.11) holds for any material which has a Mie-Gruneisen EOS of the form given by Equation (5.8.1) and the Gruneisen coefficient γ is linear in density. This implies that any material with $\gamma_0 > 2S$ with γ linear in ρ violates the Mode II criterion.

If in Equation (5.8.7) the values of glass for zero initial pressure are substituted, then the Mode II criterion takes the following form:

$$P > \frac{24.2847\mu(\mu+1)}{(1-0.5\mu)^2} - \left[\frac{\dfrac{24.2847(1+0.5\mu)}{(1-0.5\mu)^3}\cdot\left(1-\dfrac{0.66}{\mu+1}\right)+\dfrac{3.8856}{(\mu+1)(1-0.5\mu)^2}}{\dfrac{2.32+\mu}{(\mu+1)^2}-\dfrac{1}{\mu+1}}\right] \tag{5.8.12}$$

Figure (5.15) illustrates the right hand side of Equation (5.8.12) together with the Hugoniot curve for comparison purposes. It is apparent that the Hugoniot curve never violates the Mode III criterion. The GAM EOS becomes unstable to a small portion of the P-μ plane, which represents material under large tensions. Therefore the tensions required to produce instability are very high, 9.2 GPa at $\mu=0$ ($\rho=\rho_0$). However the spall strength of soda lime glass is about 5 GPa[20] and thus the material will fail before it approaches this unstable thermodynamic state.

Finally, the Mode IV criterion, using Equations (5.8.3) and (5.8.8) takes the form:

$$\frac{\gamma_0}{\mu+1} \geq \frac{\gamma_0}{1+(\gamma_0+1)\mu} \tag{5.8.13}$$

Rearranging Equation (5.8.13) we obtain:

$$\gamma_0 \mu \geq 0 \tag{5.8.14}$$

However, Equation (5.8.14) is always true for compressions if Mode II is satisfied. It is apparent that it is satisfied for the GAM model. Equation (5.8.13) is illustrated graphically in Figure (5.14). It can be said that Modes II and IV provide an upper and a lower bound for the Gruneisen coefficient, both depicted in Figure (5.14).

Thus, the GAM EOS meets Segletes modes of stability and provide further confident to the model.

5.9 Conclusions

In this chapter, a Glass Analogue Model (GAM) for hydrocodes was presented for predicting depth and diameter of the central pit of a soda-lime glass crater during a hypervelocity impact. Results were compared against experimental work and hydrocode simulations using the Johnson-Holmquist model performed by EA Taylor. Results using the GAM were found to agree better with experiments than using the J-H model. However, some further improvements of the J-H were suggested which may make the J-H more suitable for the hypervelocity regime.

In addition, a crater depth dependence on impact velocity using the GAM was established, which was different from the established damage equations. The J-H model also has a velocity dependence different to the damage equations but lies between GAM's and equations'.

Finally, it was proved that the way AUTODYN calculates temperature is equivalent to the way temperatures have been estimated by the author in chapter 3. However, due to numerical limitations and a general lack of knowledge of appropriate material data, it was impossible to have an estimation of ejecta temperatures using AUTODYN™.

References

1. Taylor E A et al., (1997), 'Hydrocode Modelling of Space Debris Hypervelocity Impact on Soda-Lime Glass Using the Johnson-Holmquist Brittle Material Model', Proc. 2nd Eur. Conf. Space Debris, Darmstadt, Germany, 449-453.
2. Taylor E A, (1997), 'Experimental and Computational Study of Hypervelocity Impact on Brittle Materials and Composites', Unit for Space Sciences and Astrophysics, University of Kent, Ph.D. Thesis.
3. AUTODYN™ Theory Manual (Century Dynamics Inc., Oakland, CA, 1995).
4. Birbaum N K, Cowler M S , (1987), 'Numerical Simulation of Impact Phenomena in an Interactive Computing Environment', Proc. Of Int. Conf. On Impact Loading and Dynamic Behaviour of Materials', 'IMPACT '87', Bremen, Germany.
5. Randles P W, Libersky L D, (1996), 'Smooth Particle Hydrodynamics: Some Recent Improvements and Applications', Computer Methods in Applied Mechanics and Engineering, Meshless Methods, pre-print.
6. Gardner D J, (1995), 'Hypervelocity Impact Morphology', Unit for Space Sciences and Astrophysics, University of Kent at Canterbury, Ph.D. thesis.
7. McSherry F, (1995), 'Numerical Simulations of Hypervelocity Impacts on Solar Arrays', ESA Study Contract Report, No 11693/95/NL/JG.
8. Segletes S B , (1991), 'Thermodynamic Stability of the Mie-Gruneisen Equation of State, and its Relevance to Hydrocode Computations', *J. Appl. Phys.*, **70**, 2489-2499.
9. Segletes S B , (1994), 'Further Examination on the Thermodynamic Stability of the Mie-Gruneisen Equation of State', *J. Appl. Phys.*, **76**, 4560-4566.
10. Holmquist T J et al., (1995), 'High Strain Rate Properties and Constitutive Modelling of Glass', 15th International Symposium on Ballistics, Jerusalem, Israel.
11. Alwes D, (1990), 'Columbus-Viewport Glass Pane Hypervelocity Impact Testing and Analysis', *Int. J. Impact Engng*, **10**, 1-22.
12. Asay J R and Shahinpoor M , (Eds), (1993), 'High-Pressure Shock Compression of Solids', Springer-Verlag, NY.
13. Kipp M E et al., (1997), 'Elastic Shock Response and Spall Strength of Concrete', *Shock Compression of Condensed Matter,* Schmidt S C et al. (Eds), AIP Press, NY, (to appear).
14. Tanner W G , Jr, (1995), 'Meteoroids and Space Debris Hypervelocity Impact Penetrations: The role of Hydrocodes', Unit for Space Sciences and Astrophysics, University of Kent at Canterbury, Ph.D. thesis.

15.Touloukian Y S (Ed.), (1970), 'Thermophysical Properties of Matter', Plenum, N.Y.

16.Taylor E A , and McDonnell J A M , (1996), 'Hypervelocity Impact on Soda-Lime Glass: Damage Equations for Impactors in the 400-2000 μm Range', COSPAR '96, Birmingham, UK.

17.Goldthorpe B D, (1997), 'A Path Dependent Model for Ductile Fracture', *J. Phys. IV France*, **7**, 705.

18. Iain Livingstone, Century Dynamics Ltd., (1997), private communication.

19.Iain Livingstone, Century Dynamics Ltd., (1997), private communication.

20.Rosenberg Z, et al., (1985), 'Spall Strength of Shock-Loaded Glass', *J. Appl. Phys.*, **58** (8), 3249.

CHAPTER 6

Conclusions and further work

Conclusions

The temperature of the ejecta cloud when iron impacted soda-lime glass was measured both experimentally and theoretically. The experimental program was performed using the 2 MV Van de Graaff accelerator facility of the university of Kent. Two photomultiplier tubes, with filters at different wavelengths, were detecting the light flash produced by the hot and radiating ejecta cloud. The specific energy at these two different velocities was fitted to a black body spectrum. The temperature of the cloud was then discovered to be 2600 ± 250 K and largely independent of iron dust particle velocity; that result, although surprising, implied that the experimental value was close to the vaporisation temperature of the material. For the theoretical calculations a computer code was constructed using principles of thermodynamics and shock wave physics, namely, a Mie-Gruneisen equation of state and subsequent full release. The theoretical calculations showed that the glass ejecta cloud had a temperature close to the target vaporisation temperature and hence supported the experimental results.

The code has also been used to estimate the velocity threshold for impact plasma production. Those calculations were used for the calibration of the Cosmic Dust Analyser (CDA) which flies on the Cassini/Hyugens space mission to the Saturnian system. The calculations agreed better with experiments than those using molecular dynamics calculations (P R Ratcliff), as shown in chapter 3. These results provide an independent, theoretically based and efficient way to check the validity of the CDA calibration experiments.

Finally a simple model (GAM) was constructed for the dynamic behaviour of soda-lime glass to be used in the AUTODYN™ hydrocode using a Mie-Gruneisen EoS and a Mohr-Coulomb strength model. The model was used to predict the glass crater morphology and results were compared against experiments and hydrocode simulations using the Johnson-Holmquist (J-H) brittle material model performed by E A Taylor. GAM results showed good agreement with experiments within 15% and better agreement than the J-H model. For that reason, two new possible implementations were suggested for the J-H model to include energy dependence in the J-H EoS and to address the issue of thermal softening.

Further work

A way to obtain more accurate results in the accelerator facility would be to use more than two wavelengths. In this way we could establish the specific energy as a function of impact velocity at many wavelengths and to fit a more accurate blackbody spectrum. In addition, dust impactors other than iron may be used. The Van de Graaff may currently also accelerates boron carbide and latex particles. It would, therefore, be interesting to address the possible differences in the ejecta cloud temperature of glass when impacted by different material. The way developed to calculate temperatures can be extended to other materials than glass.

Another issue than may be addressed is the shock temperature of the material. As explained in chapters 2 and 3 the shock wave heats the material to a high temperature and then the release takes the material to a lower temperature which can then be measured using the technique described in chapter 4. In the case for transparent materials such as glasses, it may be possible to observe the light emanating from the shock wave travelling inside the material if a photomultiplier tube is placed in the antipodal side of the impact surface. Thus, a temperature may be established for the shock front..

Finally, the issue of autoemission could be addressed. It has been explained in chapter 3, that the microparticle impactors may ionise and hence reach extreme temperatures because of their electric charge . However the timescale of such an event is of the order of few nanoseconds. That is why new photomultiplier tubes can be used with sub-nanosecond response. In this way it would be possible to assess and distinguish between a light flash from an autoemission event which is a surface effect and a flash from the impact generated ejecta cloud which is a bulk event of both projectile and target materials.

APPENDIX A

Derivation of the Hugoniot Relations

The derivation comes from Melosh H J, (1989), 'Impact Cratering: A geologic Process', Oxford University Press, N.Y, 228-229, ISBN 0-19-510463-3.

AI.1 Mass Conservation

Figure A1.1 illustrates a block of material through which a shock wave is passing. This is a 'freebody' diagram in the sense that all forces acting on the block are explicitly shown. The cross-sectional area of the block A is constant as the shock moves through it. The pressures P and P_0 on the block's sides are not shown in the figure to avoid confusion: they are completely balanced and so play no direct role in driving the shock, so they are ignored in this derivation. Only the pressures acting on the ends of the block, in the direction of the shock wave motion, are significant.

The figure shows the block at two different times, t and t^1. At the earliest time t, the length of the unshocked region is l_u and the length of the shocked region is l_s. Later, at time t^1, the shock wave has progressed a distance $U(t^1-t)$ farther to the right and the shocked end of the

block, moving at the particle velocity u_p, has progressed $u_p(t^1-t)$ farther to the right. The unshocked end of the block, assumed to be at rest, has not moved. The new lengths of the unshocked region l_u^1 and shocked region l_s^1 are thus given by:

$$l_u^1 = l_u - U(t^1-t) \qquad \text{(AI.1.1a)}$$

$$l_s^1 = l_s + U(t^1-t) - u_p(t^1-t) \qquad \text{(AI.1.1b)}$$

The mass contained in the unshocked portion of the block at time t is its volume l_uA times its density ρ_0, $\rho_0 l_u A$. The mass in the shocked portion is likewise $\rho l_s A$. Mass conservation implies that the masses at times t and t^1 are equal. That is:

$$\rho l_s A + \rho_0 l_u A = \rho l_s^1 A + \rho_0 l_u^1 A \qquad \text{(AI.1.2)}$$

Cancelling through the common factor A, substituting Equations (AI.1.1a) and (AI.1.1b) for l_s^1 and l_u^1 in Equation (AI.1.2), then cancelling the terms ρl_s and $\rho_0 l_u$ on both the left and right hand sides we get:

$$0 = \rho(U-u_p)(t^1-t) - \rho_0 U(t^1-t) \qquad \text{(AI.1.3)}$$

Finally, cancelling the common factor (t^1-t) and rearranging, we obtain the first Hugoniot relation:

$$\rho (U - u_p) = \rho_0 U \qquad \text{(AI.1.4)}$$

AI.2 Momentum Conservation

Pressure P on the shocked end of the block in Figure AI.1 is larger than the pressure P_0 on the unshocked end, so a net force $F = (P-P_0)A$ acts towards the right, accelerating the material in that direction. The momentum of material in the block at time t, $\rho l_s u_p A$, is thus not equal to the momentum $\rho l_s^1 u_p A$ at time t^1. The difference is equal to the momentum imparted by the applied force F over the time interval t^1-t, $F(t^1-t)$. The net momentum balance is thus:

$$\rho l_s^1 u_p A - \rho l_s u_p A = (P-P_0)\, A\, (t^1-t) \qquad \text{(AI.2.1)}$$

Cancelling A throughout and substituting for l_s^1 using Equation (AI.1.1b), noting that the term $\rho l_s u_p$ is subtracted from itself on the left hand side of the equation, and further cancelling the common factor (t^1-t) from the remaining terms we obtain:

$$\rho(U-u_p)u_p = (P-P_0) \qquad \text{(AI.2.2)}$$

Now use Equation (AI.1.4) to replace $\rho(U-u_p)u_p$ by $\rho_0 U$ and rearrange to obtain the second Hugoniot equation:

$$P - P_0 = \rho_0 U u_p \qquad \text{(AI.2.3)}$$

A1.3 Energy Conservation

Like momentum, the total energy in the block at time t is not equal to that at time t^1 because the applied forces do work on the system. This work is equal to the force times the distance through which it acts. Since the displacement of the unshocked end of the block is zero, the total energy gained between t and t^1 is thus $PAu_p(t^1-t)$, equal to the force PA on the shocked end of the block times the distance $u_p(t^1-t)$ through which it acts. The total energy $E_{tot}(t)$ in the block at time t is the sum of the internal energies in the shocked and unshocked portions and the kinetic energy in the shocked portion:

$$E_{tot}(t) = \rho_0 l_u E_0 A + \rho l_s E A + \tfrac{1}{2}\rho l_s u_p^2 A \qquad \text{(AI.3.1a)}$$

Similarly, at time t^1 the total energy is:

$$E_{tot}(t^1) = \rho_0 l_u^1 E_0 A + \rho l_s^1 E A + \tfrac{1}{2}\rho l_s^1 u_p^2 A \qquad \text{(AI.3.1b)}$$

Energy conservation thus requires:

$$E_{tot}(t^1) - E_{tot}(t) = PAu_p(t^1-t) \qquad \text{(AI.3.2)}$$

Substituting Equations (AI.3.1a) and (AI.3.1b) into Equation (AI.3.2), cancel A through as before, substitute Equation (AI.1.1a) for l_u^1 and Equation (AI.1.1b) for l_s^1, and simplify. The common factor (t^1-t) may then be cancelled to obtain:

$$-\rho_0 E_0 U + \rho E(U-u_p) + \tfrac{1}{2}\rho u_p^2(U-u_p) = Pu_p \qquad \text{(AI.3.3)}$$

Now replace $\rho(U-u_p)$ by $\rho_0 U$ using the first Hugoniot equation to obtain:

$$\rho_0 U(E-E_0) + \tfrac{1}{2}\rho_0 u_p^2 U = Pu_p \qquad \text{(AI.3.4)}$$

By eliminating either U or u_p from Equations (AI.1.4) or (AI.2.3) respectively, between these equations, we get:

$$u_p = \sqrt{(P-P_0)(V_0-V)} \qquad \text{(AI.3.5a)}$$

and

$$U = V_0\sqrt{(P-P_0)/(V_0-V)} \qquad \text{(AI.3.5b)}$$

where $V = 1/\rho$ and $V_0 = 1/\rho_0$ are the specific volumes of the shocked and unshocked material, respectively. Substituting Equation (AI.3.5a) for u_p and (AI.3.5b) for U in Equation (AI.3.4), cancelling the common factor $\sqrt{(P-P_0)}$, and rearranging we finally get the third Hugoniot relation:

$$E - E_0 = \tfrac{1}{2} (P + P_0) (V_0 - V) \qquad \text{(AI.3.6)}$$

Figure AI.1 : Free body diagrams of a shock wave passing through a mass of material at times t and t_1.

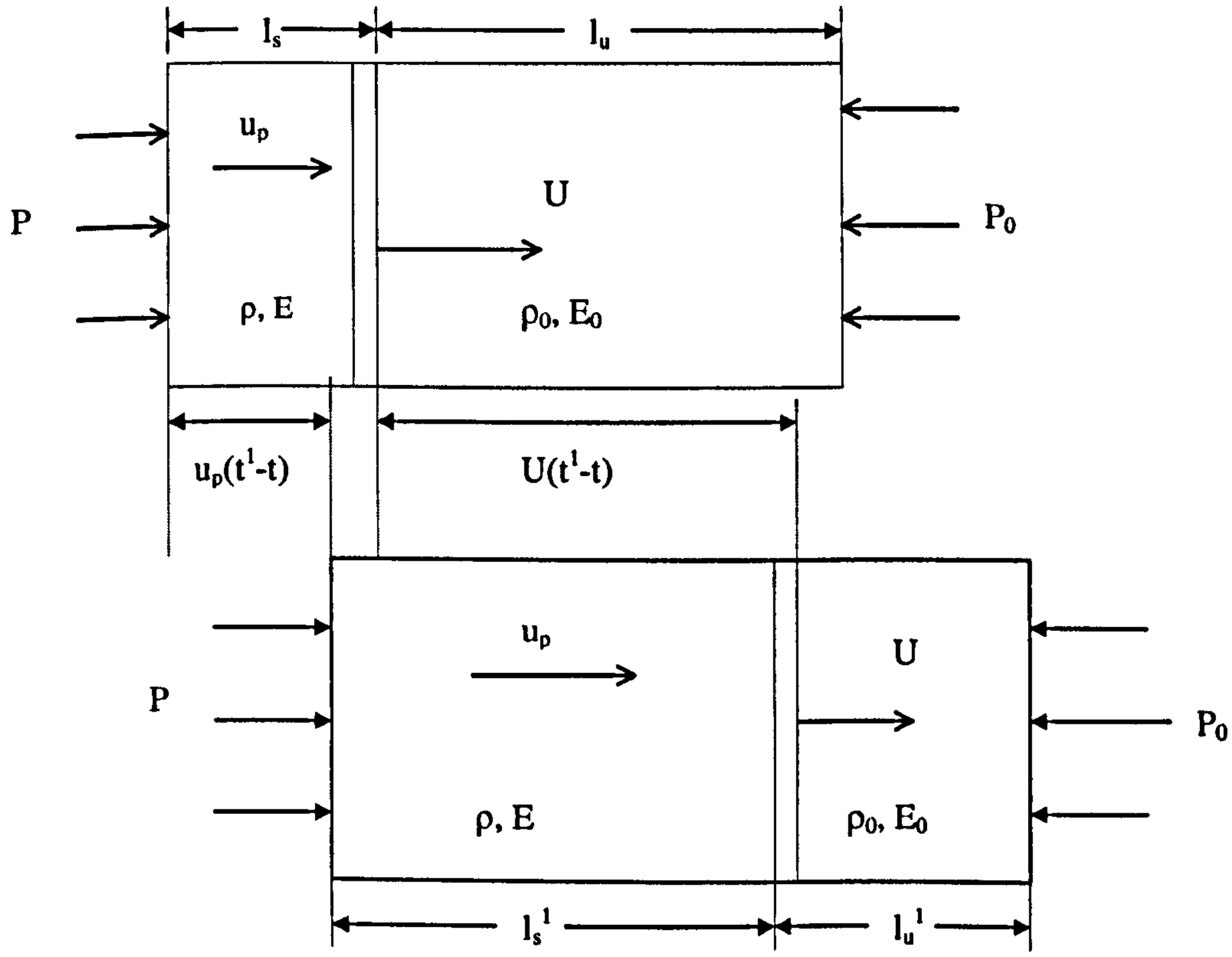

APPENDIX B

```
program shock
external Phoug, Thoug
double precision half, zero, Phoug, Thoug
double precision Pf, Pi, Ef, Ei, PH, EH, PH0, EH0, TH0, TH, TR
double precision Etotal, EHI, TR1, Tm, nf, Cp, TR2
double precision a, b, c, v, delv, delE, gamma, VH, V0
double precision delP, delUr, Urtotal
double precision delEim, delEcm, wheat
double precision rho0, AA, BB, Theta0, nk3, T0, Mmax
parameter ( half = 0.5d0, zero = 0.0d0 )

open (1, file="isentrop.dat", status='UNKNOWN')
open(5,file='al.dat',status='old')
write(*,*) 'Enter value for gamma :'
read(*,*) gamma
write(*,*) 'Enter value for VH (cm3/g):'
read(*,*) VH
write(*,*) 'Enter value for V0 (cm3/g):'
read(*,*) V0
write(*,*) 'Enter AA  : '
read(*,*) AA
write(*,*) 'Enter BB  : '
read(*,*) BB
write(*,*) 'Enter melting Temperature (K):'
```

```
read(*,*) Tm
write(*,*) 'Enter Specific Heat at constant Pressure (MJ/kgK)'
read(*,*) Cp
write(*,*) 'Enter Latent Heat of Fusion (MJ/kg):'
read(*,*) nf
write(*,*) 'Enter Theta0 : '
read(*,*) Theta0
write(*,*) 'Enter nk3  : '
read(*,*) nk3
write(*,*) 'Enter T0   : '
read(*,*) T0
write(*,*) 'Enter Mmax : '
read(*,*) Mmax

delEim = Cp * ( Tm - T0 )
delEcm = delEim + nf

rho0 = 1.0d0 / V0
delv = ( V0 - VH ) * 1.0d-3
a = gamma / V0
b = 1.0d0 + a * delv * half
c = 1.0d0 / b
PH0 = Phoug(VH, V0, AA, BB)
EH0 = half * ( V0 - VH ) * PH0
Pi = PH0
Ei = EH0
TH0 = Thoug(PH0, rho0, AA, BB, gamma, Theta0, nk3, T0, Mmax)
Etotal = zero
EHI = zero
v = VH

write(1,40)'!', 'V', 'PH', 'Pi'
write(1,30)'!'
```

```
30    format(a1)
40    format(a1,7x,a4,13x,a2,13x,a6,13x,a2)
10    continue

      v = v + delv

      PH = Phoug(v, V0, AA, BB )

      if ( v .le. V0 ) then
      TH = Thoug(PH, rho0, AA, BB, gamma, Theta0, nk3, T0, Mmax)
c       else
c        PH = Phoug(V0, V0, AA, BB)
      endif

      EH = half * PH * ( V0 - v )
      Pf = ( PH + a * ( Ei - half * Pi * delv - EH ) ) * c
      delE = half * ( Pf + Pi ) * delv
      delP = Pi - Pf
       if ( delP .le. 1.0d-8 ) then
           delP = zero
       endif
      delUr = dsqrt(delP * delv)
      Ef = Ei - delE

      if ( v .le. V0 ) EHI = EHI + PH * delv

      Etotal = Etotal + delE
      Urtotal = Urtotal + delUr
      Pi = Pf
      Ei = Ef
```

```
c       write(1,50) (V0/v -1), PH, Pi
        write(1,50) v, PH, Pi

      If ( pf .ge. 1.0d-5 ) goto 10
c      if ( pf .le. zero ) then
c            pf = zero
c      endif
15     TR = TH0 * dexp ( - gamma / V0 * ( v - VH) )

      wheat = EH0 - Etotal

      if ( wheat .le. delEcm ) then
        if (wheat .lt. delEim ) then
          TR1 = TR
          TR2 = wheat /Cp + T0
        else
          TR1 = Tm
          TR2 = Tm
        endif
      else
        TR1 = TR - nf/Cp
        TR2 = (wheat - nf)/Cp + T0
      endif

      write(*,*)
      write(*,100) " Initial Hugoniot Pressure   (GPa)    :", PH0
      write(*,100) " Wasted Heat (EH0-Ei)        (MJ/Kg)  :",
     * EH0 - Etotal
        write(*,100) " Final specific volume      (cm3/g)  :", v
        write(*,*)
        write(*,100) " Ejecta velocity            (km/s)   :",
     * (2.0d0 * EH0) ** half + Urtotal
        write(*,100) " Twice Isothermal Sound Vel. (km/s)   :",
```

```
     *  2.0d0 * dsqrt(PH0 * V0)
        write(*,*)
        write(*,100) " Jap. Hougoniot temp.          (K) :", TH0
        write(*,100) " Jap. Residual temp.-no ch. phase (K) :", TR
        write(*,100) " Jap. Residual temp.-cg. phase    (K) :", TR1
        write(*,100) " Anderson Residual temp.       (K) :", TR2
        write(*,*)
        write(*,100) " Energy of shocked state EH0  (MJ/kg) :", EH0
        write(*,100) " Energy under isentrope  Ei   (MJ/kg) :", Etotal
        write(*,100) " Final Pressure              (GPa)   :", Pf
        write(*,*)
        write(*,100) " Shock Particle velocity     (km/s)  :",
     *  (2.0d0 * EH0) ** half
        write(*,100) " Residual velocity           (km/s)  :", Urtotal
        write(*,100) " Shock Wave Velocity         (km/s)  :",
c    *  V0 * dsqrt(PH0)/dsqrt(V0-VH)
     *  AA+BB*((2.0d0 * EH0) ** half)

        write(*,*)
50      format(4e15.5)
100     format(a,e11.4)
120     format(a,f12.3)
        close (1)
200     stop
        end

c**********************************************************************

      function Phoug(v, V0, coef1, coef2)
      double precision Phoug, v, V0, a1, denom, coef1, coef2, coef3

      coef3 = coef1 * coef1
      a1 =  V0 - coef2 * ( V0 - v )
```

```
      denom = a1 * a1
      Phoug = coef3 * ( V0 - v ) / denom

      return
      end
c ***********************************************************************
c ***********************************************************************
c **                                                                   **
c ** rho0   : initial density                                        **
c ** A      : bulk sound velocity                                     **
c ** B      : non-dim. coeff. in Us-Up relationship                   **
c ** g0     : Gr• $B]O• (Beisen parameter                             **
c ** Theta0 : Debye temperature for the initial state                 **
c ** T0     : initial temperature                                     **
c **                                                                   **
c ***********************************************************************

      function Thoug(PH, rho0, A, B, g0, Theta0, nk3, T0, Mmax)
      external CA, CX, XC

      double precision zero, half
      parameter ( zero = 0.0d0, half = 0.5d0 )

      double precision CA, CX, XC
      double precision C, A2, AB, AB2, gB, ABT, lC, lx, x, T
      double precision C00,C1,C2,C3,C4,C5,C6,C7,C8
      double precision M, PH, Thoug
      double precision rho0, A, B, g0, Theta0, nk3, T0, Mmax

      common /c_/C1,C2,C3,C4,C5,C6,C7,C8
```

```
      A2  = A*A
      AB  = A/B
      AB2 = AB * AB
      ABT = AB2 / ( Theta0 * nk3)
      gB  = g0 / B
      C1  = - gB
      C2  = gB * gB / 2.0d0
      C3  = C1 * C2 / 3.0d0
      C4  = C1 * C3 / 4.0d0
      C5  = C1 * C4 / 5.0d0
      C6  = C1 * C5 / 6.0d0
      C7  = C1 * C6 / 7.0d0
      C8  = C1 * C7 / 8.0d0

      M = 1.0d0
      T = T0
      x = Theta0 / T
      lx = dlog(x)
      lC = CX(lx)
      C00 = dexp(lC)

      M = half + sqrt(1.0d0/4.0d0 + B * PH / ( rho0 * A2 ) )
c      print*, M
      if ( M .le. 1.0d0 ) then
        print*, 'M < 1.0d0 : choose different Hougoniot pressure.'
       print*, 'The hougoniot pressure is, PH = ', PH
        stop
      endif

      C  = C00 + ABT * CA(M)
      lC = dlog(C)
      lx = XC(lC)
      x  = dexp(lx)
```

```
      Thoug  = Theta0 * dexp ( gB * (M - 1.0d0) / M ) / x

      if ( M .gt. Mmax ) then
         print*, 'M > Mmax'
         stop
      endif

      return
      end

c ========================
c ==  C - C00 = F(Mach) ==
c ========================

      function CA(Mach)

      double precision zero, half
      parameter (zero = 0.0d0, half = 0.5d0 )

      double precision M2, LM, Mach, Mach2, CA
      double precision C1,C2,C3,C4,C5,C6,C7,C8
      double precision Mn1, Mn2, Mn3, Mn4, Mn5, Mn6, Mn7, Mn8
      double precision fM0, fM1, fM2, fM3, fM4, fM5, fM6, fM7, fM8
      common /c_/C1,C2,C3,C4,C5,C6,C7,C8

      Mach2 = Mach * Mach
      M2 = half * Mach2
      LM = dlog(Mach)
      Mn1 = 1.0d0 / mach
      Mn2 = 1.0d0 / mach2
      Mn3 = Mn1 * Mn2
      Mn4 = Mn2 * Mn2
      Mn5 = Mn2 * Mn3
```

```
Mn6 = Mn3 * Mn3
Mn7 = Mn3 * Mn4
Mn8 = Mn4 * Mn4

fM0 = M2 - 2.0d0 * Mach + LM + 1.5d0
fM1 = M2 - 3.0d0 * Mach + 3.0d0 * LM + Mn1 + 1.5d0
fM2 = M2 - 4.0d0 * Mach + 6.0d0 * LM + 4.0d0 * Mn1 - half * Mn2

fM3 = M2 - 5.0d0 * Mach + 1.0d1 * LM + 1.0d1 * Mn1 - 2.5d0 * Mn2
fM3 = fM3 + Mn3 / 3.0d0 - 1.0d1 / 3.0d0

fM4 = M2 - 6.0d0 * Mach + 1.5d1 * LM + 2.0d1 * Mn1
fM4 = fM4 - half*1.5d1*Mn2 + 2.0d0 * Mn3 - Mn4 / 4.0d0
fM4 = fM4 - 3.5d1 / 4.0d0

fM5 = M2 - 7.0d0 * Mach + 2.1d1 * LM + 3.5d1 * Mn1
fM5 = fM5 - half * 3.5d1 * Mn2 + 7.0d0 * Mn3
fM5 = fM5 - 7.0d0 * Mn4 / 4.0d0 + Mn5 / 5.0d0 - half * 3.29d1

fM6 = M2 - 8.0d0 * Mach + 2.8d1 * LM + 5.6d1 * Mn1 - 3.5d1 * Mn2
fM6 = fM6 + 5.6d1 * Mn3 / 3.0d0 - 7.0d0 * Mn4 + 8.0d0*Mn5/5.0d0
fM6 = fM6 - Mn6 / 6.0d0 - 1.33d2 / 5.0d0

fM7 = M2  - 9.0d0*Mach + 3.6d1 * LM  + 8.4d1* Mn1 - 6.3d1 * Mn2
fM7 = fM7 + 4.2d1*Mn3  - 2.1d1 * Mn4 + 3.6d1* Mn5 / 5.0d0
fM7 = fM7 - half * 3.0d0 * Mn6 + Mn7/7.0d0 - 1.96d2/5.0d0
fM7 = fM7 - 1.0d0/7.0d0

fM8 = M2  - 1.0d1 * Mach + 4.5d1 * LM + 1.2d2 * Mn1
fM8 = fM8 - 1.05d2 * Mn2 + 8.4d1 * Mn3 - half * 1.05d2 * Mn4
fM8 = fM8 + 2.4d1 * Mn5 - half * 1.5d1 * Mn6
fM8 = fM8 + 1.0d1 * Mn7/7.0d0 - Mn8/8.0d0 -5.3d1 -1.01d2/5.6d1
```

```
      CA = fM0 + C1 * fM1 + C2 * fM2 + C3 * fM3 + C4 * fM4 + C5 * fM5
      CA = CA + C6 * fM6 + C7 * fM7 + C8 * fM8

      return
      end

c     ==========================================================
c     == Modified Debye Function : ln x = F( ln C) ==
c     ==========================================================

      function XC(CC)

      double precision XC, CC
      double precision CC0, CC1, CC2, CC3, CC4, CC5, CC6, CC7, CC8
      parameter ( CC0 = -0.29108336532d0,
     +          CC1 = -0.76850728989d0,
     +          CC2 = -0.72627595071d-1,
     +          CC3 =  0.68279735108d-2,
     +          CC4 =  0.18993280418d-2,
     +          CC5 = -0.4445271904d-3,
     +          CC6 = -0.60342849602d-4,
     +          CC7 =  0.28720614136d-4,
     +          CC8 = -0.26118858428d-5 )

      XC = CC7 + CC * CC8
      XC = CC6 + CC * XC
      XC = CC5 + CC * XC
      XC = CC4 + CC * XC
      XC = CC3 + CC * XC
      XC = CC2 + CC * XC
      XC = CC1 + CC * XC
      XC = CC0 + CC * XC
```

```
c   XC = CC5 + CC *(CC6 + CC *(CC7 + CC *CC8))
c   XC = CC0 + CC *(CC1 + CC *(CC2 + CC *(CC3 + CC *(CC4 + CC *XC))))

      return
      end

c ==========================================
c == Modified Debye Function : ln C = F( ln x) ==
c ==========================================

      function CX(XX)

      double precision CX, XX
      double precision CC0, CC1, CC2, CC3, CC4, CC5, CC6, CC7, CC8, CC9

      parameter ( CC0 = -0.39390925583d0,
     +            CC1 = -0.14112049057d1,
     +            CC2 = -0.22105029892d0,
     +            CC3 = -0.8187302888d-1,
     +            CC4 = -0.22886680929d-1,
     +            CC5 = -0.46986746487d-2,
     +            CC6 = -0.59581949858d-3,
     +            CC7 = -0.18701254466d-4,
     +            CC8 =  0.57170796191d-5,
     +            CC9 =  0.58720648417d-6 )

      CX = CC8 + XX * CC9
      CX = CC7 + XX * CX
      CX = CC6 + XX * CX
      CX = CC5 + XX * CX
      CX = CC4 + XX * CX
      CX = CC3 + XX * CX
```

```
      CX = CC2 + XX * CX
      CX = CC1 + XX * CX
      CX = CC0 + XX * CX

c     CX = CC5 + XX *(CC6 + XX *(CC7 + XX *(CC8 + XX *CC9)))
c     CX = CC0 + XX *(CC1 + XX *(CC2 + XX *(CC3 + XX *(CC4 + XX *CX ))))
      return
      end
```

APPENDIX C

```
{=================================      }
{     Code Name     :     gamma.p          }
{     Author        :     K. Nagayama      }
{                                          }
{     First Created :     April 29, 1994   }
{     Last Update   :     April 30, 1994   }
{     Latest Update :     April 30, 1994   }
{                                          }
{     Version No.   :     1.12             }
{                                          }

{-------------------------------------------------------------}
program gam(input,output);

const
        name = 'datafile';
var
        f: text;
        A, B, x, Us0, Up, Usp0, qs, qs0, dqs, dUp: real;
        g00, g000, g0, g1, g2, t, t23: real;
        { material: string[20]; }
        i, j, k, nt, N: integer;
{-------------------------------------------------------------}
    function Us (Up: real): real;
```

```
    begin
        Us := A + B * Up;
    end;
{-------------------------------------------------------------------}
    function g (Up, qs: real): real;
        var
            g001, g002, g003, g1, g2, Us1, Usp1, rUsUp: real;
    begin
        g001 := 2 * B - 2 / 3 - t / 3 + g00;
        g002 := B * (B - 2) - B * g001 - t / 3 * (1 - 4 * B + t23);
        g003 := B * (B * (B - 1) - (B + 1) / 2 * g001 - 3 / 2 *
g002) + 4 * sqr(B - t / 3) * (B - t / 3) + B * (B - t / 3) * g001;
        Us1 := Us(Up);
        Usp1 := Us1 - Up;
        rUsUp := Usp1 / Us1;
        g1 := g001 + g002 * Up / A + g003 * sqr(Up) / A / A;
        if Up > 0 then
            g2 := Usp1 / B / sqr(Up) * (A + 2 * B * Up - t23 *
A * Up / Usp1 - qs * exp(t23 * ln(Us1 / Usp1)) * A / sqr(Usp1))
        else
            g2 := g001;
        if rUsUp > 0.97 then
            g := g1
        else
            g := g2;
    end;
{-------------------------------------------------------------------}
    function dqsU (Up, qs: real): real;
        var
            z, Us1, Usp1: real;
    begin
        z := g(Up, qs);
        Us1 := Us(Up);
```

```
        Usp1 := Us1 - Up;
        dqsU := +qs * (z - (1 + t) / 3 - g00) * 2 * A / Us1 / Usp1;
    end;
{-------------------------------------------------------------------}
    procedure Runge_Kutta (var h, x0, y0, y: real);
        var
            hh, k0, k1, k2, k3, k4: real;
    begin
        hh := h / 2.0;
        k1 := h * dqsU(x0, y0);
        k2 := h * dqsU(x0 + hh, y0 + k1 / 2.0);
        k3 := h * dqsU(x0 + hh, y0 + k2 / 2.0);
        k4 := h * dqsU(x0 + h, y0 + k3);
        y := y0 + (k1 + 2 * k2 + 2 * k3 + k4) / 6.0;
    end;
{-------------------------MAIN PROGRAM-------------------------}
begin
    rewrite(f,name);
{       write(' Please input the name of the material : ');
    readln(material);
}   write('Please input the Hugoniot parameter A: ');
    readln(A);
    write('Please input the Hugoniot parameter B: ');
    readln(B);
    writeln('    v/v0      Up       qs       gamma ');
    writeln(f,'    v/v0      Up       qs       gamma ');

    N := 17500;
    nt := 100;
    dUp := 0.0005;
    t := 2.0;
    t23 := 2 / 3 * t;
    g00 := 0.0;
```

```
        Up := -dUp;
        qs := A * A;
        j := nt - 1;
        g0 := g000;

        for i := 1 to N do
            begin
                Up := Up + dUp;
                Us0 := Us(Up);
                Usp0 := Us0 - Up;
                j := j + 1;
                g0 := g(Up, qs);
                if (j = nt) then
                    begin
                        x := (Us0 - Up) / Us0;
                        writeln(x : 10 : 4, Up : 10 : 4, qs
: 10 : 3, g0 : 10 : 4);
                        writeln(f, x : 10 : 4, Up : 10 : 4,
qs : 10 : 3, g0 : 10 : 4);
                        j := 0;
                    end;
                qs0 := qs;
                Runge_Kutta(dUp, Up, qs0, qs);
            end;
        close(f);
end.
{-------------------------------------------------------------}
```

APPENDIX D

Proof and comments of various equations appeared in the main text

Proof of Eq. (2.3.1.3)

$$\sigma_1+\sigma_2+\sigma_3=-P+s_1-P+s_2-P+s_3=-3P+(s_1+s_2+s_3)=$$

$$=3\frac{1}{3}(\sigma_1+\sigma_2+\sigma_3)+(s_1+s_2+s_3)\Leftrightarrow(s_1+s_2+s_3)=0 \qquad \text{QED}$$

Proof of Eq. (2.3.1.6)

$$(s_1-s_2)^2+(s_2-s_3)^2+(s_3-s_1)^2=2Y^2\Leftrightarrow 2\left(s_1^2+s_2^2+s_3^2\right)-2(s_1s_2+s_2s_3+s_3s_1)=2Y^2 \quad (A4.1)$$

But from Eq. (2.3.1.3) we have the following set of equations:

$$\begin{aligned} s_1&=-(s_2+s_3)\\ s_2&=-(s_1+s_3)\\ s_3&=-(s_1+s_2)\end{aligned} \quad (A4.2)$$

From Eq. (A4.2) we get:

$$s_1s_2=(s_2+s_3)(s_1+s_3)\Leftrightarrow s_3^2+s_2s_3+s_3s_1=0 \quad (A4.3a)$$

Similarly for s_1s_3 and s_2s_3 we derive:

$$s_2^2 + s_2 s_1 + s_2 s_3 = 0 \tag{A4.3b}$$

$$s_1^2 + s_1 s_2 + s_3 s_1 = 0 \tag{A4.3c}$$

Adding Eqs. (A4.3a)-(A4.3c), we get:

$$2(s_2 s_3 + s_3 s_1 + s_1 s_2) = -(s_1^2 + s_2^2 + s_3^2) \tag{A4.4}$$

From Eqs. (A4.1) and (A4.4) we finally deduce:

$$s_1^2 + s_2^2 + s_3^2 = \frac{2Y^2}{3} \tag{A4.5}$$

Proof of Eq. (2.3.2.6)

From the 1st Hugoniot relation we have:

$$U_s = \frac{V_0 u_p}{V_0 - V} \tag{A4.6}$$

while from the 2nd Hugoniot relation may be written as:

$$P_H = \frac{U_s u_p}{V_0} \tag{A4.7}$$

The linear relation between the shock and particle velocity is:

$$s u_p = U_s - c_0 \tag{A4.8}$$

Substituting Eq. (A4.6) into Eq. (A4.8) and rearranging:

$$u_p = \frac{c_0 (V_0 - V)}{[V_0 - s(V_0 - V)]} \tag{A4.9}$$

Substituting Eq. (A4.9) into Eq. (A4.6):

$$U_s = \frac{c_0 V_0}{[V_0 - s(V_0 - V)]} \tag{A4.10}$$

Finally, from Eqs (A4.7), (A4.9) and (A4.10) we deduce:

$$P_H = \frac{{c_0}^2 (V_0 - V)}{[V_0 - s(V_0 - V)]^2} \tag{A4.11}$$

Proof of Eq. (2.3.2.9)

From the impedance match method, the impact velocity is the sum of the particle velocities of target and projectile materials:

$$U_0 = u_p^p + u_p^t \tag{A4.12}$$

But, the particle velocity, in general, is given by Eq. (AI.3.5a):

$$u_p = \sqrt{P_H(V_0 - V)} \tag{A4.13}$$

where the initial pressure P_0 is assumed to be zero.

Applying Eq. (A4.13) for both materials and substituting into Eq. (A4.12), we derive:

$$U_0 = \left[1 + \left(\frac{V_0^t - V_H^t}{V_0^p - V_H^p}\right)^{1/2}\right]\sqrt{P_H\left(V_0^p - V_H^p\right)} \tag{A4.14}$$

Proof of Eq. (2.3.2.23)

From the 3rd Hugoniot relation we have:

$$E_H = \frac{1}{2}P_H(V_0 - V) \tag{A4.15}$$

However, from the Mie-Gruneisen EOS the Hugoniot energy is the sum of the cold and thermal terms (neglecting electronic contributions):

$$E_H = E_C + E_T \tag{A4.16}$$

while the Hugoniot pressure is the sum of the cold and thermal pressures:

$$P_H = P_C + P_T \tag{A4.17}$$

From Eqs. (A4.15) and (A4.16) we have:

$$E_C + E_T = \frac{1}{2}P_H(V_0 - V) \tag{A4.18}$$

But the thermal energy is connected to the thermal pressure from:

$$E_T = \frac{VP_T}{\gamma(V)} \tag{A4.19}$$

Substituting Eq. (A4.17) into Eq. ((A4.19):

$$E_T = \frac{V(P_H - P_C)}{\gamma(V)} \tag{A4.20}$$

Finally, from Eqs (A4.18) and (A4.20):

$$P_H = \frac{(\kappa - 1)P_C - 2E_C/V}{\kappa - V_0/V} \qquad \text{(A4.21)}$$

where $\kappa = 2/\gamma + 1$.

The new method of calculating shock temperatures developed by K. Nagayama

Usually, shock temperature has been calculated by integrating Eq. (2.3.3.34), giving the value of C_V by Eq. (2.3.3.36). The new method, however, does not require any integration and has the following four stages:

1. Calculate the value of C at the initial state $C(S_0)$ (or $C_{M=1} = C(1)$) by the Debye function:

$$C(S) = C(x) = 3nk\frac{D_3(x)}{x}, \quad \text{where } x = \Theta_D / T \qquad \text{(A4.22)}$$

2. Calculate the increment in C from C(1), $\Delta C = C(M) - C(1)$ for the given shock strength by:

$$C(M) - C(1) = \frac{(C_0/s)^2}{\Theta_0}\int_1^M \frac{(M-1)^2}{M}\exp\left(-\frac{\gamma_0}{s}\frac{M-1}{M}\right)dM \qquad \text{(A4.23)}$$

where Θ_0 is the characteristic Debye temperature and M is the Mach number given by U_s/C_0.

3. Calculate the corresponding value of x to the value of C(M) by solving Eq. (A4.21).
4. Calculate the Debye temperature $\Theta(M)$ by solving:

$$\Theta(M) = \Theta_0 \exp\left(-\frac{\gamma_0}{s}\frac{M-1}{M}\right) \qquad \text{(A4.24)}$$

then use this value together with the value of x already calculated in step 3 to find the temperature.

The integral of Eq. (A4.23) has been approximated by a polynomial formula by expansion of the exponential term.

The function C(x) had been calculated (by K. Nagayama) by numerically integrating the Debye function over a wide range of x, that is $D_3(x)/x$ has been found for different values of x. These values gave a relationship which has been approximated by a polynomial. Sufficient precision was obtained only when the functional relationship has been represented in the plane of (lnC) vs. (lnx). It is required to calculate C from x in step 1 and x from C in step 3. For this purpose, it was necessary to have two approximate formulae. By introducing the variables $\zeta \equiv \ln C$

and $\xi \equiv \ln x$ and by writting the relationship between C(x) and x in polynomial forms he got coefficients by least square fit.

Why the release is nearly isentropic and the Riemannian integral

The difference between the principal Hugoniot and the isentrope centered at ambient conditions is small for small strains. This can be shown by expanding the entropy S in a Taylor series along the Hugoniot:

$$S = S_0 + \left.\frac{dS}{dV}\right|_0 (V - V_0) + \left.\frac{1}{2!}\frac{d^2S}{dV^2}\right|_0 (V - V_0)^2 + \left.\frac{1}{3!}\frac{d^3S}{dV^3}\right|_0 (V - V_0)^3 + \ldots + \left.\frac{1}{n!}\frac{d^nS}{dV^n}\right|_0 (V - V_0)^n + \ldots \tag{A4.25}$$

But from Eq. (2.3.3.35) we have:

$$\frac{dS}{dV} = \frac{1}{2T}\left[(V_0 - V)\frac{dP}{dV} + P - P_0\right] \tag{A4.26}$$

It can be proved that:

$$\left.\frac{dS}{dV}\right|_0 = \left.\frac{d^2S}{dV^2}\right|_0 = 0 \quad \text{and} \quad \left.\frac{d^3S}{dV^3}\right|_0 = -\frac{1}{2T_0}\frac{d^2P}{dV^2} \tag{A4.27}$$

Hence, from Eqs (A4.25) and (A4.27) we deduce:

$$S - S_0 = \left.\frac{1}{12T_0}\frac{d^2P}{dV^2}\right|_0 (V_0 - V)^3 + K(V_0 - V)^4 + \ldots \tag{A4.28}$$

Thus, to the 3rd order of strain, the entropy along the Hugoniot is constant and weak shock waves are nearly isentropic. However, an unsteady wave such as a spreading rarefaction can be approximated by an infinite number of vanishingly small discontinuities. Hence Eq. (A4.28) is applied to the release, and thus, release in nearly isentropic.

From Eq.(A4.13) we have:

$$u_p = \sqrt{P_H(V_0 - V)} \tag{A4.29}$$

The incremental change can be written as a differential:

$$du_p = \pm\sqrt{dP\,dV} \tag{A4.30}$$

where the sign depends on the direction of flow. However, Eq. (A4.30) may be applied to a release wave since it is approximated by an infinite number of vanishingly small discontinuities. In addition, it is nearly isentropic, hence $dP/dV = (\partial P/\partial V)_S$. This states the obvious fact that a principal Hugoniot has the slope of the isentrope only at the initial state. At other states along the

Hugoniot, the Hugoniot will always be steeper than the corresponding isentrope. (Mode I stability criterion by Segletes). Hence Eq. (A4.30) may take the form:

$$du_p = \pm\left(\frac{\partial P}{\partial V}\right)_S^{1/2} dV \quad \text{or} \quad u_p - u_{0p} = \int_{V_0}^{V}\left(\frac{\partial P}{\partial V}\right)_S^{1/2} dV \tag{A4.31}$$

Eq. (A4.31) is the Riemann integral and can be applied to usteady waves. It has also been used to predict the ejecta velocities in chapter 3.

The pressure dependence of a brittle material flow stress

It is well known that the yield stress of brittle materials depends on the hydrostatic pressure. The reason is that brittle materials cannot deform plastically by dislocation movement. Thus, they either have to continue on the elastic curve or fail by crack nucleation and growth (possible mechanism of failure waves).

Rosenberg (*J. Applied Phys.*, **76(3)**, 1543, 1994) expressed the above dependence mathematically:

From Eq. (2.3.1.1), the difference between the applied stress and mean hydrostatic pressure is the deviator stress which for 1-D strain equals 4/3 of the maximum shear strain:

$$s_1 = \sigma_1 - P = \tfrac{4}{3}\tau = \tfrac{2}{3}(\sigma_1 - \sigma_2) \tag{A4.32}$$

From the Griffith's criterion:

$$(\sigma_1 - \sigma_2)^2 = Y_0(\sigma_1 + \sigma_2) \tag{A4.33}$$

Using Eqs. (A4.32) and (A4.33):

$$s_1 = \left(\sigma_1 - \frac{1}{3}(\sigma_1 + 2\sigma_2)\right) = \frac{2}{3}(\sigma_1 - \sigma_2) = \frac{2}{3}\sqrt{Y_0(\sigma_1 + \sigma_2)} = \frac{2}{3}\sqrt{Y_0(3P - \sigma_2)} = \frac{2}{3}\sqrt{Y_0(2P + P - \sigma_2)} \tag{A4.34}$$

But

$\sigma_2 - P = s_2$ and $s_3 = \sigma_3 - P = \sigma_2 - P$

and

$$s_1 + s_2 + s_3 = s_1 + \sigma_2 - P + \sigma_3 - P = s_1 + 2(\sigma_2 - P) = 0 \Leftrightarrow P - \sigma_2 = \frac{s_1}{2} \tag{A4.35}$$

From Eqs. (A4.34) and (A4.35) we get:

$$s_1^2 = \frac{4}{9}\left[Y_0\left(2P + \frac{s_1}{2}\right)\right] \tag{A4.36}$$

Solving for s_1 and putting $s_1^* = s_1/Y_0$ and $P^* = P/Y_0$, we can solve Eq. (A4.36) for s_1^*:

$$s_1^* = \frac{1}{9}\left(1+\sqrt{1+72P^*}\right) \approx \frac{1}{9}\left(1+6\sqrt{2P^*}\right) \qquad \text{(A4.37)}$$

Substituting Eq. (A4.37) into Eq. (A4.32) we finally derive an expression for the normalised shear strength:

$$\tau^* = \frac{1}{12}\left(1+6\sqrt{2P^*}\right) \qquad \text{(A4.38)}$$

Thus, the shear strength of a brittle solid should increase with shock pressure. This Eq. Should apply behind the shock wave and before the failure wave arrives. This is indeed what we observe on glasses and ceramics where the shear strength increases with impact stress (unfailed region) and then drops to a constant value as the failure wave appears.